

12-2023

## ONCOGENIC KRAS AND TELOMERE BIOLOGY IN CRC PROGRESSION

Ronald DePinho

Follow this and additional works at: [https://digitalcommons.library.tmc.edu/utgsbs\\_dissertations](https://digitalcommons.library.tmc.edu/utgsbs_dissertations)



Part of the [Cancer Biology Commons](#)

---

### Recommended Citation

DePinho, Ronald, "ONCOGENIC KRAS AND TELOMERE BIOLOGY IN CRC PROGRESSION" (2023).  
*Dissertations and Theses (Open Access)*. 1310.  
[https://digitalcommons.library.tmc.edu/utgsbs\\_dissertations/1310](https://digitalcommons.library.tmc.edu/utgsbs_dissertations/1310)

This Dissertation (PhD) is brought to you for free and open access by the MD Anderson UTHealth Houston Graduate School at DigitalCommons@TMC. It has been accepted for inclusion in Dissertations and Theses (Open Access) by an authorized administrator of DigitalCommons@TMC. For more information, please contact [digcommons@library.tmc.edu](mailto:digcommons@library.tmc.edu).

**ONCOGENIC KRAS AND TELOMERE BIOLOGY IN CRC PROGRESSION**

by

**Wen-Hao (Howard) Hsu, M.S.**

**APPROVED:**

\_\_\_\_\_  
Ronald DePinho, M.D.

\_\_\_\_\_  
Scott Kopetz, M.D., Ph.D.

\_\_\_\_\_  
Guillermina Lozano, Ph.D.

\_\_\_\_\_  
Traver Hart, Ph.D.

\_\_\_\_\_  
Jian Hu, Ph.D.

**APPROVED:**

\_\_\_\_\_  
Dean, The University of Texas

MD Anderson Cancer Center UTHealth Houston Graduate School of Biomedical Science

**ONCOGENIC KRAS AND TELOMERE BIOLOGY IN CRC PROGRESSION**

A

**DISSERTATION**

Presented to the Faculty of

The University of Texas

MD Anderson Cancer Center UTHealth Houston

Graduate School of Biomedical Sciences

in Partial Fulfillment

of the Requirements

for the Degree of

**Doctor of Philosophy**

by

**Wen-Hao (Howard) Hsu, M.S.**

Houston, Texas

December 2023

## ACKNOWLEDGEMENTS

First and foremost, I would like to extend my heartfelt gratitude to my Ph.D. mentor, Dr. Ronald DePinho. Completing this journey would not have been possible without Dr. DePinho's unwavering support and mentorship. He exemplified the essence of a true mentor, and I deeply appreciate his remarkable patience in guiding me through my academic pursuits. I am profoundly grateful for the opportunity to have been mentored by him during my graduate studies and for the privilege of being a part of his research laboratory.

I also wish to convey my sincere appreciation to my advisory committee members, Dr. Scott Kopetz, Dr. Guillermina Lozano, Dr. Filippo Giancotti, Dr. Traver Hart, and Dr. Jian Hu. Their invaluable guidance, constructive feedback, and continuous encouragement have significantly contributed to the success of my research projects over the years. Their unwavering support has enriched my understanding of cancer biology and improved the quality of my work.

I extend my heartfelt thanks to the current and former members of the DePinho laboratory. Collaborating with such a talented and dedicated group of individuals has been a highlight of my Ph.D. training. Their collective wisdom, camaraderie, and shared passion for scientific exploration have enriched my academic experience in immeasurable ways. I also want to express my sincere gratitude to my dear friends who have brought immense joy and companionship to my life during my time in Houston. Your unwavering support and shared experiences have been a source of strength and happiness. Furthermore, I cannot adequately express my appreciation to my friends in Taiwan, who have consistently demonstrated their care and support, even from afar. Your friendship has been a constant source of encouragement and connection.

Last but certainly not least, my deepest and most heartfelt thanks go to my family. Throughout the challenging journey of pursuing a Ph.D., their unwavering support, encouragement, and unconditional love have been my anchor. It is their unwavering belief in me that has empowered me to pursue my academic and career aspirations, enabling me to reach for and achieve my dreams.

## ONCOGENIC KRAS AND TELOMERE BIOLOGY IN CRC PROGRESSION

Wen-Hao (Howard) Hsu, M.S.

Advisory Professor: Ronald DePinho, M.D.

While colorectal cancer (CRC) patients diagnosed with localized stage disease (as defined by SEER) have a 5-year survival rate of 90%, this rate plunges to 14% for patients diagnosed with metastatic CRC. Consequently, there is an immediate imperative to elucidate the mechanisms that drive the transition to advanced CRC.

Human CRCs carrying oncogenic mutations in the *KRAS* oncogene, henceforth referred to as *KRAS\**, exhibit a 25% higher propensity for developing liver metastases. Similarly, in our CRC mouse model, engineered with an inducible *Kras\** transgene and conditional null alleles of *Apc* and *Tp53* (referred to as iKAP), *KRAS\** has been implicated in driving cancer progression and metastasis. Mechanistically, *KRAS\**-driven cancer metastasis operates, in part, by activating cancer cell-intrinsic TGF $\beta$  signaling and suppressing anti-tumoral immunity through the IRF2-CXCL3 axis, which recruits myeloid-derived suppressor cells. Regrettably, emerging therapies targeting *KRAS\** have demonstrated limited efficacy in clinical settings. This challenge has spurred our efforts to identify and validate additional mechanisms underpinning *KRAS\**-driven cancer progression, with the ultimate aim of expanding the array of therapeutic targets for metastatic CRC. By utilizing the iKAP model and employing functional gene set enrichment and histological analyses of *KRAS\**-expressing CRC metastases, we have uncovered a robust adipogenesis signature and an abundance of lipid-rich fibroblasts and angiogenesis in the tumor microenvironment. Consequently, our co-culture experiments involving mouse embryonic fibroblasts and conditioned media from iKAP primary cell lines

have induced their differentiation into a cell population displaying traits of both adipocytes and fibroblasts, aptly referred to as 'lipid-rich fibroblasts.' In the initial segment of my study, I have elucidated the molecular mechanisms through which KRAS\*-expressing cancer cells drive lipo-fibrogenesis and have shed light on the tumor biological role of lipid-rich fibroblasts in facilitating KRAS\*-driven CRC progression.

As only a minority of cases among both human and mouse KRAS\* CRC show progression to metastatic disease, it is clear that genetic events beyond *KRAS* activation play a pivotal role in driving metastases. Notably, patients, irrespective of *KRAS* mutations, exhibit a nearly identical lymph node metastatic rate of approximately 40%. In order to explore these pro-metastasis events more effectively, I propose an integration of an inducible telomerase reverse transcriptase (*LSL-Tert*) into our existing iAP model, which is engineered with conditional null alleles of *Apc* and *Tp53*. This introduced modification enables us to replicate telomere-based crisis and genome instability, subsequently followed by telomerase reactivation. In prior studies employing telomerase-inducible mouse models of prostate cancer, the introduction of crisis-telomerase sequences led to the development of cancer-relevant genomic aberrations and an escalation in metastatic potential. While the inclusion of genomic instability within the iAP model may not fully replicate the intricacies of the human context, it does provide a platform for identifying gene alterations and biological transformations associated with the metastatic process. In the second phase of my research, I have introduced human-like telomere dynamics into the iAP model (referred to as iTAP) to investigate the consequences of telomere-based crisis and telomerase reactivation in driving metastasis and unraveling the underlying biological changes. These endeavors hold the potential to expedite the discovery of novel therapeutic targets for advanced CRC disease.

## TABLE OF CONTENTS

APPROVAL.....	i
TITLE.....	ii
ACKNOWLEDGEMENTS.....	iii
ABSTRACT.....	v
TABLE OF CONTENTS.....	vii
LIST OF FIGURES.....	viii
CHAPTER 1: INTRODUCTION.....	1
CHAPTER 2: MATERIALS AND METHODS.....	8
CHAPTER 3: KRAS* REGULATES CRC STROMA IN THE ENRICHMENT OF LIPID-RICH CAFS .....	25
CHAPTER 4: KRAS* UPREGULATES PROADIPOGENIC CYTOKINES TO ORCHESTRATE LIPO-FIBROGENESIS AND PROMOTE TUMOR GROWTH.....	41
CHAPTER 5: KRAS* REGULATES PRO-ADIPOGENESIS CYTOKINES THROUGH TFCP2.....	55
CHAPTER 6: LIPID-RICH CAFs SECRETE VEGFA TO PROMOTE TUMOR ANGIOGENESIS.....	65
CHAPTER 7: THE IMPACT OF TELOMERE DYNAMICS BEYOND KRAS* ON CRC.....	78
CHAPTER 8: TELOMERE DYNAMICS-DRIVEN CHROMOSOMAL INSTABILITY MODULATES TUMOR IMMUNITY.....	89
CHAPTER 9: CONCLUSIONS AND DISCUSSION.....	100
BIBLIOGRAPHY.....	108
TABLES.....	123
VITA.....	128



## LIST OF FIGURES

FIG. 1A GSEA transcriptomic profiling.....	27
FIG. 1B-C Immunohistochemical staining of lipid droplets.....	28
FIG. 1D-E The quantification of LipidTOX+ cells.....	29
FIG. 1F The quantification of LipidTOX+ cells in different tumor stages.....	30
FIG. 1G Single-cell sequencing in GEM to identified lipid-rich CAFs.....	32
FIG. 1H Single-cell sequencing in human CRC to identified lipid-rich CAFs.....	33
FIG. 1I-J Adipokine gene module score plots in GEM CRC stroma.....	34
FIG. 1K-L Adipocyte and lipofibroblast genes' expression level in CRC stroma.....	36
FIG. 1M Adipocyte and myofibroblast gene module score plot in human CRC stroma.....	37
FIG. 1N CAF marker gene expression levels in lipid-rich and -sparse cells.....	38
FIG. 1O-P Proportion of $\alpha$ SMA+ and lipid-rich CAF subgroups.....	39
FIG. 1Q The lipid-rich CAFs GSVA score analysis in TCGA-COAD.....	39
FIG. 2A Putative secretome that is regulated by KRAS*.....	43
FIG. 2B Pathway analyses in KRAS* stroma.....	43
FIG. 2C-G BMP4 and WNT5B is regulated by KRAS*.....	45
FIG. 2H-M KRAS* tumor CM drives fibroblast to obtain adipocyte traits.....	47
FIG. 2N-O Orthotopic co-injection experimental design.....	50
FIG. 2P-U Lipid-rich CAFs drive tumor progression and worse survival.....	52
FIG. 3A Putative transcription factors that is regulated by KRAS*.....	57
FIG. 3B-D TFCEP2 regulates BMP4 and WNT5B.....	58
FIG. 3E TFCEP2 positive correlates with adipocyte in TCG-COAD.....	59
FIG. 3F-G TFCEP2 regulates the present of lipid-rich fibroblasts.....	60
FIG. 3H TFCEP2 regulates tumor progression.....	60
FIG. 3I-J TFCEP2 does not regulates cell proliferation.....	61

FIG. 3K-L TFCEP2 positive correlates with worse survival.....	63
FIG. 3M-P FQI1 decrease lipid-rich CAFs and extend survival.....	63
FIG. 4A-C Angiogenesis positive correlates with lipid-rich CAFs.....	67
FIG. 4D-G Lipid-rich CAFs secrete VEGFA.....	69
FIG. 4H-K KRAS* positive correlates with VEGFA and endothelial cells.....	71
FIG. 4L-N KRAS*-TFCEP2-VEGFA axis regulates tumor progression.....	75
FIG. 4O-P Preclinical study of FQI1 and VEGFA Ab.....	76
FIG. 5A-D Telomere dynamics models.....	80
FIG. 5E Schematic diagram of the dynamics of telomeres.....	82
FIG. 5F Kaplan–Meier survival curves of iTAP mice.....	82
FIG. 5G-H Single-cell sequencing analyses in iTAP.....	84
FIG. 5I-K Inferred CNA analyses in iTAP.....	86
FIG. 5L Inferred CNA analyses in human CRC.....	88
FIG. 6A Pathway analyses in CIN high models.....	92
FIG. 6B-D Immune population analyses in iTAP scRNAseq .....	94
FIG. 6E-F Gamma-delta T 17 in iTAP G4 tumor .....	97
FIG. 6G-I IL1B expression level in iTAP G4 epithelial tumor .....	99
FIG. 7A Schematic diagram of the proposed mechanism that regulates the progression of CRC through the KRAS*-TFCEP2-VEGFA axis .....	102

**CHAPTER 1:**  
**INTRODUCTION**

## CHAPTER 1: INTRODUCTION

### 1.1 Gene Alterations In CRC

CRC accounts for more than 50,000 deaths in the United States and 600,000 deaths globally annually (Li et al., 2021; Siegel et al., 2022). While the 5-year survival rate stands at 90% for localized CRC, it drops drastically to a mere 14% for advanced metastatic disease (Manfredi et al., 2006). The signature genetic alterations seen in CRC encompass activating oncogenic mutations in *KRAS* (42%) and inactivating mutations and/or deletions of the *APC* (75%) and *TP53* (60%) tumor suppressor genes (Wood et al., 2007, TCGA-COAD). In human CRC, the most prevalent activating *KRAS* mutation, *KRAS*<sup>G12D</sup>, exhibits a positive correlation with advanced disease (Li et al., 2011) and is highly co-occurring in primary and metastatic tumors, underscoring its role in CRC progression (Knijn et al., 2011). Similarly, studies involving mice engineered with a doxycycline (DOX)-inducible *Kras*<sup>G12D</sup> allele and conditional null alleles for *Apc* and *Tp53*, designated as "iKAP" mice, have provided compelling evidence that *KRAS*<sup>G12D</sup> (hereafter referred to as *KRAS*<sup>\*</sup>) suppresses anti-tumor immunity and promotes increased invasiveness and metastatic potential (Boutin et al., 2017, Liao et al., 2019).

### 1.2 *KRAS*<sup>\*</sup> Plays an Important Role to Drive Cancer Metastases

The most prevalent mutation in the *KRAS* gene occurs at codon 12, leading to the substitution of glycine (G) with aspartic acid (D); this specific mutation, has been consistently associated with advanced invasive stages and liver metastasis in CRC (Li et al., 2011). Furthermore, there is a remarkable 96% co-occurrence of *KRAS*<sup>\*</sup> between primary CRC tumors and their metastases, underscoring the pivotal role of *KRAS*<sup>\*</sup> in the progression of CRC (Knijn et al.,

2011). In the TCGA CRC dataset, 25% of *KRAS* mutant patients are diagnosed with late-stage and distal metastases. The DFCI colorectal adenocarcinoma dataset, the second largest CRC dataset globally, mirrors these findings, with 36.4% of mutant *KRAS* cancer patients diagnosed with late-stage and distal metastatic cancer. Importantly, our iKAP engineered mouse (GEM) model accurately recapitulates this human metastatic CRC disease. In this model, CRC with *Kras*\* exhibits a 25% metastatic rate, while iAP mice lacking *Kras*\* show no metastases (Boutin et al., 2017), providing further evidence of the critical role played by *Kras*\* in driving cancer metastasis.

### **1.3 The Limitation of Targeting the KRAS Signaling Pathways in CRC Progression**

Targeting the KRAS signaling pathway, specifically the RAF-MEK-ERK cascade, has yielded limited success in clinical applications for several compelling reasons: 1) Oncogenic *KRAS* activates numerous downstream pathways (Pylayeva-Gupta et al., 2011); 2) *KRAS* mutation plays a partial yet crucial role in CRC maintenance and progression (Kapoor et al., 2014); 3) CRC has the capacity to activate alternative *KRAS*-dependent survival signaling mechanisms (Chen et al., 2021); 4) Intra-tumoral genomic heterogeneity in *KRAS* mutations exists (Fearon et al., 2015); 5) Distinct microenvironmental changes occur in *KRAS*-mutation-driven CRC, limiting the efficacy of targeting *KRAS* signaling with therapeutic interventions. Furthermore, a study involving CRC cell lines has demonstrated that many *KRAS* mutant lines are not entirely reliant on sustained *KRAS* expression but depend on TAK1 kinase instead (Singh et al., 2012). The precise regulation of cell intrinsic pathways by oncogenic *KRAS* in the context of CRC maintenance and progression remains inadequately understood. To address these complexities, our iKAP CRC model, engineered with key mutations, offers a valuable platform for replicating genomic heterogeneity and evolutionary dynamics. It allows us to investigate the role of *KRAS* mutations in tumor progression and therapeutic responses. Previous

research has shown that activated KRAS\* contributes to invasion, partly through the activation of TGF- $\beta$ , and induces a transcriptional profile enriched with features reminiscent of an invasive human CRC signature. In clinical studies, TGF- $\beta$  inhibitors have been deemed safe in humans but have shown limited clinical efficacy (Morris et al., 2014; Rodon et al., 2015). A significant challenge in utilizing TGF- $\beta$  inhibitors lies in identifying responders among CRC patients. In some cases, inhibiting TGF- $\beta$  in systemic or epithelial CRC, as observed in *Apc* mutation mice, has been associated with promoting cancer progression, inflammation, and reduced survival rates (Principe et al., 2017). Therefore, the discovery of novel functional pathways regulated by KRAS holds the promise of identifying potential therapeutic targets that could ultimately enhance the survival rates of CRC patients.

### **1.3 Current Targeted Therapies in CRC**

Current targeted therapies focused on growth factor receptors, including epidermal growth factor receptor (EGFR), fibroblast growth factor receptor, and insulin-like growth factor 1 receptor, have exhibited limited clinical efficacy in metastatic CRCs harboring KRAS\*. This aligns with the role of KRAS\* in regulating cell survival and proliferative signaling downstream of these growth factor receptors. Alternative approaches to address KRAS\*-driven CRC have involved targeting the downstream pathways of KRAS\*, such as the phosphoinositide 3-kinase (PI3K)/ mammalian target of rapamycin (mTOR) and KRAS\*/MEK pathways. However, attempts to inhibit mTOR (Spindler et al., 2013) or MEK (Infante et al., 2012) have not yielded significant clinical benefits in KRAS\*-driven CRC patients, indicating the potential presence of alternative or redundant KRAS\* signaling pathways. This redundancy hypothesis is supported by evidence from combined treatments involving MEK inhibitors (binimetinib), BRAF inhibitors (encorafenib), and EGFR inhibitors (cetuximab), which have shown enhanced clinical benefits in CRC patients with the BRAF<sup>V600E</sup> mutation. Nonetheless, recurrence remains a common

occurrence in most cases, and treatment merely extends median survival by 3.6 months (Kopetz et al., 2019). The intricate role of KRAS\* in CRC biology is further underscored by its ability to suppress anti-tumoral immunity through the recruitment of myeloid-derived suppressor cells (Liao et al., 2019). While new therapies directly targeting KRAS\* (e.g., adagrasib and sotorasib) have demonstrated promising anti-tumor activity, tumors in patients treated with these therapies swiftly develop resistance mechanisms (Awad et al., 2021). This emphasizes the imperative need to gain a deeper understanding of the KRAS\* signaling network to identify alternative or synergistic therapeutic approaches for patients with KRAS\*-driven CRC.

#### **1.4 The Complex Role of KRAS\* in Shaping Tumor Microenvironment of CRC**

The ongoing challenge of identifying alternative or synergistic therapeutic strategies for KRAS\*-driven CRC has spurred a deeper examination of KRAS\*'s role in CRC tumor biology, particularly its impact on various host cells within the tumor microenvironment. These host cells encompass immune cells, endothelial cells, and cancer-associated fibroblasts (CAFs), with a specific focus on the intriguing and relatively poorly understood CAFs. CAFs, although abundant in the tumor microenvironment, remain among the least characterized cell types. CAFs can be classified into subtypes based on specific markers, including alpha smooth muscle actin ( $\alpha$ SMA), fibroblast-activation protein, and platelet-derived growth factor receptor (PDGFR). The two most consistently defined CAF subtypes across diverse cancers are myofibroblastic CAFs ( $\alpha$ SMA+) and non-myofibroblastic CAFs ( $\alpha$ SMA-) (Bartoschek et al., 2018; Bernard et al., 2019; Costa et al., 2018; Li et al., 2017). Myofibroblasts are characterized as lipid-sparse cells that undergo transdifferentiating from adipocytes or lipofibroblasts (El Agha et al., 2017; Shook et al., 2020). CAFs play divergent roles in either promoting or suppressing cancer progression (Biffi et al., 2021; Kalluri, R. 2016). Specifically,  $\alpha$ SMA+

fibroblasts have been shown to suppress Lgr5+ cancer stem cells, thereby restraining CRC progression (McAndrews et al., 2021). Conversely,  $\alpha$ SMA- CAFs have been found to secrete lipid metabolites into the tumor microenvironment through fatty acid translocase, thereby enhancing CRC metastasis by modulating membrane fluidity (Gong et al., 2020; Peng et al., 2022). Emerging evidence suggests that specific cancer genotypes can exert influence over CAF biology (Pereira et al., 2019). For example, the loss of *TP53* can activate JAK2-STAT3 signaling, leading to stromal fibrogenesis and enhanced tumor growth (Wormann et al., 2016). In the context of KRAS\*-induced cancer, sonic hedgehog (SHH) secretion by cancer cells shapes stromal cells, initiating reciprocal signaling via AXL/IGF1R-AKT signaling in pancreatic cancer (Tape et al., 2016). Additionally, KRAS\* has been found to reprogram pancreatic fibroblasts, activating inflammatory genes and polarizing pro-tumorigenic macrophages (Velez-Delgado et al., 2022). Moreover, in cases of *BRCA*-mutated cancer cells, heat shock factor 1 (HSF1) activation in pancreatic stellate cells (PSCs) prompts their transformation into CLU+ immune regulatory CAFs (Shaashua et al., 2022). While it is evident that KRAS\* and other oncogenic events in cancer cells can influence various aspects of CAF biology, the precise mechanisms through which these events impact CAF subtype biology and heterogeneity represent a current focus of active research.

### **1.5 The Role of Telomerase Reactivation and Chromosomal Instability, Beyond Kras\* Activation, in Colorectal Cancer Progression and Metastasis**

Stem cells play a crucial role in maintaining tissue integrity through their remarkable capacity for self-renewal and differentiation into various cell types. However, as individuals age, this long-term self-renewal ability becomes susceptible to the accumulation of DNA mutations, potentially leading to the initiation of cancer (Reya et al., 2001). This vulnerability is compounded by the process of aging, which includes telomere shortening, ultimately



culminating in what is known as telomere crisis. Telomere crisis, in turn, triggers chromosomal alterations, significantly increasing the likelihood of DNA mutations (Artandi et al., 2000). It is worth noting, however, that only an exceedingly rare 1 out of 10 million events occurring during telomere crisis progresses to cancer. Moreover, most human cancers exhibit elevated levels of telomerase activity (Harley et al., 2008). Based on these insights into telomere dynamics in cancer development, we formulated a hypothesis that reactivating telomerase, an enzyme critical for genome stability and cellular fitness, could potentially enhance tumor malignancy and promote cancer metastases. In 2012, our group provided compelling evidence for this concept by demonstrating that telomerase reactivation following telomere dysfunction led to the development of metastases in our *LSL-Tert* mouse model, featuring conditional knockout of the *PB-Pten/ Tp53* genes in prostate cancer (Ding et al., 2012). In the context of colorectal cancer (CRC) progression, approximately 70% of cases exhibit chromosomal instability (CIN), characterized by one of several genomic instability pathways (Lengauer et al., 1998). The amplification of CIN, in conjunction with mutations in tumor suppressor genes or the activation of oncogenes, assumes a pivotal role in advancing CRC (Pino et al., 2010). However, it is important to note that only a minority of cases, both in humans and our mouse model of *KRAS\** CRC, progress to metastatic disease. Remarkably, patients, regardless of *KRAS* mutations, exhibit nearly identical lymph node metastatic rates of approximately 40%. Therefore, the innovative *LSL-TERT* DOX-inducible telomerase reactivation process employed within our iAP model offers an ideal platform for conducting comprehensive investigations into the role of telomere dynamics, alongside oncogenic *KRAS*, in driving CRC metastasis.

**CHAPTER 2:**  
**MATERIALS AND METHODS**

## CHAPTER 2: MATERIALS AND METHODS

Content of this chapter is partly based on the following manuscript:

Hsu, W.H., LaBella, K. A., Lin, Y., Xu, P., Lee R., Hsieh, C.E., Yang, L., Zhou, A., Blecher, J. M., Wu, C. J., Lin, K., Shang, X., Jiang, S., Spring, D. J., Xia, Y., Chen, P., Shen, J. P., Kopetz, S., DePinho, R. A. (2023) "Oncogenic KRAS drives lipo-fibrogenesis to promote angiogenesis and colon cancer progression" *Cancer Discov*, 10.1158/2159-8290.CD-22-1467

### Cell culture

The iKAP primary cell line cultures were derived from GFP+ iKAP-dissociated tumors and were subsequently cultured in Dulbecco Modified Eagle's Medium (Gibco; 11995-065) with or without DOX supplementation (2 µg/mL). The following cell lines were used in our study. CMT93 (ATCC; CCL-223): Cultured in DMEM with supplementation as per ATCC's guidelines; 293T (ATCC; CRL-3216): Cultured in DMEM with supplementation as per ATCC's guidelines; 3T3L1 (ATCC; CL-173): Cultured in DMEM with supplementation as per ATCC's guidelines; DLD1 isogenic KRAS wild-type CRC cells: Cultured in RPMI-1640 medium (Gibco; 11875-093); hMSC (ATCC; SCRC-4000): Obtained from ATCC and cultured in Mesenchymal Stem Cell Basal Medium (ATCC PCS-500-030) with supplementation as specified by ATCC; HUVEC (CRL-1730): Obtained from ATCC and cultured in F-12K Medium (ATCC; 30-2004) with supplementation according to ATCC's recommendations. All cell lines were cultured in the specified medium containing 10% fetal bovine serum or bovine calf serum (Sigma), and 1% Antibiotic-Antimycotic (Gibco; 15-240-062) following ATCC's instructions. Furthermore, regular mycoplasma testing using the Mycoplasma Elimination Kit (Sigma; MP0030) was performed to confirm that the cells

remained mycoplasma-free. The cells were maintained at a temperature of 37°C with a 5% CO<sub>2</sub> atmosphere.

To induce adipogenic cell differentiation, supplemental recombinant Bmp4 and Wnt5b proteins were utilized. Specifically, 100 ng/mL Bmp4 (R&D; 5020-BP-010) and 100 ng/mL Wnt5b (R&D; 3006-WN-025) were introduced into the complete 3T3L1 medium. Following this, the medium was supplemented with 10 µg/mL insulin for a duration of 2 days. The transcriptional expression of adipogenic genes was subsequently validated using RT-qPCR after a 2-week period.

Conditioned media (CM) were obtained from iKAP cell lines, DLD1 cell lines, and PDXOs after 24 hours of culturing in specific complete culture media for each experiment. Following a published protocol (Scott et al., 2011), in vitro differentiation was accomplished by co-culturing 3T3L1 cells or hMSCs with the CM from iKAP or DLD1 cell lines for a period of 16 days. During this period, old CM was replaced with fresh CM every 2 days. In the final 2 days, adipogenic terminal differentiation was initiated by adding insulin to a concentration of 10 µg/mL (Sigma; 11070-73-8 and Sigma; 11061-68-0), 3-isobutyl-1-methylxanthine to 500 µM (Sigma; I7018), and dexamethasone to 700 nM (Sigma; D4902). Validation of adipogenic differentiation was conducted through immunoblotting, RT-qPCR, IHC, and immunofluorescence procedures to confirm the presence of genes associated with adipocytes and lipid-rich fibroblasts.

### **Patient derived xenograft organoids establishment and maintenance**

In human studies, ethical guidelines outlined in the Helsinki Declaration were followed, and the research was conducted in accordance with an Institutional Review Board-approved

protocol at MD Anderson Cancer Center. All patients participating in the study provided written informed consent for tissue distribution and specimen collection. To generate organoids, primary human tumor xenografts were first minced and then digested in a digestion buffer consisting of DMEM (Gibco; 11995-065), 100 U/ml Penicillin/Streptomycin (Gibco; 15140-122), 500 U/ml Collagenase IV (Thermo; 17104019), and 125 mg/ml Dispase type II (Thermo; 17105041). This digestion process took place for 30 minutes at 37 °C. Subsequently, the samples were washed sequentially with DMEM/5% FBS and PBS. The digested tumor cells were resuspended in Matrigel and plated onto a 24-well culture plate, with each well receiving approximately 10% confluent cells in a 30 mL droplet. Once the gel solidified, 500 µl of WENR medium was added to each well. The WENR medium was composed of Advanced DMEM/F12 medium (Gibco; 12634-010), 1 mM GlutaMAX (Gibco; 35050-061), 1 mM HEPES (Gibco; 15630-080), and 100 U/ml Penicillin/Streptomycin (Gibco; 15140-122). This medium was supplemented with various components, including 50% Wnt-3A conditioned medium from L-Wnt3A cells (ATCC; CRL-2647), 10% R-spondin-1 conditioned medium from R-spondin1 cells (Sigma; SCC111), 100 ng/ml hNoggin (R&D; 6507-NG), 10 nM hGastrin I (Sigma; G-9145), 500 nM A83-01 (Tocris; 2939), 10 µM SB202190 (Sigma; S7067), 10 mM Nicotinamide (Sigma; N0636), 1X B27 supplement (Gibco; 008-0085SA), 1X N2 supplement (Gibco; 17502-048), 1 mM N-acetyl cysteine (Sigma; A9165), and 50 ng/ml hEGF (R&D; 236-EG). These cultures were then incubated at 37 °C.

Established organoids were subjected to routine passage every 10 to 14 days, maintaining a cell density of approximately 50% confluence. To release organoids from the Matrigel, they were incubated with Cell Recovery Solution (Corning; 354253) at 4 °C for 30-40 minutes. Subsequently, the released organoids were either mechanically pipetted to break them down into smaller fragments or further dissociated using TrypLE Express Solution

(Gibco; 12604013) at 37 °C for 3-5 minutes to obtain smaller fragments or individual cells. After a thorough wash with PBS, the resulting fragments and cells were resuspended in Matrigel (Corning; 356231) and plated onto 24-well culture plates (Thermo; 142475), typically at a split ratio of 1:3–1:4. The culture medium was refreshed every 2 to 3 days. To ensure quality control, regular checks for mycoplasma contamination were conducted using STR sequencing. For long-term storage, organoid fragments or dissociated single cells were resuspended in cold Recovery Cell Culture Freezing Medium (Gibco; 12648010), gradually frozen to –80°C, and then stored in liquid nitrogen.

### **Tumor models and treatments**

The iKAP CRC mouse model (*Villin-Cre-ERT;Apc<sup>lox/lox</sup>;Trp53<sup>lox/lox</sup>;tet-O-LSL-Kras<sup>G12D</sup>*) and iAP mouse model (*Villin-Cre-ERT;Apc<sup>lox/lox</sup>;Trp53<sup>lox/lox</sup>*) were previously established and validated for the histopathological identification of invasive and noninvasive tumors, as detailed in a previous publication (Boutin et al., 2017). The iTAP CRC mouse model were established by introducing *LSL-Tert* within iAP model (*Villin-Cre-ERT;Apc<sup>lox/lox</sup>;Trp53<sup>lox/lox</sup>;LSL-Tert*). Mouse colony management and tumor observations via colonoscopy followed established protocols (Boutin et al., 2017). To induce colorectal tumors in iKAP, iAP, and iTAP mice, a 20 µl solution of 4-OHT (1 mg/mL) in 100% ethanol was directly injected into the distal colon lumen. This was followed by DOX water feeding (200 mg/kg) when the mice were between 10 to 16 weeks old. The treatments described in this study were initiated after mice had received one 4-OHT injection and 14 days of DOX water. 4-OHT injected iKAP mice, comprising an equal number of males and females, were randomly assigned to receive either FQI1 or the VEGFA mouse antibody (B20) treatment. FQI1 (1 mg/kg) or its vehicle (phosphate-buffered saline + 0.4% DMSO) were administered five days a week, while B20 (10 mg/kg) or an IgG isotype control (10 mg/kg)

were administered three times a week via intraperitoneal injection. Mice were euthanized when they reached a moribund state, and their tumors were collected for analysis.

All surgical procedures were conducted with the animals under isoflurane anesthesia, and all animal experiments were approved by The University of Texas MD Anderson Cancer Center's Institutional Animal Care and Use Committee. In the orthotopic xenograft co-injection model, we co-injected  $10^5$  iKAP cells and  $10^4$  fluorescence-activated cell-sorted fibroblasts, either lipid-rich or lipid-scarce, suspended in growth factor-reduced Matrigel, into the cecum wall of the mice. The mice were closely monitored for their survival, and they were euthanized when they became moribund. After 4 weeks from the injection, a subset of mice was sacrificed to measure tumor volumes. In the syngeneic transplantation and xenograft tumor models, we injected  $10^5$  *Tfcp2*-engineered iKAP cells suspended in growth factor-reduced Matrigel subcutaneously. For the syngeneic transplanted tumors, they were collected after 4 months, while the xenograft tumors were harvested after 1.5 months.

### **Plasmids, viral transfections, and cloning**

Four guide RNAs targeting *Tfcp2* were designed using CHOPCHOP (Labun et al., 2019) and screened for their efficacy in reducing messenger RNA (mRNA) and protein levels by at least 80%. The sequences of the guide RNAs were 5'-GACGACGTGATCCAAATCTGCGG-3' and 5'-GCCTGTCGTGGAACACTACGCGG-3'. These guide RNAs were inserted into LentiCRISPR v2 plasmids following the standard protocol (Sanjana et al., 2014). LentiCRISPR v2 was generously provided by Feng Zhang (Addgene plasmid # 52961, <http://n2t.net/addgene:52961>; RRID, Addgene\_52961). Colonies were generated from single cells through serial dilution of each m*Tfcp2* knockout

clone in a 96-well plate. After assessing the knockout efficacy of Tfc2 in each colony, two single clones from the guide RNAs knockout cells were designated as cell lines Tfc2-KO1 and Tfc2-KO2. Four short hairpin RNAs targeting Tfc2 in the pLKO.1 vector (Sigma) were screened, and those that effectively reduced mRNA and protein levels by at least 80% were selected. The chosen clones were TRCN0000218063, TRCN0000085495, and TRCN0000225944 (Sigma) for further use. Plasmids for Tfc2 overexpression were purchased from GenScript (NM\_033476.3; cloning Tfc2 protein-coding sequence into pInducer20 vector, mTfc2-DYK\_pInducer20). Lentiviral particles (8 µg) were generated by transfecting 293T cells with the packaging vectors psPAX2 (4 µg) and pMD2.G (2 µg). The lentiviral particles in the medium were collected 48 and 72 hours after transfecting the 293T cells, and the medium was filtered through a 0.45-µm filter (Corning; 430514). The viral medium was used in a 1/3 dilution of complete medium for cell culture. After 24 hours, fresh DMEM was provided, and at 48 hours, cells were selected following 72 hours of treatment with Puromycin (2 µg/mL). The cell lines were then cultured in complete medium.

### **Immunoblotting**

Immunoblotting was conducted following the standard protocol outlined in the R&D Systems Quality Control Western Blot Protocol. Antibodies, including β-actin (Sigma, #A3854), vinculin (Millipore 05-386), Bmp4 (Abcam, ab124715), Bmp2 (Abcam, ab82511), Wnt5a (Abcam, ab229200), Wnt5b (Abcam, ab94914), Wnt10b (Abcam, ab70816), insulin (Abcam, ab181547), KRAS<sup>G12D</sup> (Cell Signaling, 14429S), and Tfc2 (Cell Signaling, 80784S), were procured for the analysis. Quantification was carried out using Image J software, and the results were normalized using the first control band.

### **IHC and immunofluorescence**



Invasive iKAP, non-invasive iAP, and non-invasive iKAP–DOXoff (KRAS\*–off) CRC tumors were obtained from micro-dissected localized adenomas and invasive adenocarcinomas. These tumors were subsequently subjected to IHC and immunofluorescence analyses as described below.

IHC was performed following R&D Systems' Protocol for the Preparation and Chromogenic IHC Staining of Frozen Tissue Sections and Protocol for the Preparation and Chromogenic IHC Staining of Paraffin–embedded Tissue Sections. Lipid droplet staining by oil red and/or LipidTOX were performed on frozen tissue sections. Antibody staining was done on paraffin–embedded tissue sections after antigen retrieval using a pressure cooker (95 °C for 30 min followed by 120 °C for 10 s) and incubation in antigen–unmasking solution (Vector Laboratories). For frozen tissue sections, antibody and lipid droplet staining was performed after 4% formalin fixation. Oil Red O Stain Kit (Lipid Stain; ab150678) was used for lipid droplet staining. The antibodies used included Pdgfra (Cell Signaling, #3174), Lpl (Invitrogen, PA585126), KRAS<sup>G12D</sup> (Cell Signaling, 14429S), Thy1 (eBioscience, 14–0900–81), Col3a1 (proteintech, 22734–1–AP), Fabp4 (Abcam, ab92501), Dlk1 (Abcam, ab119930), Tcf21 (Invitrogen, PA5116012), Vegfa (Invitrogen, MA5–32038), and Cd31 (Invitrogen, PA5–16301). Slides were scanned using a Panoramic 250 Flash III scanner (3DHISTECH Ltd), and images were captured using Panoramic Viewer software (3DHISTECH Ltd). IHC quantification was conducted following bio–protocol (Crowe et al., 2019) to measure 3,3'-diaminobenzidine staining and quantify the average pixel intensity. Immunofluorescence was performed using the Protocol for the Preparation and Fluorescent IHC Staining of Frozen Tissue Sections (R&D Systems). Purchased lipid–staining dyes included HCS LipidTOX Deep Red Neutral Lipid Stain (Invitrogen, H34477) and HCS LipidTOX Red Neutral Lipid Stain (Invitrogen, H34476). Antibodies included those specific for  $\alpha$ SMA (Abcam, ab124964), Cd326 (eBioscience, 11–5791–82), Dlk1 (Abcam, ab119930), Fabp4 (Abcam, ab92501), Col3a1 (proteintech, 22734–1–AP), Lpl (Millipore,

MABS1270), Pdgfr $\alpha$  (Cell Signaling, #3174), and Cd31 (Invitrogen, PA5–16301). Images were captured using a fluorescence microscope (Leica DMI8). Quantification was performed using Fuji (Schindelin et al., 2012) and Image J (Schneider et al., 2012).

### **Flow cytometry and sorting**

iKAP and iAP tumors were dissociated following the protocol outlined in "Dissociation of Single Cell Suspensions from Human Breast Tissues" available at protocols.io (<http://dx.doi.org/10.17504/protocols.io.t3aeqie>). The dissociated primary cells were subsequently stained with antibodies and/or dyes, including Cd326 (eBioscience, 11–5791–82), Cd45 (Biolegend, 103137), Cd31 (Biolegend, 102427), CD140a (Biolegend, 135906), and LipidTOX Deep Red Neutral Lipid Stain (Invitrogen, H34477). After washing twice with cold phosphate–buffered saline, lipid–rich CAFs and endothelial cells were analyzed using a flow cytometer (BD LSRFortessa™ X–20 Cell Analyzer) or were flow–sorted using a BD FACSAria Flow Cytometer.

### **Lipid–sparse CAFs/myofibroblasts isolation**

Lipid–sparse CAFs were isolated by gating on CD326–, CD45–, CD31–, PDGFR $\alpha$ –, and LipidTOX<sup>low</sup> markers. These lipid–sparse CAFs were subsequently cultured in a 2D culture dish to expand myofibroblasts and exclude pericytes. The expansion process followed established protocols available in JoVE and MIMB (Khan et al., 2016; Boroujerdi et al., 2014). In brief, cell selection was carried out by culturing the cells in RPMI 1640 medium (Gibco; 11875-093) supplemented with 10% FCS, 50  $\mu$ M 2-mercaptoethanol (Sigma; M6250-10ML), 100  $\mu$ M asparagine (Sigma; PHR2350), 2 mM glutamine (Sigma; 1294808), and 1% Antibiotic–Antimycotic (Gibco; 15-240-062) on a 2D culture dish (Corning; 430167).

Pericytes grow in Pericyte growth medium, including Pericyte Growth Supplement (ScienCell 1252, San Diego, CA), in Pericyte Medium (ScienCell 1201), on Collagen I-coated plates. After expanding the myofibroblasts through four subcultures, cells were validated by measuring *Acta2*, *Rgs5*, and *Pdgfra* expression levels through RT-qPCR and immunofluorescence staining. The validated myofibroblasts were then employed for in vivo tumor co-injection assays.

### **ChIP-qPCR and Luciferase Reporter Assay**

The ChIP-qPCR procedure was conducted following a previously established standard protocol (Terranova et al., 2018). In brief, iKAP cells were crosslinked with 1% paraformaldehyde for 10 minutes, followed by quenching the reaction with glycine for 5 minutes at room temperature. Subsequently, the cells were lysed for 30 minutes with ChIP lysis buffer (Terranova et al., 2018) on ice. Chromatin fragmentation was carried out using a Diagenode BioruptorPico sonicator (45 cycles, each consisting of 30 seconds on and 30 seconds off). The solubilized chromatin was then subjected to incubation with a Tfc2 antibody (Cell Signaling, 80784S) in a 1:100 dilution along with Dynabeads (Life Technologies) at 4°C overnight. Following this, the immune complexes underwent a series of washes: 3 times with RIPA buffer, once with RIPA-500, and once with LiCl wash buffer. Elution and reverse crosslinking were carried out overnight at 65°C using a direct elution buffer containing proteinase K (20 mg/mL). The eluted DNA was purified using AMPure beads (Beckman-Coulter) and subsequently utilized for qPCR. Three primer pairs each for *Bmp4* and *Wnt5b* were employed (Supplementary Table S4).

To perform the luciferase reporter assay, the promoter region of human *BMP4* and *WNT5B* (-1500 to +500 bp) was first amplified via PCR. Subsequently, it was inserted into the pGL3

vector (Addgene: E1751) to create the corresponding reporter constructs. The luciferase reporter assay was carried out by transfecting these reporter constructs along with the Renilla luciferase vector into iKAP TFCP2 knockout and rescued cell lines. Cells were collected for analysis 24 hours post-transfection, and luciferase activity was quantified.

## **PGE2 ELISA**

The analysis of PGE2 was conducted using the Prostaglandin E2 ELISA Kit according to the manufacturer's instructions (Abcam, ab133021). In brief, tumor samples were homogenized, and the supernatant was collected after centrifugation for quantifying the PGE2 levels. Furthermore, conditioned media from 3T3L1 cells cultured with iKAP–DOXon and –DOXoff CM were also collected to assess PGE2 levels.

## **Adipokine array**

An adipokine array was carried out using the Proteome Profiler Mouse Adipokine Array Kit in accordance with the manufacturer's instructions (R&D Systems; ARY013). In summary, cell lysates were diluted, combined with a mixture of biotinylated detection antibodies, and then exposed to a Proteome Profiler Mouse Adipokine Array. Control antibodies provided by the kit were utilized as reference points located in the upper left corner of the arrays.

## **Angiogenesis assay**

A human umbilical vein endothelial cell (HUVEC) tube formation assay was conducted using conditioned medium (CM) obtained from lipid-rich CAFs. CM derived from DLD1-KRAS<sup>G12D</sup>-educated hMSCs was incubated with HUVEC cells on Matrigel (Corning, 47743-

722), and an online tool for image analysis, Wimasis Image Analysis (<https://www.wimasis.com/en/>), was employed to assess tube formation parameters, including the percentage of covered area, total tube length (in pixels), total branching points, and total loops.

### **Real-time quantitative PCR (RT-qPCR)**

Cell pellets were obtained from the iKAP cell line, sorted lipid-rich fibroblasts, 3T3L1 and hMSCs cultured in conditioned medium, and iKAP cell lines treated with FQI1. mRNA was extracted using the RNeasy Mini Kit (Qiagen), followed by reverse transcription into cDNA using the OneScript Plus cDNA Synthesis Kit (ABM; G236). RT-qPCR was performed using SYBR Green PCR Master Mix (Thermo Fisher Scientific) on a 7500 Fast Real-Time PCR Machine (Applied Biosystems). Gene expression levels were normalized using actin and/or Ywhaz, which serves as an internal control gene for adipocytes (Perez et al., 2017). Detailed qRT-PCR primer information can be found in Supplementary Table S4.

### **RNA sequencing and analysis**

Prior to conducting RNA sequencing, iKAP and iAP tumors underwent assessment for KRAS\* expression through various methods, including immunohistochemistry (IHC) and immunofluorescence (IF) for GFP, which serves as a marker for enema OHT/Cre-induced reporter activation. The tumor stages were verified by a gastrointestinal pathologist who was blinded to the sample identities. Tissues for RNA isolation were obtained from micro-dissected localized adenomas and invasive adenocarcinomas (T4).

The RNA sequencing of CRC GEM tumors followed the procedure outlined in Boutin et al. 2017, and the resulting data were deposited in the National Center for Biotechnology Information under the SRA number SRP097890. In brief, cells were initially lysed using Buffer RLT and subsequently purified with TRIzol Reagent (Life Technologies) and chloroform. The subsequent steps were carried out according to the RNeasy Mini Kit protocol. RNA sequencing libraries were constructed, and the samples were processed on an Illumina HiSeq 2000 at The University of Texas MD Anderson Cancer Center Sequencing and Microarray Core Facility. Transcriptome reads were aligned to the reference mouse genome mm10, normalized, and quantified as fragments per kilobase per million mapped fragments (FPKM) values using HTSeq-count. A differential gene expression analysis was conducted based on the results derived from a negative binomial distribution. Genes were compared across several groups, including iAP vs. iKAP, iKAP vs. iKAP DOX-off, high vs. low lipid-rich CAF scores, and high vs. low *Tfcp2* scores. The gene signatures associated with lipid-rich CAFs can be found in Supplementary Tables S1 and S2. The gene signatures regulated by *TFCP2* and *SRY* were obtained from GSEA datasets (C3 TFT). The results of these comparisons were subsequently subjected to Gene Set Enrichment Analysis (GSEA) and heatmap analyses.

### **Single cell RNA sequencing and analysis of mouse and human CRC**

Three independent samples were collected for each of the following categories: invasive iKAP, non-invasive iAP, and non-invasive iKAP-DOXoff (*KRAS\**-off) CRC tumors. These samples were obtained by micro-dissecting localized adenomas and invasive adenocarcinomas. Tumor collection took place two months after the initiation of TAM/DOX tumor induction, and each tumor measured approximately 1 cm<sup>3</sup> in size. In the case of the iKAP-DOXoff (*KRAS\**-off) CRC tumors, doxycycline was discontinued for seven days after seven weeks of

TAM/DOX tumor induction. Additionally, three independent samples were collected for each of the iTAP-G0 (telomere intact) and iTAP-G4 (telomere shortened, as validated in Mariela Jaskelioff et al., 2011) categories by micro-dissecting tumor parts and potentially invasive tissues. These tumors were harvested freshly and used for tumor dissociation and subsequent single-cell sequencing analyses.

Single-cell RNA sequencing (scRNA-seq) was conducted at MD Anderson's CPRIT Single Core. The procedure followed the Single-Cell Chromium 3' protocol (10X Genomics; PN-120237) with V3 chemistry reagents (10X Genomics). Barcoding and library preparation were performed, and the libraries containing barcoded single-cell transcriptomes were sequenced with 100 cycles on an S2 flowcell using the Novoseq 6000 system (Illumina). Data processing was accomplished using the CASAVA 1.8.1 pipeline (Illumina), and sequence reads were transformed into FASTQ files and UMI (Unique Molecular Identifier) read counts using the CellRanger software (10X Genomics). For in-silico analyses, raw count matrices were converted into Seurat objects for further investigation. The quality of the scRNA-seq data was assessed using metrics such as the percentage of mitochondrial genes (percent.mt) per cell and the number of unique molecular identifiers (UMI count). Cells that did not meet quality criteria, with a UMI count below 800, a percent.mt exceeding 25%, and doublets expressing markers of multiple cell types, were excluded. To mitigate batch effects, we applied the PCA-based integration method in Seurat. Subsequently, we performed unsupervised dimension reduction and clustering to identify cell populations. Cell identities within each cluster were determined based on canonical marker genes and cluster-specific differential genes. Module score plots were generated using Seurat's AddModuleScore, incorporating an adipocyte gene signature (Franzen et al., 2019) along with a combination of classic adipocyte and pre-adipocyte genes, including markers for mature adipocytes (*Fabp4*, *Lpl*, *Plin4*, *Dcn*, *Dpt*, *Cfd*, *Ccl2*; regulatory TFs: *Pparg*, *Cebpa*,

*Cebpb*) and pre-adipocytes (*Dlk1*, *Dlk2*, *Lpl*, *Plin4*; regulatory TFs: *Zfp423*, *Tcf21*). All single-cell RNA sequencing data from GEM CRC (Genetically Engineered Mouse Colorectal Cancer) experiments were deposited in the National Center for Biotechnology Information under the accession number GSE229559. The R code and processed data are available on Code Ocean at <https://codeocean.com/capsule/1830109/>.

Human research adhered to the ethical guidelines of the Helsinki Declaration. Tumor specimens from human participants were collected at The University of Texas MD Anderson Cancer Center under the approved Institutional Review Board protocol LAB10-0982 (Principal Investigator: Dr. Scott Kopetz) with the written informed consent of each participant. Fresh specimens were promptly transported in sterile cold DMEM medium to MD Anderson's CPRIT Single Core for single-cell isolation, scRNA sequencing, and subsequent analyses, as outlined earlier. Clinical data, encompassing tumor location, gender, age, stage at collection, microsatellite (MS) status, and genotype, are detailed in Supplementary Table S5. The raw data from single-cell RNA sequencing and the processed datasets from human CRC specimens have been made available on the Gene Expression Omnibus under accession number GSE231559.

### **Computational analysis of TCGA–COAD data**

For the analysis of human CRC data, we sourced gene expression and survival data from the TCGA-COAD datasets and/or datasets available on cBioPortal (<https://www.cbioportal.org/>). Our data collection encompassed critical information such as tumor genotypes, patient survival rates, tumor stages, tumor subtypes, and patient treatments, all retrieved from cBioPortal. Employing R packages, specifically DESeq2, GSVA, and pathfindR, we conducted comprehensive analyses to investigate pathways



enriched in KRAS\* patients, KRAS-related genes, lipid-rich CAF scores, TFCP2 scores, and their implications for patient survival. In a nutshell, our pathway analysis involved identifying differentially expressed genes in KRAS\* patients using DESeq2, followed by GSEA analyses or utilizing pathfindR to uncover enriched pathways. For evaluating lipid-rich CAF scores and TFCP2 scores, we utilized GSVA with the lipid-rich CAF gene signature (Supplementary Table S1 and S2) and the TFCP2-regulated gene signature (obtained from GSEA datasets, C3 TFT) from both KRAS\* and KRASWT patients.

### **The analysis of KRAS\* downstream TFs**

The downstream transcription factors (TFs) associated with KRAS\* were identified through a comprehensive analysis. This analysis involved examining the consensus TF binding motifs located in the promoters of BMP4 and WNT5B using PROMO software. Additionally, we considered the TF signatures that were modulated in a KRAS\*-dependent manner in both murine and human CRCs, as determined through GSEA analyses. The compiled lists of candidate TFs from these three gene sets are provided in Supplementary Table S3.

### **Statistical analysis**

We conducted all two-sample statistical analyses using Student's t-test, two-sided, and presented the results as the mean  $\pm$  standard deviation (SD). The significance analysis of various datasets, including the TCGA colon adenocarcinoma database, GEM RNAseq, scRNAseq, RT-qPCR, IHC quantification, and angiogenesis assay quantification, was carried out in EXCEL and GraphPad Prism 9. Survival data from the TCGA colon adenocarcinoma database and GEM mice were analyzed using the Log-rank (Mantel-Cox)

test in GraphPad Prism 9. The corresponding p-values are displayed in the graphs, with a significance threshold of  $p < 0.05$ .

### **Data Reproducibility and Availability**

The RNA sequencing data of CRC GEM tumors have been submitted to the National Center for Biotechnology Information under SRA number SRP097890. The GEM iKAP and iAP CRC scRNA sequencing data from this study have been made publicly accessible on Gene Expression Omnibus (GEO) at GSE229559. The R code and R processed data are deposited in the Code Ocean capsule at <https://codeocean.com/capsule/1830109/>. To access the GEM iTAP-G0 and iTAP-G4 CRC scRNA sequencing data generated in this study, interested researchers should request access from Dr. DePinho. The human CRC scRNA sequencing data generated in this study are also available to the public on Gene Expression Omnibus under accession number GSE231559.

**CHAPTER 3:**  
**KRAS\* REGULATES CRC STROMA**  
**IN THE ENRICHMENT OF LIPID-RICH CAFs**

## **CHAPTER 3: KRAS\* REGULATES CRC STROMA IN THE ENRICHMENT OF LIPID-RICH CAFs**

Content of this chapter is partly based on the following manuscript:

Hsu, W.H., LaBella, K. A., Lin, Y., Xu, P., Lee R., Hsieh, C.E., Yang, L., Zhou, A., Blecher, J. M., Wu, C. J., Lin, K., Shang, X., Jiang, S., Spring, D. J., Xia, Y., Chen, P., Shen, J. P., Kopetz, S., DePinho, R. A. (2023) "Oncogenic KRAS drives lipo-fibrogenesis to promote angiogenesis and colon cancer progression" *Cancer Discov*, 10.1158/2159-8290.CD-22-1467

### **3.1 Preliminary research and rationale**

To uncover pathways and processes associated with both KRAS\* signaling and disease progression in CRC, we conducted a gene set enrichment analysis (GSEA) using 19 bulk tumor RNA sequencing profiles. We aimed to identify genes that are upregulated in iKAP murine tumors (with active *Kras*\*) when compared to iAP murine tumors (control, lacking *Kras*\* transgene), as well as in invasive primary tumors in comparison to noninvasive primary tumors. The intersection of these *Kras*\* and progression transcriptomes revealed a prominent presence of the adipogenesis pathway in invasive *Kras*\*-expressing CRC (Fig. 1A).

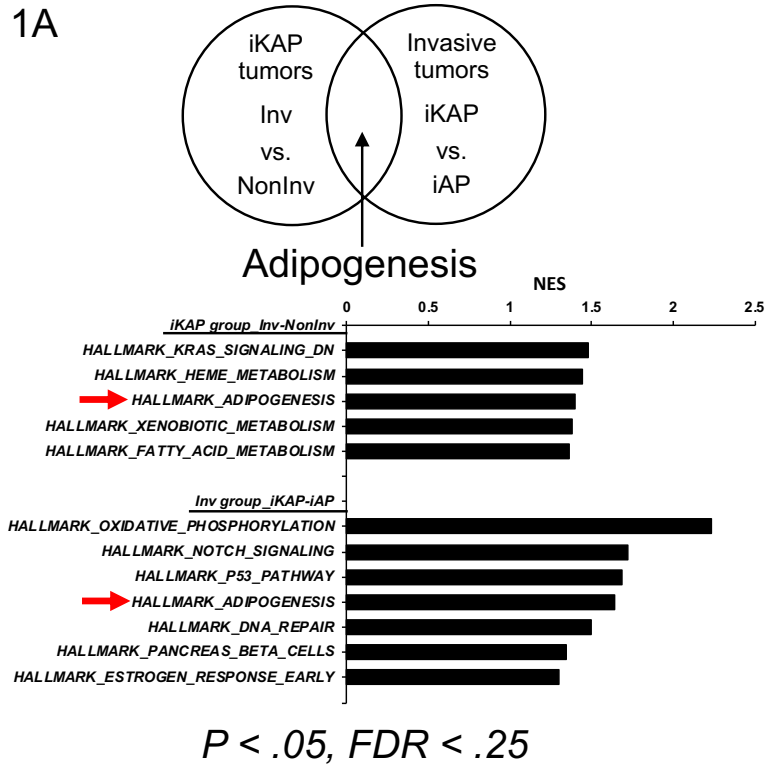


Figure 1A. GSEA transcriptomic profiling of iKAP vs. iAP tumors and invasive (Inv) vs. noninvasive (NonInv) tumors shows enriched hallmark pathways.  $N \geq 4$ . Please see Methods “RNA sequencing and analysis” for details of sample collection and characterization of *Kras* wild type, *Kras* mutation, invasive and non-invasive tumors. Red arrows indicate the adipogenesis pathway. NES, normalized enrichment score.

These computational findings aligned with our tumor histology results, which exhibited a significant increase in lipid droplet abundance within the invasive iKAP tumor stroma when contrasted with non-invasive iAP controls (Fig. 1B and 1C). Importantly, the lipid-rich iKAP tumor stroma did not co-localize with  $\alpha$ SMA and epithelial cellular adhesion molecule (Cd326) staining (Fig. 1B). Instead, it co-localized with delta-like homolog (Dlk1), a marker indicative

of preadipocytes and lipid-rich fibroblast progenitors. This further underscores the enrichment of an adipocyte-like lineage in the stromal environment of *Kras*\*-expressing CRC (Fig. 1C).

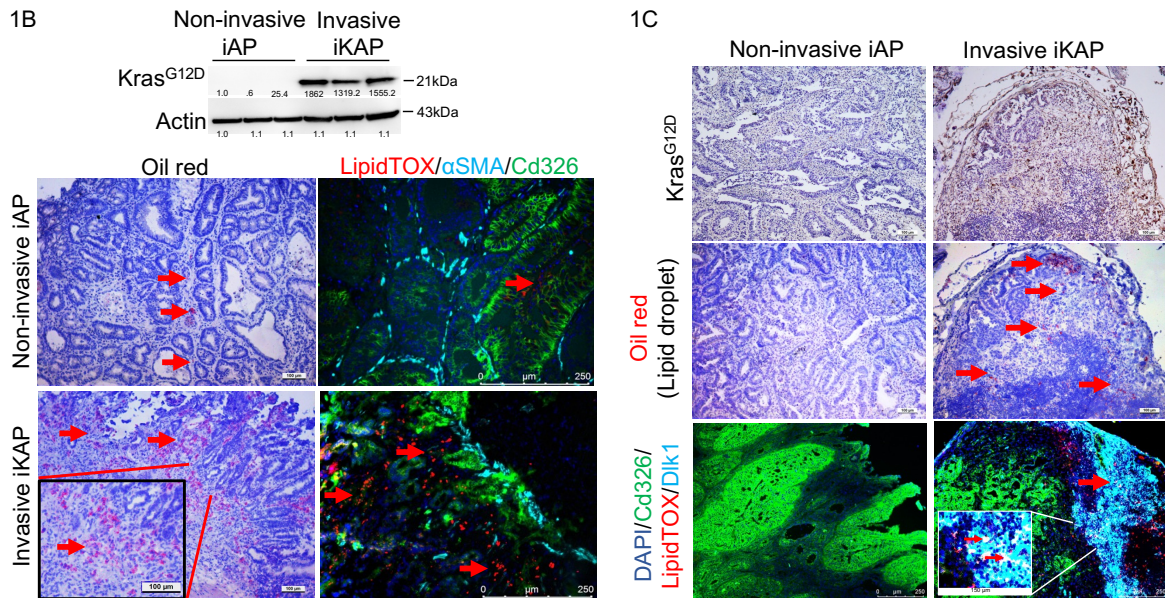
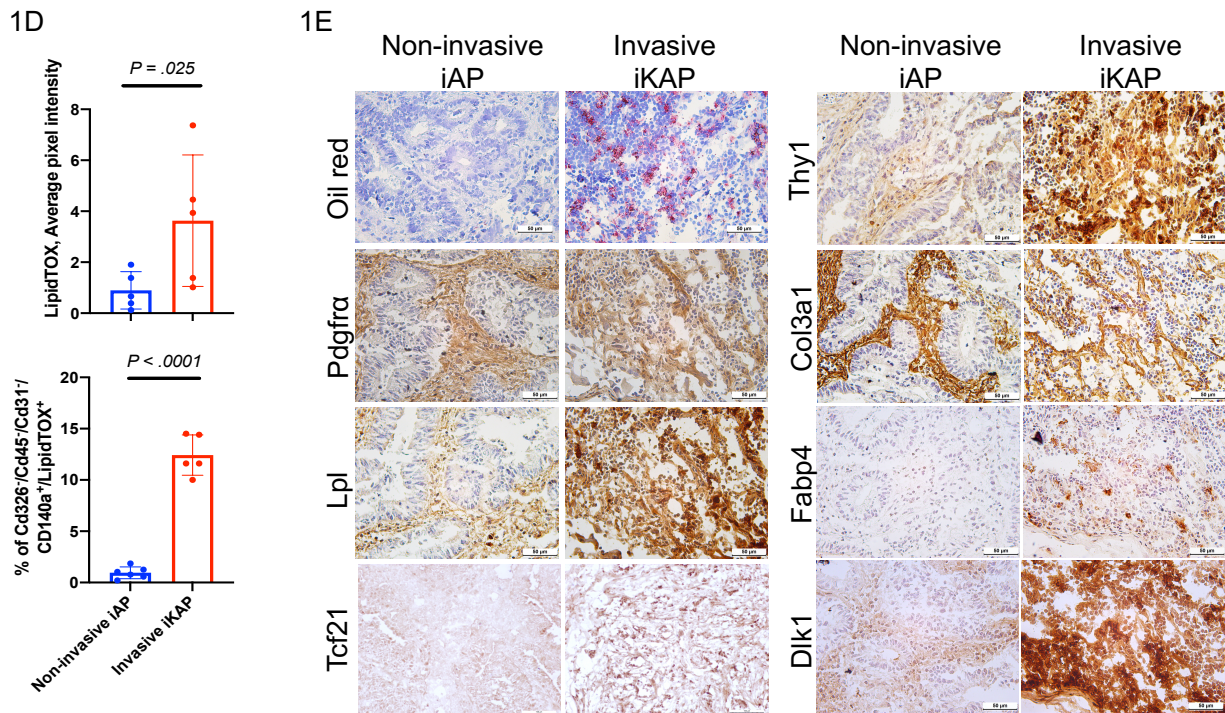


Figure 1B. Immunoblotting of *Kras*<sup>G12D</sup> in non-invasive iAP and invasive iKAP bulk tumor lysate (upper). Immunohistochemical staining of lipid droplets (oil red) and immunofluorescence staining of lipid droplets (LipidTOX), Cd326 and  $\alpha$ Sma in colorectal cancer (CRC) tumors from invasive iKAP and non-invasive iAP genetically engineered mouse (GEM) models (lower). Please see Methods for details of sample collection of invasive iKAP and non-invasive iAP tumors. Red arrows indicate lipid droplets. Scale bar, 100  $\mu$ m and 250  $\mu$ m; N = 6 biological replicates.

Figure 1C. Immunohistochemical and immunofluorescence staining of lipid droplets (oil red) and lipid-rich CAF genes in colorectal cancer (CRC) tumors from invasive iKAP and non-invasive iAP GEM models. N = 6 biological replicates. Red arrows indicate lipid droplets.

We employed flow cytometry analysis that focused on LipidTOX+, Pdgfr alpha-positive (Pdgfr $\alpha$ + [Cd140a, a non-myofibroblast marker]), Cd326- (a CRC epithelium marker), Cd45- (an immune cell marker), and Cd31- (an endothelial marker) cells. This analysis revealed a heightened percentage of lipid-rich CAFs in KRAS\*-expressing invasive iKAP tumors when compared to non-invasive iAP tumors (Fig. 1D). Immunohistochemical (IHC) analyses validated our transcriptomic findings by confirming the enrichment of lipid droplets and markers/regulators of adipocytes, including Dlk1, Tcf21, Fabp4, and Lpl, in Kras\*-expressing invasive iKAP tumors relative to non-invasive iAP controls. Additionally, these analyses indicated the expression of fibroblast markers such as Col3a1, Thy1, and Pdgfr $\alpha$  (Fig. 1E).



**Figure 1D.** The quantification of LipidTOX staining intensity in non-invasive iAP and invasive iKAP tumors (upper panel).  $N = 5$  biological replicates. The percentages of Cd326-/Cd45-/Cd31-/Cd140a+/LipidTOX+ cells in non-invasive iAP and invasive iKAP tumors determined using flow cytometry analysis (lower panel).  $N = 5$  biological replicates. Data represent mean  $\pm$  SD. Student's  $t$  test.

Figure 1E. Immunohistochemical analysis of lipid droplets, non-myofibroblast and adipocyte genes in CRC tumors from invasive iKAP and non-invasive iAP GEM models. Scale bar, 50  $\mu\text{m}$ ; N = 3 biological replicates.

To decipher the *Kras*\*-dependency and stage-specificity of lipid-rich CAF enrichment during CRC development, we assessed lipid-rich CAFs at various stages of tumor progression, including high-, moderate-, and low-grade invasive, as well as non-invasive iKAP and iAP tumors. Notably, positive lipid staining was most abundant in high-grade invasive iKAP tumors compared to moderate- and low-grade invasive, as well as non-invasive iKAP and iAP tumors (Fig. 1F). These results underscore the *Kras*\* dependency and tumor stage specificity of lipid-rich CAF enrichment in the development of CRC.

1F

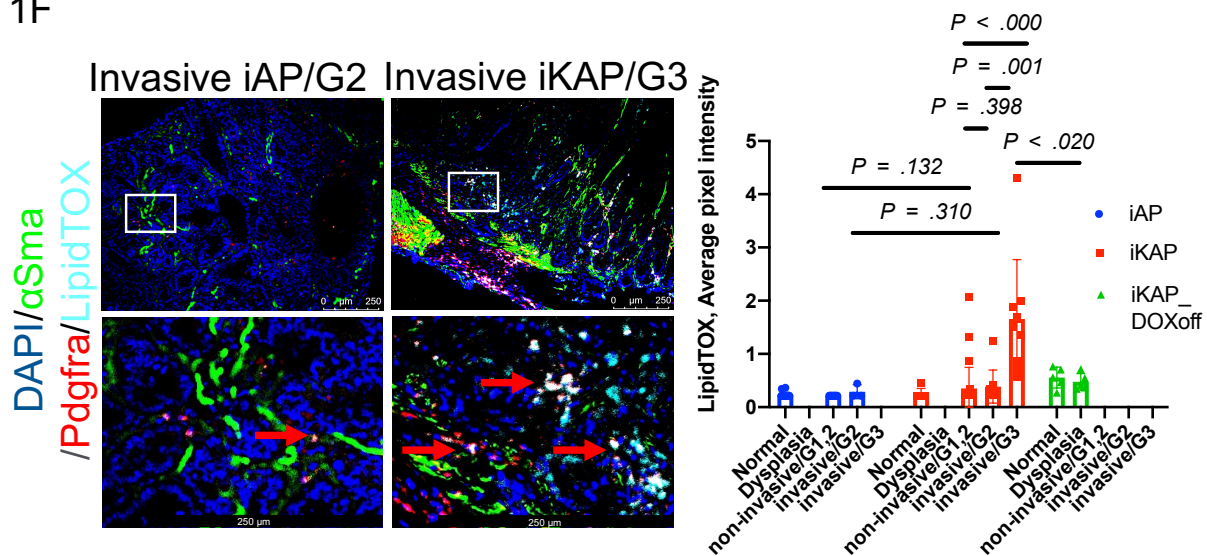


Figure 1F. Immunofluorescence staining of lipid droplets,  $\alpha\text{Sma}$ , and  $\text{Pdgfra}$  in moderate grade (G2) and high grade (G3) invasive iKAP and iAP tumors (grade scored by GI pathologist; blinded) (left panel). White rectangles indicate the enlarged area presented in the lower images. Red arrows indicate the co-staining of  $\text{Pdgfra}$  and lipid droplet. Scale bar, 250  $\mu\text{m}$ .



*µm. Quantification of LipidTOX at different tumor status (right panel). N ≥ 3 biological replicates. Data represent mean ± SD. Student's t test.*

### **3.2 Results**

To further characterize the stromal response driven by Kras\*, we conducted single-cell RNA sequencing (scRNA-seq) comparisons across invasive iKAP, non-invasive iAP, and non-invasive iKAP–DOXoff (KRAS\*–off) CRC tumors. Among the 71,525 cells analyzed, we identified 5,984 stromal cells, including (i) pericytes (enriched for Rgs4 and Rgs5), (ii) three subgroups of endothelial cells (enriched for Pecam1 and Eng), and (iii) six subgroups of fibroblasts (enriched for Pdgfra and Pdpn) (Fig. 1G). The fibroblast subtypes, which include ECM+ CAFs (expressing Col12a1, Col1a2, and Col6a2), Mmp+ CAFs (expressing Mmp13, Mmp10, and Mmp9), Pi16+ CAFs (expressing Pi16, Il33, and Clip), inflammatory CAFs (expressing Cxcl13, Tnfsf13b, and C4b), proliferating fibroblasts, and myofibroblasts (expressing Actg2, Tagln, and Acta2) (Fig. 1G), were defined using previously established markers (Lavie et al., 2022; Deng et al., 2021; Muhl et al., 2020; Taylor et al., 2020; Xie et al., 2018). Importantly, four CAF subgroups stood out for their expression of adipocyte- and adipogenesis-related genes (Fig. 1G, right). For example, ECM+ CAFs express Igf1, which induces lipid production (Smith et al., 2006); Mmp+ CAFs express Nrg1, which fine-tunes white adipose stem cell differentiation (Cordero et al., 2020); Pi16+ CAFs express Pi16+, a marker of Pdgfra+ adipocyte progenitor cells (Han et al., 2021); and inflammatory CAFs express Sfrp2, which enhances the adipogenic differentiation of dental mesenchymal stem cells (Lin et al., 2017).

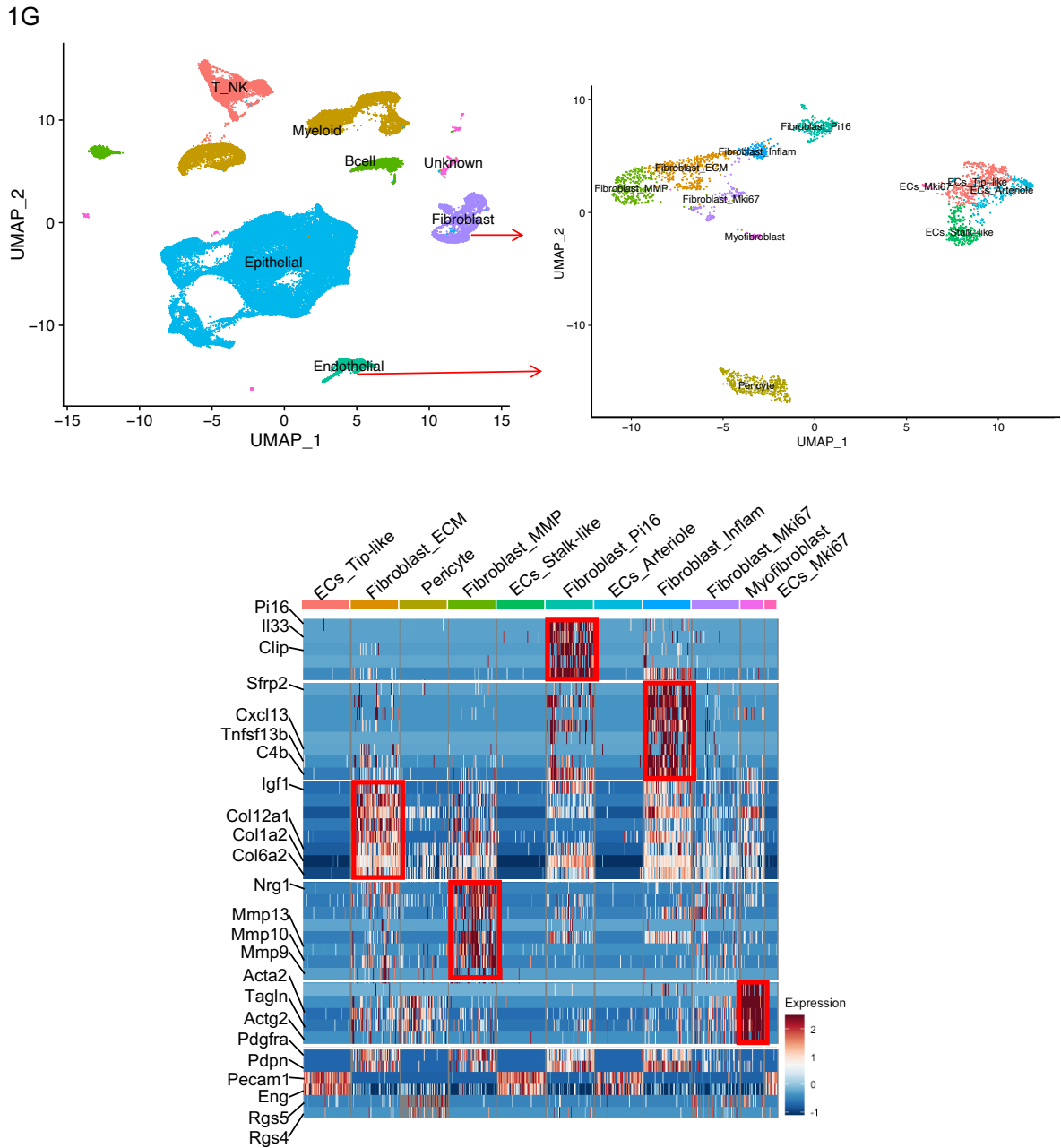


Figure 1G. Single-cell sequencing annotations for all cell types and stroma cells in invasive iKAP, non-invasive iAP, and non-invasive iKAP\_DOXoff tumors (upper panel).  $N = 3$  biological replicates. Heatmap of differential expression marker genes for stroma subgroups (lower panel).  $N = 3$  biological replicates.

To validate these findings, we analyzed scRNA-seq data containing 2,666 stromal cells from six *KRAS* mutant and six *KRAS* wild-type tumors from CRC patients. These human CAF annotations mirrored those in *Kras*<sup>\*</sup> and *Kras* wild-type murine CRC, as reflected by scRNA-seq analyses showing six fibroblast subgroups, including *PI16*<sup>+</sup>, *SFRP*<sup>+</sup>, inflammatory, extracellular matrix (ECM), myofibroblasts, and KI67<sup>+</sup> fibroblasts (Fig. 1H left). Moreover, the *PI16*<sup>+</sup>, *SFRP*<sup>+</sup>, inflammatory, and ECM fibroblasts expressed adipocyte and/or adipogenesis-related genes, including *PI16*, *SFRP2*, *RARRES1*, and *SFRP4*, respectively (Ullah et al., 2013; Guan et al., 2018) (Fig. 1H right).

1H

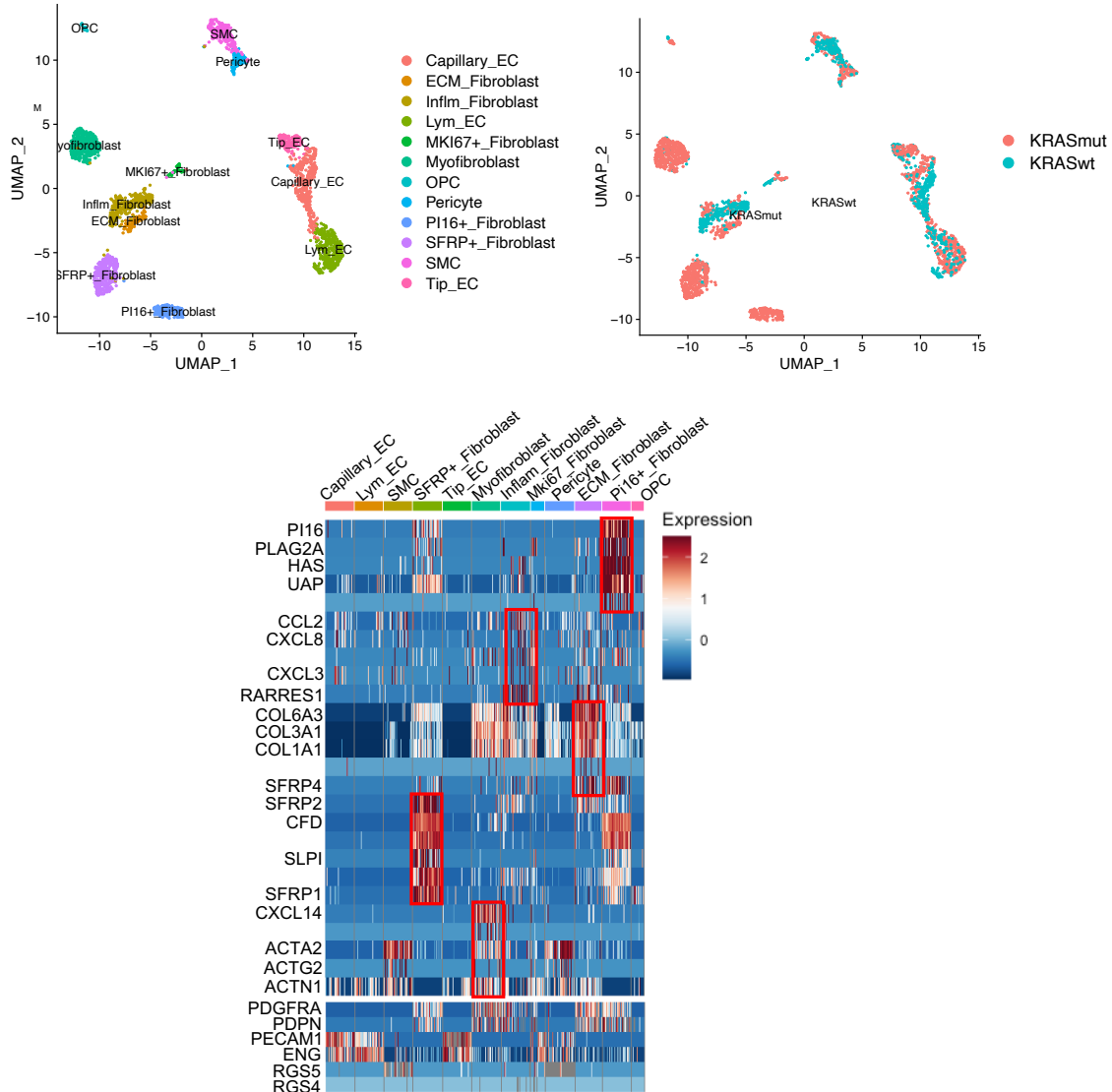
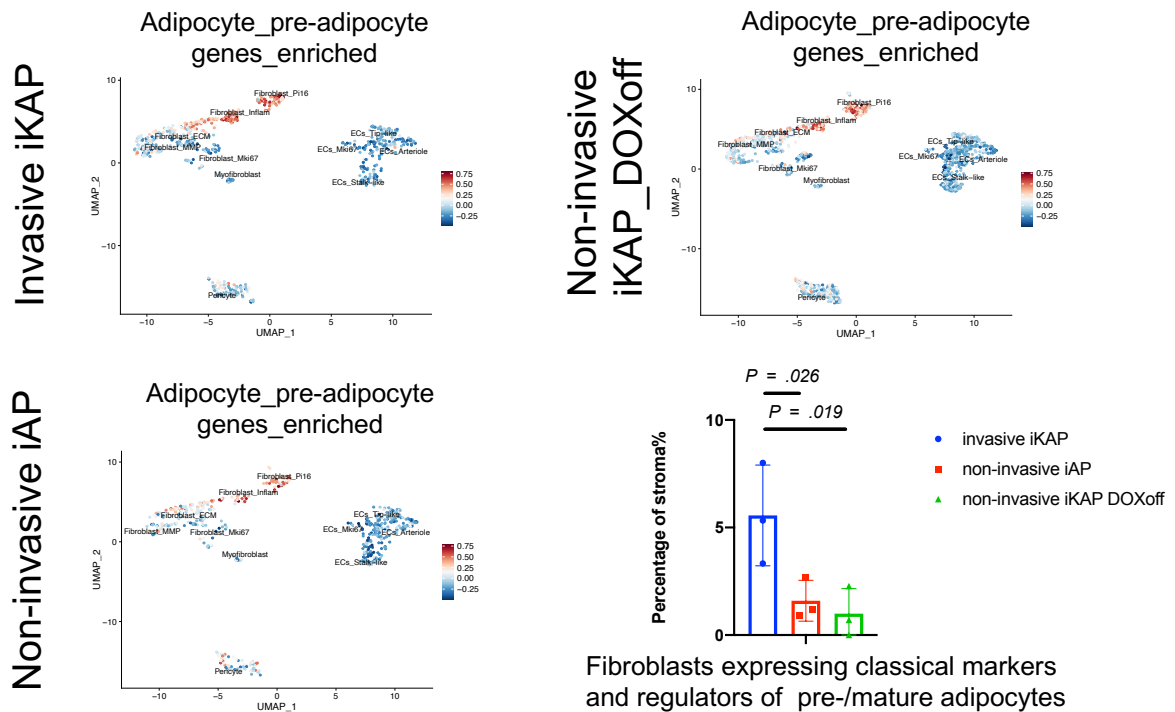


Figure 1H. Single-cell sequencing annotation of stroma cells in human CRC (upper left panel) and of patients with wild type *KRAS* or *KRAS\** (upper right panel). Heatmap of differential expression marker genes of cancer-associated fibroblast (CAF) subgroups (lower panel). *N* = 12 biological replicates. See Methods “Single cell RNA sequencing and analysis of mouse and human CRC” and Supplementary Table S4. OPC: Oligodendrocyte progenitor cells.

Furthermore, we characterized the murine CAF subtypes corresponding to lipid-rich CAFs using gene set module score analyses in murine scRNA datasets. These analyses revealed enrichment of the adipocyte gene signature (Franzen et al., 2019) and a combination of classic adipocyte and pre-adipocyte genes (McGowan et al., 2014; Park et al., 2019; Sanchez—Gurmaches et al., 2016; Goralski et al., 2007; Unamuno et al., 2020) in the four *αSma*–CAF subgroups, namely, inflammatory, *Pi16*+, ECM+, and *Mmp*+ CAFs (Fig. 1I and 1J).

11



1J

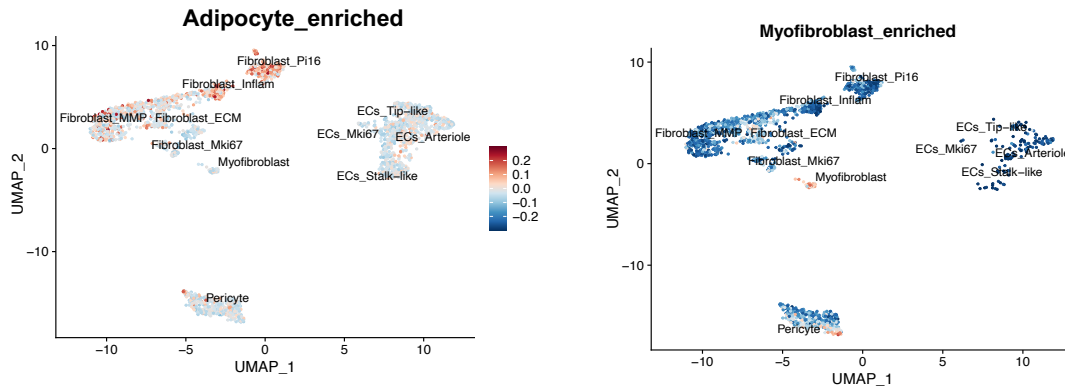
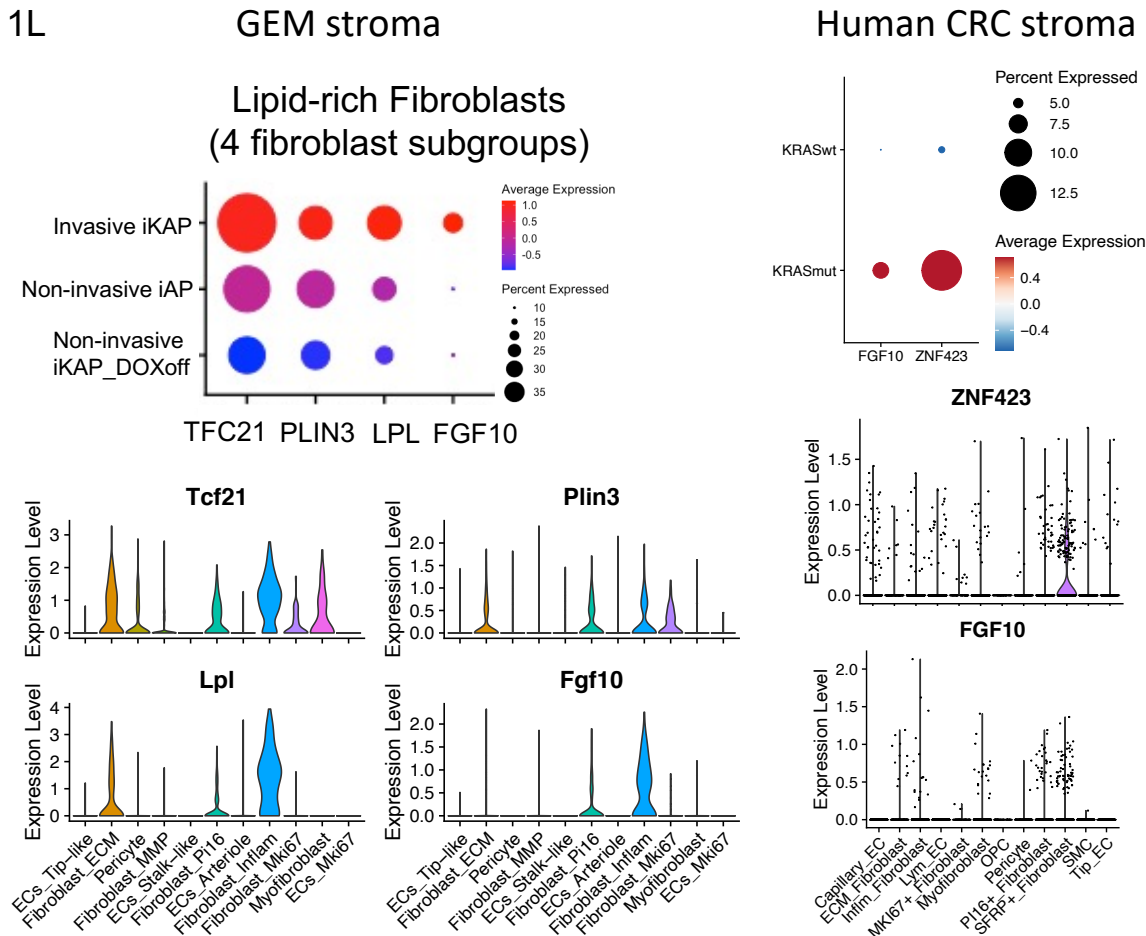
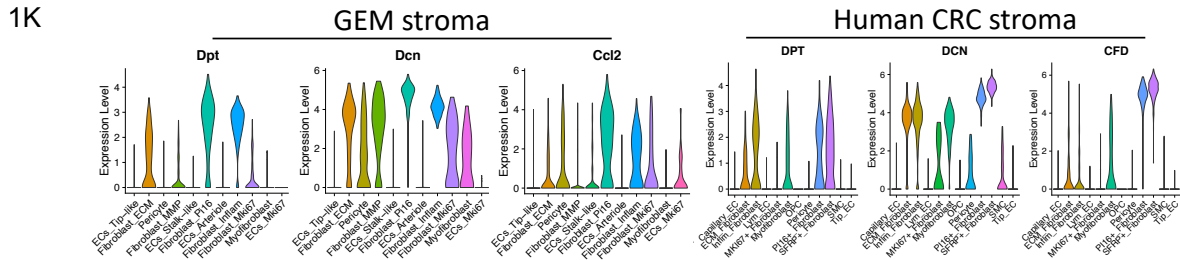


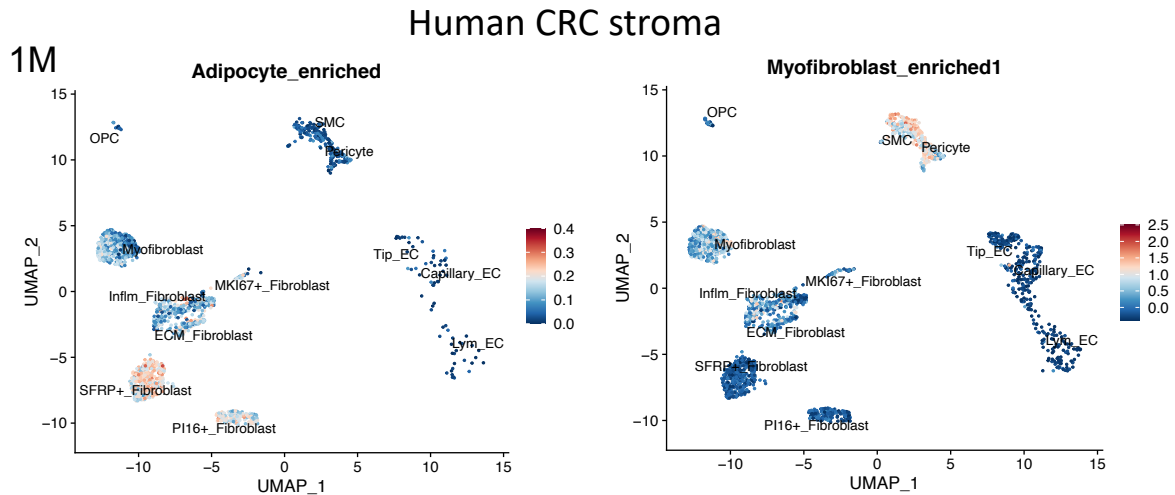
Figure 1I. Adipocyte and pre-adipocyte genes' module score plots of invasive *iKAP*, non-invasive *iAP*, and non-invasive *iKAP\_DOXoff* tumor stroma subgroups as determined using the Seurat's *AddModuleScore* function. Please see Methods "Single cell RNA sequencing and analysis of mouse and human CRC" for details of obtaining module score plots. The percentage of fibroblasts that express classical markers and regulators of pre-/mature adipocytes in tumor stroma (lower right panel).  $N = 3$  biological replicates. Data represent mean  $\pm$  SD. Student's *t* test.

Figure 1J. UMAP plots of adipocytes (PanglaoDB) and myofibroblasts (GSEA) in mouse CRC CAF subgroups from single-cell sequencing as determined using the Seurat *AddModuleScore* function.

These CAF subgroups expressed classic adipokine genes (*Dpt*, *Dcn*, and *Ccl2*; Fig. 1K left) (Goralski et al., 2007; Unamuno et al., 2020) and lipid-rich fibroblast regulators and markers (*Tcf21*, *Fgf10*, *Plin3*, and *Lpl*; Fig. 1L left) (Park et al., 2019). In contrast,  $\alpha$ SMA+ myofibroblastic CAFs showed low or no expression of such signatures and markers, consistent with the absence of lipid droplets in this tumor-suppressive CAF subtype. Correspondingly, the same analyses of human CRC scRNA-seq data revealed enrichment of

an adipocyte gene signature in *PI16+* and *SFRP+* fibroblasts, along with the expression of adipokine genes and lipid-rich fibroblast markers (Fig. 1K-L right and 1M).





*Figure 1K. scRNA datasets show the mRNA expression level of adipokine genes in mouse and human CAF subgroups.*

*Figure 1L. scRNA datasets show the mRNA expression level of lipofibroblast genes in mouse and human CAF subgroups. The average expression scale ranged from -1 to 1 and -0.4 to 0.4. The dot size represents the proportion of expressing cells in each group. N = 3 in mouse scRNA-seq and N = 12 in human scRNA-seq. (biological replicates.)*

*Figure 1M. UMAP plots of adipocytes (PanglaoDB) and myofibroblasts (GSEA) in human CRC CAF subgroups from single-cell sequencing as determined using the Seurat AddModuleScore function.*

Supporting the scRNA-seq characterization of lipid-rich CAFs in vivo, transcriptomic analysis of flow-sorted lipid-rich CAFs (LipidTOX+/Pdgfra+ and Cd326-/Cd45-/Cd31-) showed a lack of  $\alpha$ Sma (Acta2) expression and enrichment of differential expression genes in the four CAF subgroups (Fig. 1N). This observation reflects the association between the lipid-rich fibroblast signature and the four  $\alpha$ Sma- CAF subgroups.

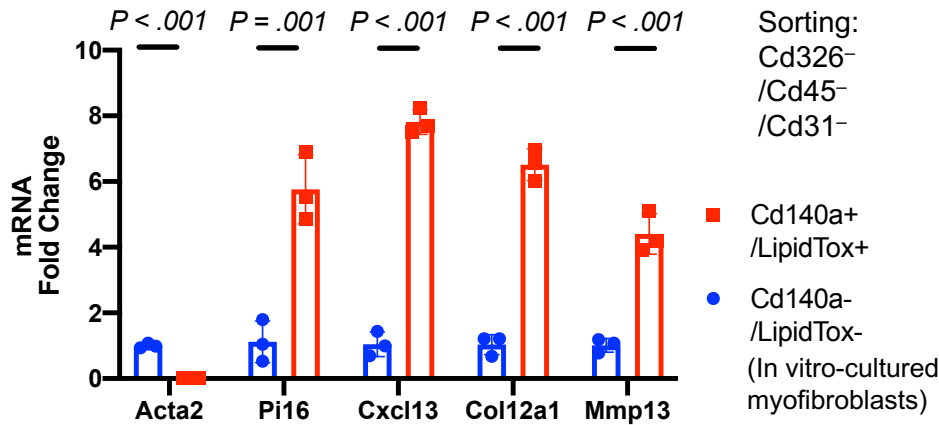


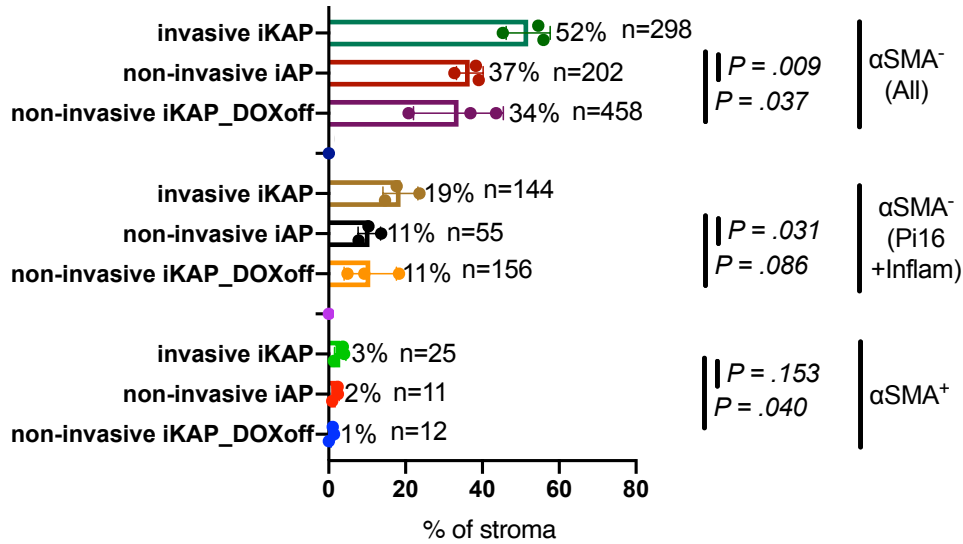
Figure 1N. CAF marker gene expression levels in Cd326-/Cd45-/Cd31-/Pdgfra+/LipidTOX+/-sorted cells and Cd326-/Cd45-/Cd31-/Pdgfra+/LipidTOX- -sorted/cultured myofibroblasts. See Methods for lipid-rich fibroblasts and lipid-sparse fibroblasts (myofibroblasts) collection.  $N = 3$  biological replicates. Data represent mean  $\pm$  SD. Student's *t* test.

Finally, scRNA-seq analysis revealed an increased presence of lipid-rich CAFs in KRAS\*-expressing invasive iKAP tumors compared to non-invasive iAP and KRAS\*-off (no DOX) iKAP controls. These lipid-rich CAFs, characterized by the enrichment of adipocyte gene signatures and pre-/mature adipocyte genes, were most prominent in the *Pi16*+ and inflammatory CAF subtypes (Fig. 1I lower right panel, and Fig. 1O). These findings were consistent with the higher abundance of lipid-rich CAFs (LipidTOX+/Pdgfra+) in KRAS\*-expressing CRC tumors (Fig. 1D). These murine results were in line with observations from KRAS\* human CRC scRNA-seq data, which also showed an increase in lipid-rich CAFs (*Pi16*+ and *SFRP*+ fibroblasts) (Fig. 1P). Additionally, data from The Cancer Genome Atlas (TCGA) comparing *APC*-/*TP53*-/*KRAS*\* to *APC*-/*P53*-/*KRAS*<sup>WT</sup> revealed a positive correlation between KRAS\*-driven CRC and the lipid-rich CAF ( $\alpha$ SMA-) gene signatures (Supplementary Table S1) (Fig. 1Q). Collectively, these findings establish a positive correlation between

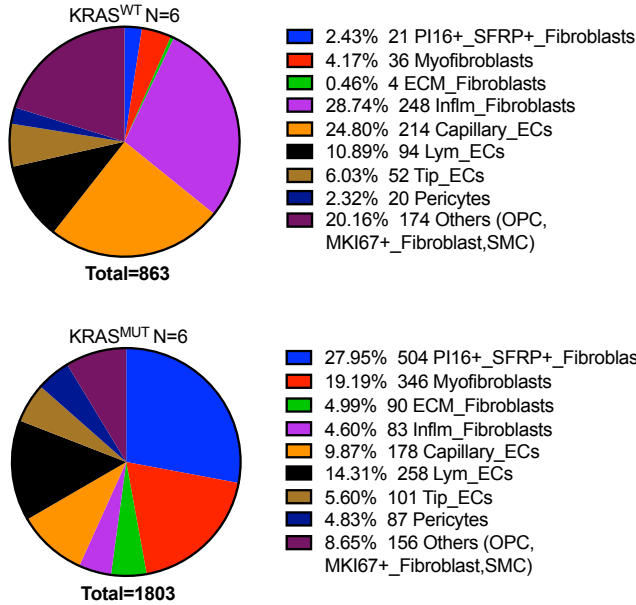


KRAS\*-driven invasiveness and the enrichment of lipid-rich CAFs in both human and murine CRC.

10



1P Human CRC stroma



1Q

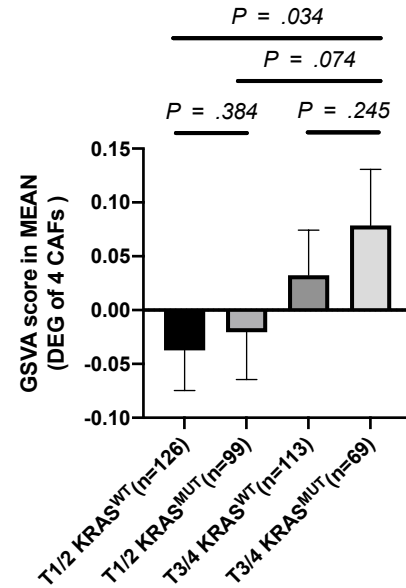


Figure 1O. Proportion of  $\alpha$ Sma- lipid-rich CAF subgroups (the combination of 4  $\alpha$ Sma- CAF subgroups, the combination of inflammatory and Pi16+ CAF subgroups, and  $\alpha$ Sma+ myofibroblasts) in invasive iKAP, non-invasive iAP, and non-invasive iKAP\_DOXoff tumor stroma cells. N = 3 biological replicates. Data represent mean  $\pm$  SD. Student's t test.

Figure 1P. scRNA-seq analyses show the proportion of all stroma subgroups in patients with wild type KRAS or KRAS\*. N =12 biological replicates.

Figure 1Q. The GSEA score analysis of lipid-rich CAFs comparing KRAS\* versus KRAS<sup>WT</sup> and in different tumor grades. Data represent mean  $\pm$  SEM. Student's t test.

**CHAPTER 4:**  
**KRAS\* UPREGULATES PROADIPOGENIC CYTOKINES**  
**TO ORCHESTRATE LIPO-FIBROGENESIS**  
**AND PROMOTE TUMOR GROWTH**

## CHAPTER 4: KRAS\* UPREGULATES PROADIPOGENIC CYTOKINES TO ORCHESTRATE LIPO-FIBROGENESIS AND PROMOTE TUMOR GROWTH

Content of this chapter is partly based on the following manuscript:

Hsu, W.H., LaBella, K. A., Lin, Y., Xu, P., Lee R., Hsieh, C.E., Yang, L., Zhou, A., Blecher, J. M., Wu, C. J., Lin, K., Shang, X., Jiang, S., Spring, D. J., Xia, Y., Chen, P., Shen, J. P., Kopetz, S., DePinho, R. A. (2023) "Oncogenic KRAS drives lipo-fibrogenesis to promote angiogenesis and colon cancer progression" *Cancer Discov*, 10.1158/2159-8290.CD-22-1467

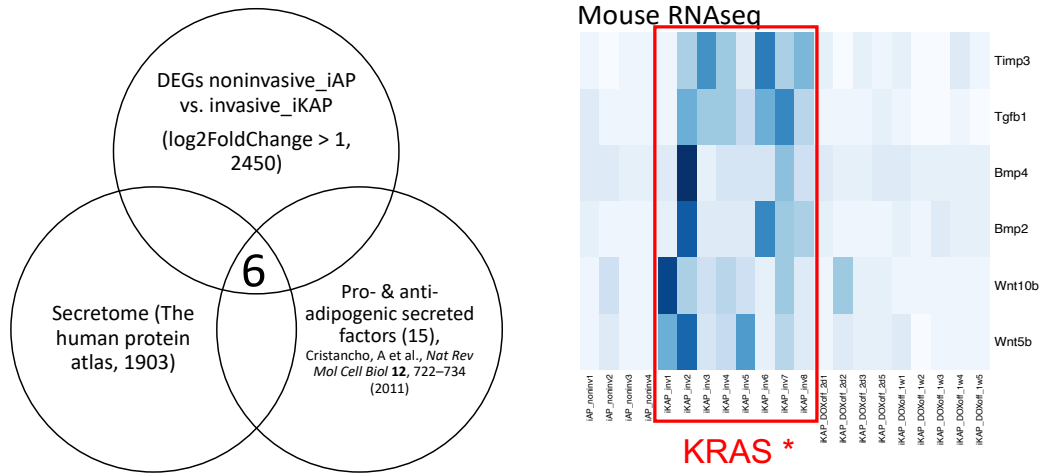
### 4.1 Preliminary research and rationale

The increased presence of lipid-rich CAFs in KRAS\*-expressing tumor stroma led us to investigate the potential for KRAS\* to regulate the expression of proadipogenic factors. Lipo-fibrogenesis appears to utilize mechanisms similar to those driving classical adipogenesis. Specifically, the commitment phase of preadipocytes in lipo-fibrogenesis and adipogenesis is orchestrated by the inhibition of WNT signaling (Christodoulides et al., 2009) and the activation of BMP signaling (Huang et al., 2009). *PDGFR $\alpha$* + preadipocytes accumulate lipids through an FGF10 autocrine loop (Lv et al., 2021), and lipid droplet accumulation can be further enhanced by insulin, cyclic AMP, or glucocorticoids, which upregulate PPAR $\gamma$  and C/EBPs (Cristancho et al., 2011).

In Figure 2A, the overlapping analysis of (i) genes with differential expression in invasive iKAP compared to non-invasive iAP tumors, (ii) the human secretome, and (iii) known pro- and anti-adipogenic secreted factors revealed that Kras\* regulates the expression of six key Bmp and Wnt factors. Furthermore, modulation of Kras\* expression by DOX resulted in significant

changes in the expression of established regulatory factors and markers associated with lipid-rich and proadipogenic processes (Fig. 2A). Additionally, GSEA of stromal populations demonstrated the *Kras*\*-dependent enrichment of two major drivers of preadipocyte commitment: RESPONSE\_TO\_BMP and NEGATIVE\_REGULATION\_OF\_WNT (Fig. 2B).

2A



2B

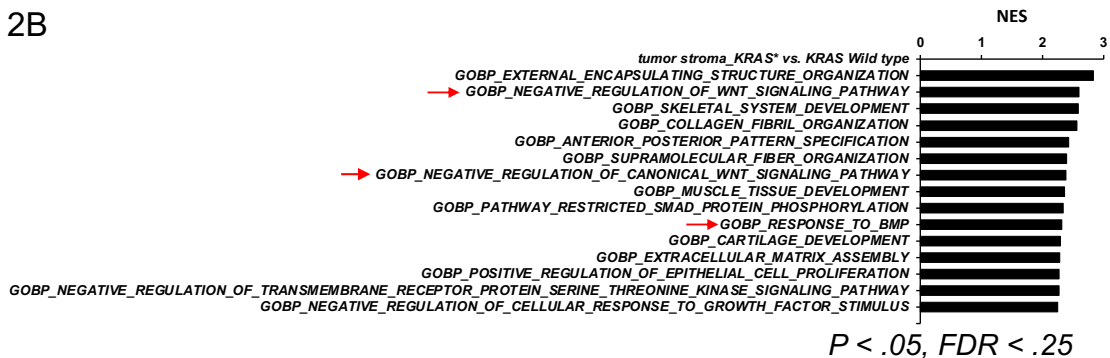


Figure 2A. Venn diagram of the putative secretome that is regulated by *Kras*\* and modulates adipogenesis (left panel). Heatmap representation of the pro- and anti-adipogenic cytokine candidate gene expression in iAP, iKAP, and iKAP\_DOXoff colorectal cancer (CRC) in the bulk RNA sequencing data set. Blue and white indicate high and low expression, respectively. The red rectangle represents the iKAP group with high expression of pro- and anti-adipogenic cytokine genes.

*Figure 2B. GSEA of tumor stroma in mouse scRNA-seq comparing invasive iKAP versus non-invasive iAP and non-invasive iKAP\_DOXoff. NES, normalized enrichment score. FDR, false discovery rate.*

## 4.2 Results

To validate these proadipogenic cytokines regulated by *Kras*<sup>\*</sup>, we assessed their expression in primary 2-dimensional iKAP cancer cell cultures with *Kras*<sup>\*</sup> activation (+DOX) versus those with *KRAS*<sup>\*</sup> deactivation (-DOX). The results revealed that *KRAS*<sup>\*</sup> induced the upregulation of *Bmp4* and *Wnt5b* (Fig. 2C). *BMP4* is known to facilitate the conversion of pluripotent stem cells into adipocytes through the SMAD and p38MAPK pathways (Huang et al., 2009), while *WNT5B* plays a role in noncanonical WNT signaling by inhibiting  $\beta$ -catenin nuclear localization and indirectly promoting the adipogenesis of progenitor cells (Cristancho et al., 2011). The connection between *KRAS*<sup>\*</sup> and *WNT5B/BMP4* was confirmed in various models, including (i) two patient-derived xenograft organoids (PDXOs) engineered for inducible *KRAS* activation (Fig. 2D), (ii) the murine CRC cell line CMT93 with and without *KRAS*<sup>\*</sup>, (iii) iAP and iKAP tumor organoids, (iv) the human CRC cell line DLD1, which includes *KRAS*<sup>\*</sup>-expressing and *KRAS* wild-type cell lines, and (v) the human CRC data from the TCGA dataset, which includes *KRAS*<sup>\*</sup>-expressing and *KRAS* wild-type cases (Fig. 2E). Furthermore, immunohistochemical (IHC) staining confirmed elevated levels of *Bmp4* and *Wnt5b* in *Kras*<sup>\*</sup>-expressing iKAP tumors compared to iAP controls (Fig. 2F). *Wnt5b* and *Bmp4* expression levels exhibited a positive correlation with tumor stages in the iKAP model, but not in the iAP model (Fig. 2G), indicating the dependence of *Bmp/Wnt* signaling on *KRAS*<sup>\*</sup> and tumor stage in CRC development. This stage-dependency may be related to the subclonal nature of *KRAS* mutant cancer cells in early-stage disease (Banerjee et al., 2021) and changes in *KRAS*<sup>\*</sup> downstream signaling as tumors progress (Cellurale et al., 2011).

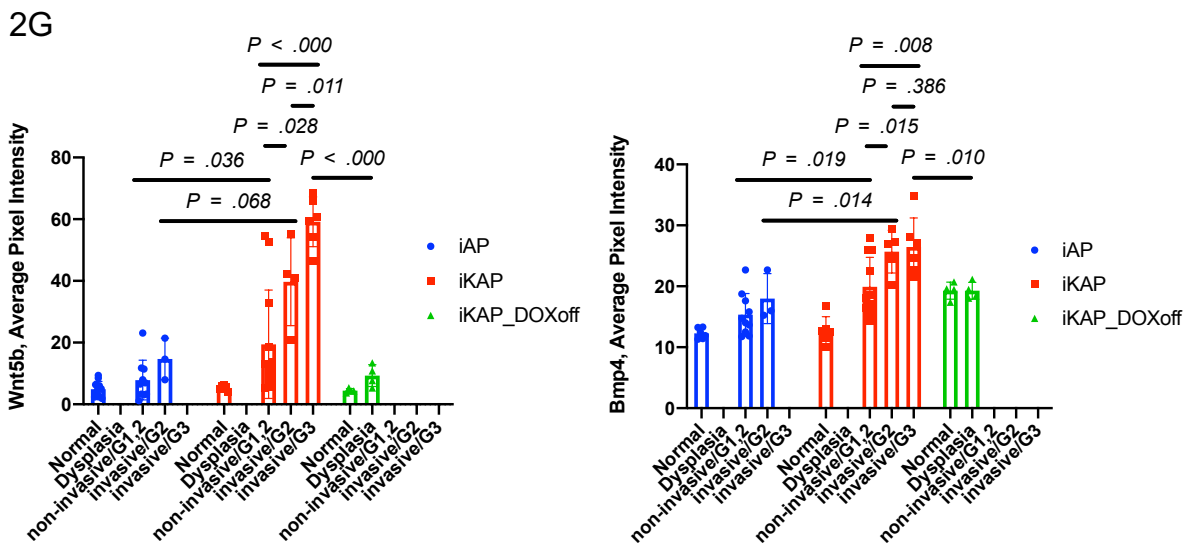
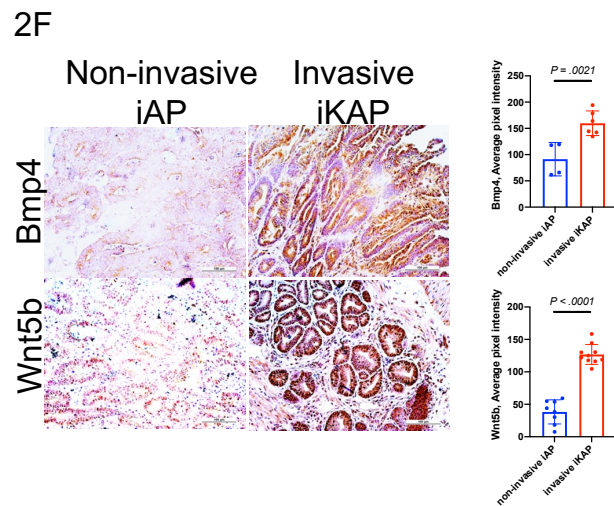
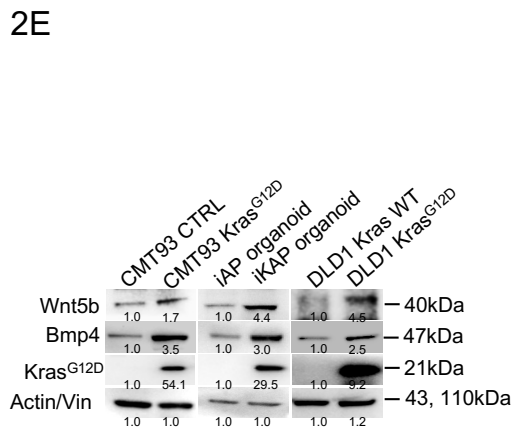
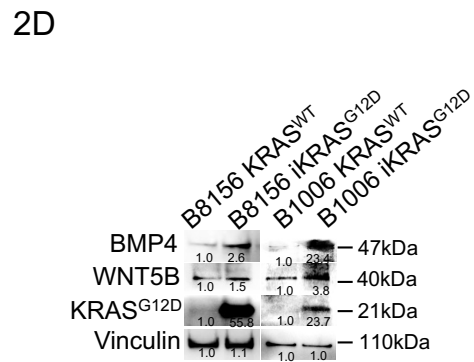
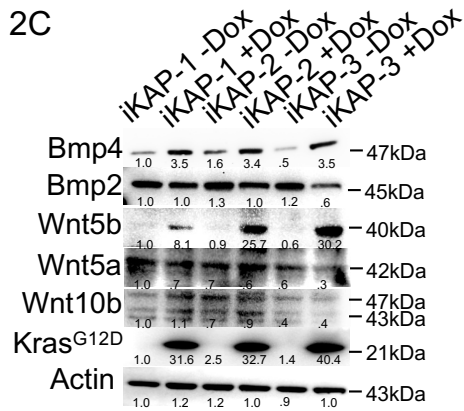


Figure 2C. Immunoblots of Bmp and Wnt family proteins in the cell lysates of iKAP cell lines with or without DOX supplementation to express Kras\*.

*Figure 2D. Immunoblots of BMP4 and WNT5B in the cell lysates of 2 PDXOs (B8156 and B1006) with or without DOX supplementation to induce KRAS<sup>G12D</sup> expression.*

*Figure 2E. Immunoblots of Wnt5B and Bmp4 in the cell lysates of CMT93 cells, iKAP/iAP organoids, and DLD1 cell lines.*

*Figure 2F. Immunohistochemical staining (left panel) and quantification (right panel) of Wnt5b and Bmp4 in non-invasive iAP and invasive iKAP tumors. Scale bar, 100  $\mu$ m;  $n \geq 4$  biological replicates. Data represent mean  $\pm$  SD. Student's *t* test.*

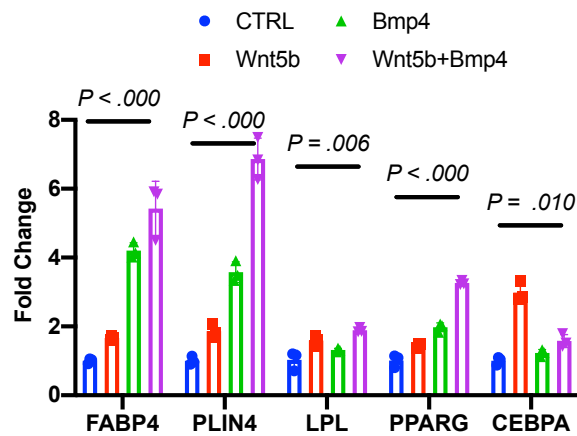
*Figure 2G. Quantification of Wnt5b and Bmp4 expression levels in high-, moderate- and low-grade invasive and non-invasive iKAP and iAP tumors (grade scored by GI pathologist; blinded).  $N \geq 3$  biological replicates. Data represent mean  $\pm$  SD. Student's *t* test.*

To validate the pro-adipogenic activity of KRAS\*-regulated BMP4 and WNT5B, we employed several model systems. Firstly, we used the 3T3L1 cell culture model of adipocyte differentiation (Reed et al., 1980), which confirmed that supplementation of insulin with recombinant Bmp4 and Wnt5b increased the expression of adipocyte markers and regulators compared to insulin-only controls (Fig. 2H). Secondly, when undifferentiated 3T3L1 cells were treated with conditioned medium (CM) from iKAP cells with KRAS\* activation (KRAS\*-on), but not from cells with KRAS\* deactivation (KRAS\*-off), it stimulated the differentiation of these cells into adipocyte progenitor cells and lipid-rich fibroblasts (Fig. 2I). These cells expressed the adipocyte marker Pparg and lipid-rich fibroblast markers such as Fgf10, Tcf21, and Plin4 (Fig. 2I, right). Thirdly, we used two patient-derived xenograft organoids engineered with a DOX-inducible KRAS\* allele and the human CRC DLD1 cell line, which isogenic for KRAS\* or wild-type KRAS. When human mesenchymal stem cells (hMSCs) were treated with KRAS\*-on CM, they showed enhanced differentiation into adipocyte-like cells expressing lipid-rich fibroblast genes compared to treatment with wild-type KRAS CM (Fig. 2J and 2K). Finally, we observed that lipo-fibrogenesis was specifically increased in the collagen-expressing tumor

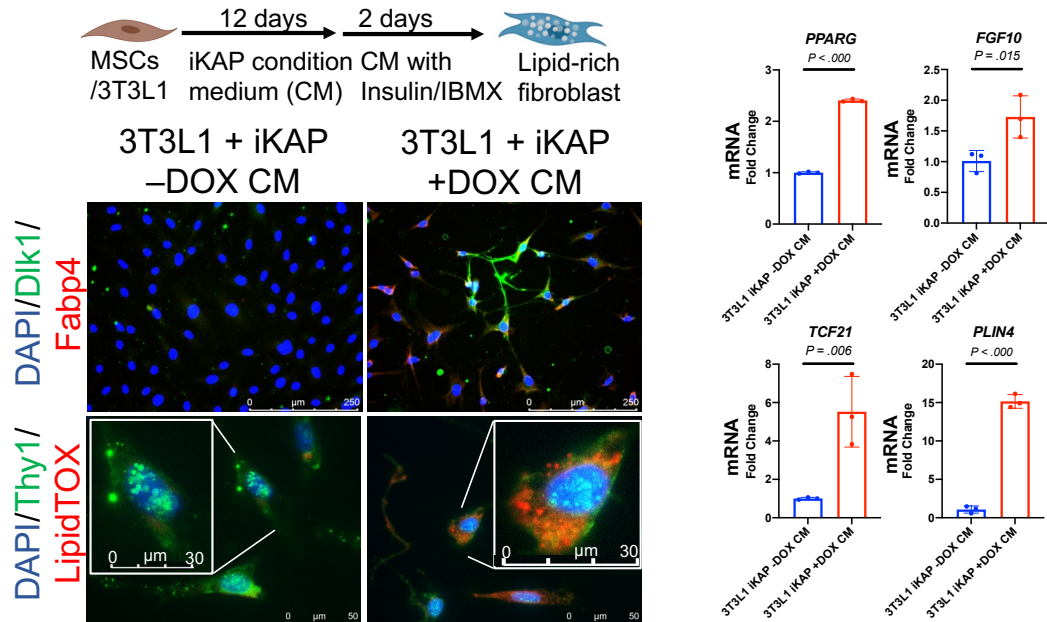


stroma of tumors generated by co-injecting 3T3L1 cells with *KRAS\**-on iKAP cancer cells. Conversely, lipo-fibrogenesis decreased in these tumors after one week of *KRAS\** inactivation due to doxycycline withdrawal (Fig. 2L). Additionally, we detected insulin pathway signaling in iKAP bulk tumors and *KRAS\**-driven tumor stroma (Fig. 2M), indicating the presence of an active adipogenesis process within the *KRAS\** stroma. Collectively, these findings support the notion that *KRAS\** induces the expression of the pro-adipogenic cytokines WNT5B and BMP4, promoting stromal lipo-fibrogenesis.

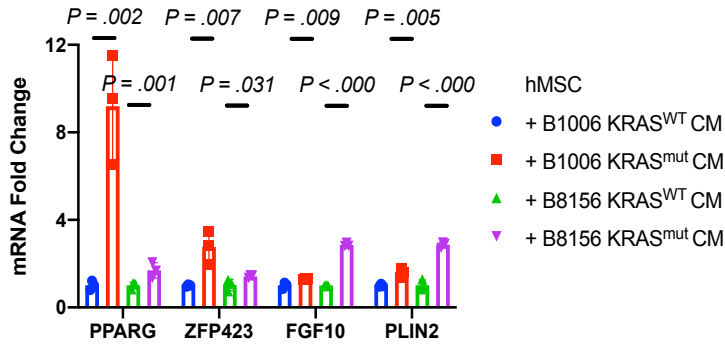
2H



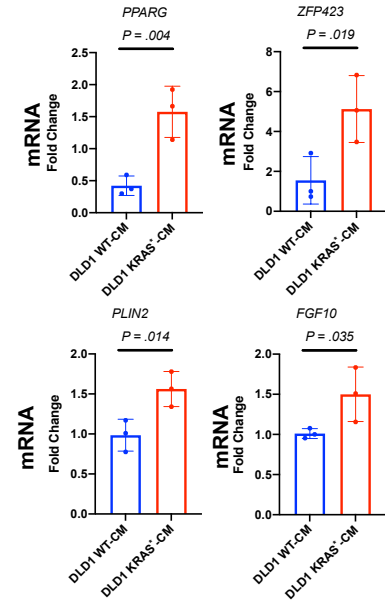
2I



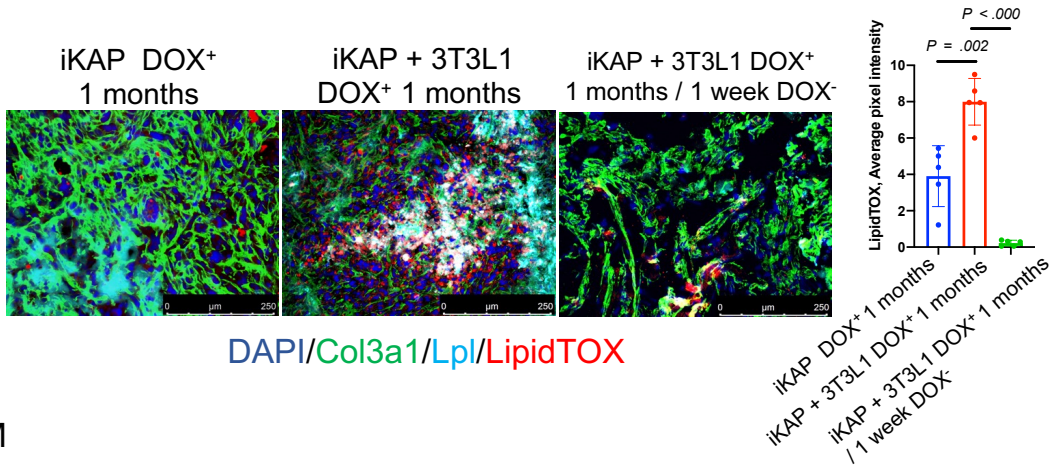
2J



2K



2L



2M

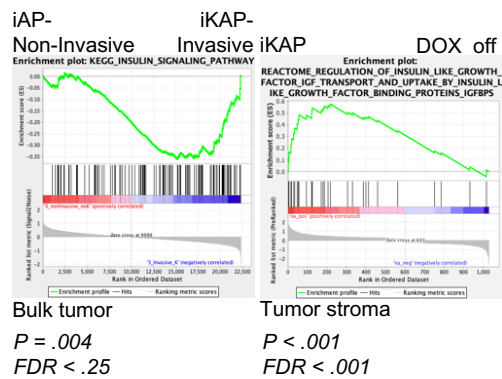


Figure 2H. RT-qPCR of adipogenic genes in 3T3L1 cells following supplementation with recombinant Bmp4 and/or Wnt5B. All experimental groups were supplemented with 10 µg/mL insulin after 2 weeks of Bmp4 and/or Wnt5b treatment. N = 3 biological replicates. Data represent mean ± SD. Student's t test.

Figure 2I. Schematic diagram of CM co-cultured experiments (upper panel) to demonstrate the impact of iKAP CM on lipid-rich fibroblast differentiation. (See Methods for cell culture details.) Immunofluorescence staining of lipid droplets, Thy1, and Dlk1 (lower panel) and quantification of lipid-rich CAF genes using quantitative reverse transcription polymerase chain reaction (RT-qPCR; right panel) in iKAP conditioned medium (CM)-educated 3T3L1 cells. Scale bar, 250 µm, 50 µm, and 30 µm; n = 3 biological replicates. IBMX, 3-isobutyl-1-methylxanthine; MSCs, mesenchymal stem cells. Data represent mean ± SD. Student's t test.

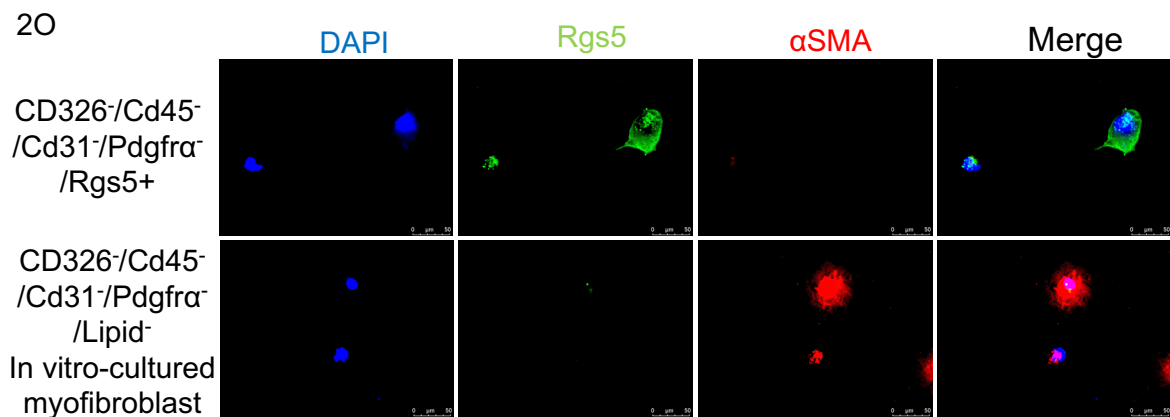
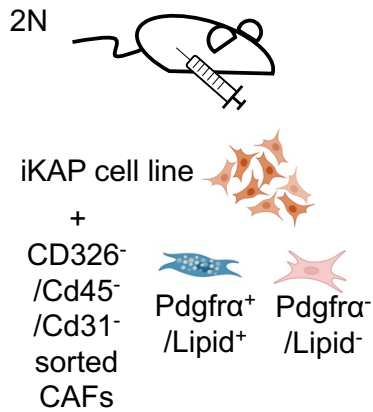
Figure 2J. RT-qPCR quantification of lipid-rich CAF genes in PDXO Kras\* CM-educated hMSCs. N = 3 biological replicates. Data represent mean ± SD. Student's t test.

Figure 2K. RT-qPCR quantification of lipid-rich CAF genes in DLD1 Kras\* CM-educated hMSCs. N = 3 biological replicates. Data represent mean ± SD. Student's t test.

Figure 2L. Immunofluorescence analysis of lipid droplets, Col3a1, and Lpl in subcutaneous iKAP tumors and tumors generated by co-injecting iKAP cell lines and 3T3L1 into nude mice. Scale bar, 250 µm. Quantification of LipidTOX intensity (right panel). N = 5 biological replicates. Data represent mean ± SD. Student's t test.

Figure 2M. Enrichment plots of insulin pathways in non-invasive iAP versus invasive iKAP bulk mRNA-seq dataset and in invasive iKAP versus non-invasive iKAP DOXoff in mouse stroma scRNA-seq dataset (lower panel). N ≥ 4 and N = 3 biological replicates FDR, false discovery rate.

These findings prompted an investigation into the potential biological consequences of lipid-rich versus lipid-sparse CAFs on tumors. To this end, we isolated primary lipid-rich and lipid-sparse CAFs from iKAP tumors by flow sorting LipidTOX<sup>+</sup>/Pdgfra<sup>+</sup>/Cd326<sup>-</sup>/Cd45<sup>-</sup>/Cd31<sup>-</sup> and LipidTOX<sup>-</sup>/Pdgfra<sup>-</sup>/Cd326<sup>-</sup>/Cd45<sup>-</sup>/Cd31<sup>-</sup> cell populations for use in co-injection studies (Fig. 2N). The small population of lipid-sparse CAFs required brief in vitro expansion (See Methods “Lipid-sparse CAFs/myofibroblasts isolation”) and were subsequently validated for the expression of αSma and Rgs5 to confirm the CAF myofibroblastic cell type (Fig. 2O).



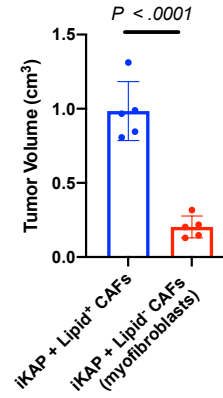
*Figure 2N. Schematic diagram of orthotopic co-injection experiments in mice. See Methods “Flow cytometry and sorting” for details.*

*Figure 2O. Immunofluorescence staining of RGS5 and  $\alpha$ SMA in Cd326-/Cd45-/Cd31-/Pdgfra-/Rgs5+ sorted cells and in Cd326-/Cd45-/Cd31-/P $\alpha$ -/Lipid- in vitro-cultured myofibroblasts. N = 4 biological replicates.*

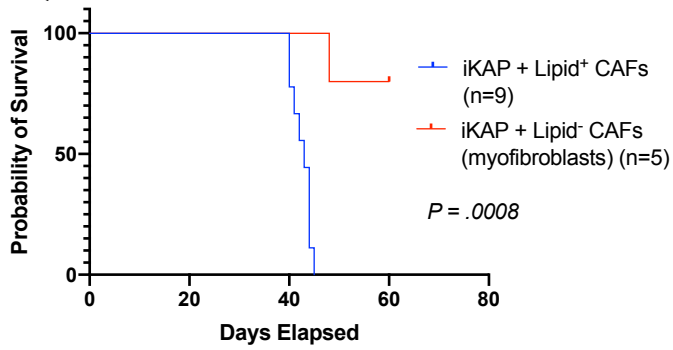
Orthotopic co-injection of iKAP cancer cells and sorted lipid-rich CAFs generated larger tumors (Fig. 2P) and reduced overall survival (Fig. 2Q). Immunofluorescence analysis of these tumors confirmed abundant lipid droplets in the tumor stroma (Fig. 2R). In contrast, orthotopic co-injection of iKAP cancer cells and lipid-sparse CAFs (myofibroblastic CAFs) generated tumors that grew more slowly and were associated with prolonged survival. Immunofluorescence analysis revealed a paucity of lipid droplets in the tumor stroma and a more prominent representation of  $\alpha$ Sma+ cells (Fig. 2P-R). These findings are consistent with the single-cell data obtained from primary tumors, which showed that  $\alpha$ Sma+ CAFs are distinct from lipid-rich CAF subpopulations (Fig. 1G and 1I). Moreover, human CRC (TCGA) analyses supported these observations and established a positive correlation between advanced disease and increased lipid-rich CAF gene signatures (Supplementary Table S1: the combination of the top 10 differentially expressed genes in the 4  $\alpha$ Sma- CAF subgroups from mouse scRNA-seq; Supplementary Table S2: the combination of adipocyte and fibroblast genes from PanglaoDB), along with a worse prognosis (Fig. 2S and 2T). It's worth noting that myofibroblast gene signature (GSEA) and myofibroblast differentiation gene signature (GSEA) scores had no impact on CRC prognosis (Fig. 2U). These results collectively suggest that lipid-rich CAFs promote the progression of both mouse and human CRC.

2P

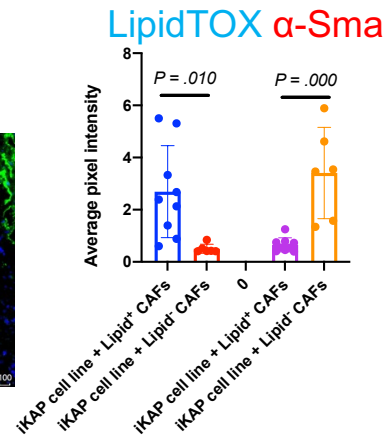
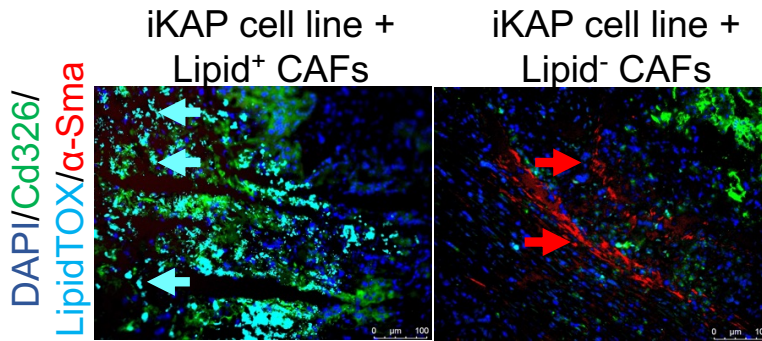
iKAP +  
Lipid<sup>+</sup> CAFs  
  
iKAP +  
Lipid<sup>-</sup> CAFs  
(myofibroblasts)



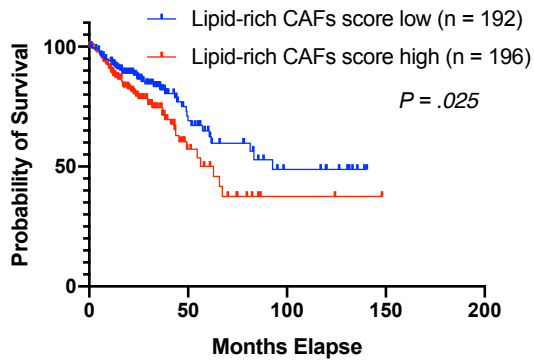
2Q



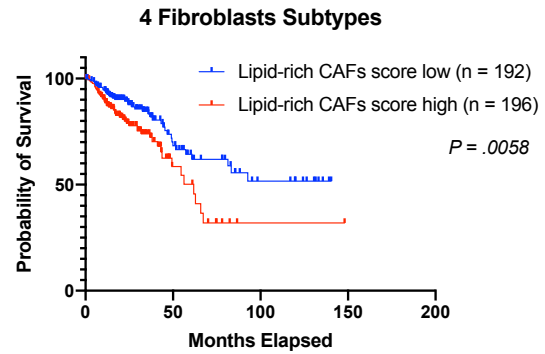
2R



2S



2T



2U

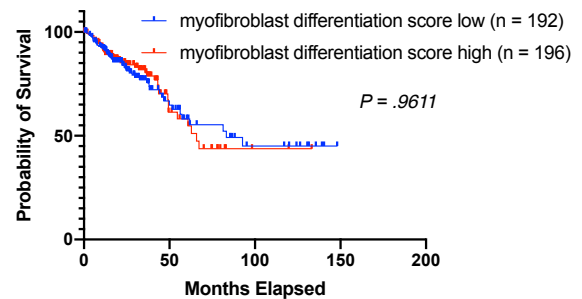
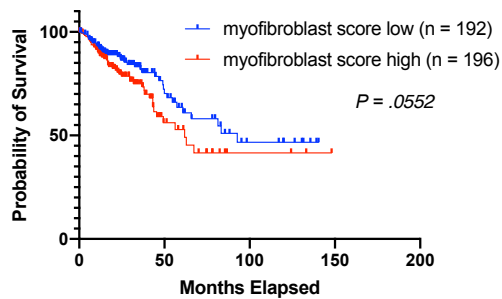


Figure 2P. Tumors generated by orthotopic co-injection in cecum of lipid-rich CAFs or lipid-sparse CAFs (myofibroblasts) with iKAP cell line (left panel) at 4 weeks. Quantification of tumor size (right panel).  $N = 5$  biological replicates. Data represent mean  $\pm$  SD. Student's  $t$  test.

Figure 2Q. Orthotopic co-injection of lipid-rich CAFs and the iKAP cell line decreases overall survival in mice.  $N \geq 5$  biological replicates. Log-rank (Mantel-Cox) test.

Figure 2R. Immunofluorescence staining of lipid droplets,  $\alpha$ Sma, and Cd326 in co-injection tumors. Quantification of LipidTOX and  $\alpha$ Sma (right panel).  $N \geq 5$  biological replicates. Data represent mean  $\pm$  SD. Student's  $t$  test.

Figure 2S. Survival of colorectal cancer patients with high vs. low gene set variation analysis scores for lipid-rich CAF gene signatures (data from The Cancer Genome Atlas- Colon adenocarcinoma). See Supplementary Table S2 for Lipid-rich CAF gene signatures. The median lipid-rich CAF GSVA score was used as cut-off to define high and low groups. Log-rank (Mantel-Cox) test.

Figure 2T. Kaplan-Meier survival curves of TCGA-COAD data comparing high vs. low signature score of differentially expressed genes from 4 CAF subtypes in single-cell RNA sequencing analyses. The median of the 4 CAF GSVA score was used as cut-off to define high and low groups. Log-rank (Mantel-Cox) test.

Figure 2U. Kaplan-Meier survival curves of TCGA-COAD data comparing high vs. low signature score of myofibroblast (GSEA) and myofibroblast differentiation (GSEA). The median of the myofibroblast and myofibroblast differentiation GSVA scores were used as cut-off to define high and low groups. Log-rank (Mantel-Cox) test.



**CHAPTER 5:**  
**KRAS\* REGULATES PRO-ADIPOGENESIS CYTOKINES**  
**THROUGH TFCP2**

## CHAPTER 5: KRAS\* REGULATES PRO-ADIPOGENESIS CYTOKINES THROUGH TFCP2

Content of this chapter is partly based on the following manuscript:

Hsu, W.H., LaBella, K. A., Lin, Y., Xu, P., Lee R., Hsieh, C.E., Yang, L., Zhou, A., Blecher, J. M., Wu, C. J., Lin, K., Shang, X., Jiang, S., Spring, D. J., Xia, Y., Chen, P., Shen, J. P., Kopetz, S., DePinho, R. A. (2023) "Oncogenic KRAS drives lipo-fibrogenesis to promote angiogenesis and colon cancer progression" *Cancer Discov*, 10.1158/2159-8290.CD-22-1467

### 5.1 Preliminary research and rationale

To elucidate the mechanisms by which KRAS\* stimulates the expression of pro-adipogenic cytokines, we conducted an analysis encompassing transcription factor expression (Muzny et al., 2012), transcription factor (TF) signatures, and consensus TF binding motifs within the promoters of proadipogenic cytokine genes that exhibited KRAS\*-dependent expression in both murine and human CRC (Supplementary Table S3). This comprehensive examination revealed two potential TF candidates: sex-determining region Y (*SRY*, also known as testis-determining factor), responsible for male sex determination (Fechner et al., 1996), and alpha-globin *TFCP2* (Fig. 3A). Subsequently, we chose to focus on *TFCP2* due to its ranking as the top candidate and the knowledge that ERK1, a downstream effector of KRAS, is recognized to phosphorylate *TFCP2*, thereby enhancing its DNA binding activity (Volker et al., 1997). *SRY*, on the other hand, was deprioritized due to its exclusive expression in males on the Y chromosome, despite our data revealing that KRAS\* stimulates the expression of pro-adipogenic cytokine genes in both sexes.

3A

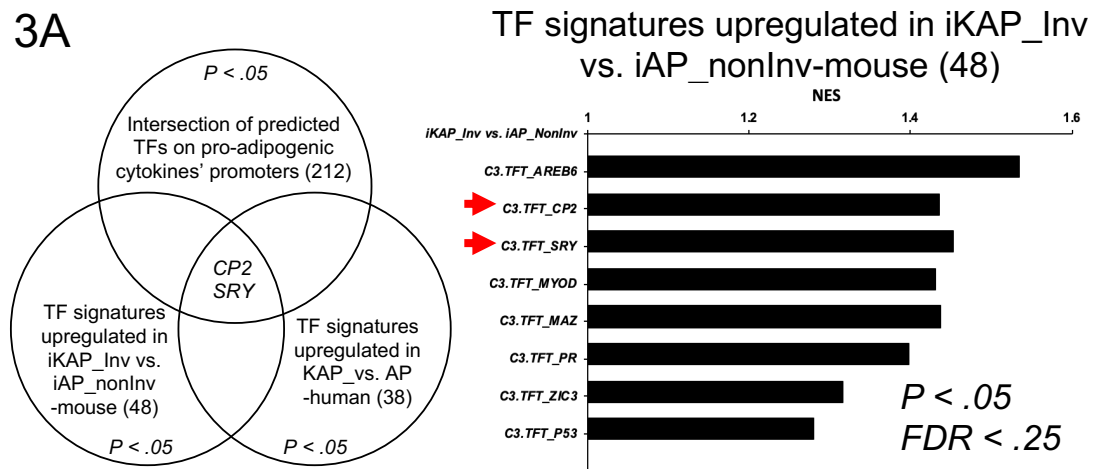


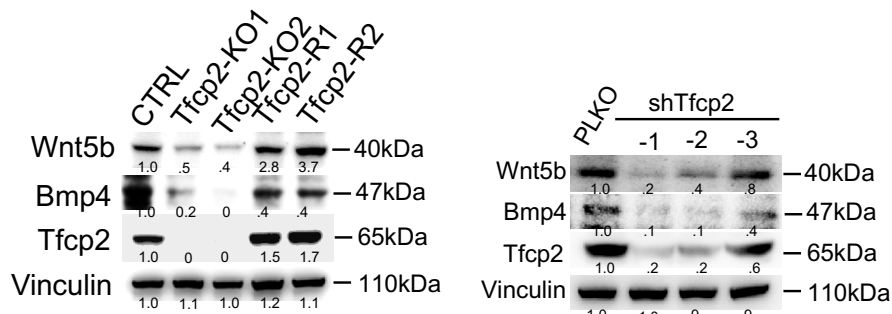
Figure 3A. Venn diagram of the putative transcription factors (TFs) that bind to the consensus motifs on promoters of pro-adipogenic cytokines as well as candidates from GSEA of TF signatures enriched in KRAS\* tumors (left panel). The gene lists of these 3 datasets are provided in Supplementary Table S3. The TF signatures enriched in Kras\* tumors in a genetically engineered mouse (GEM) model (right panel). CP2, TFCP2; FDR, false discovery rate.

## 5.2 Results

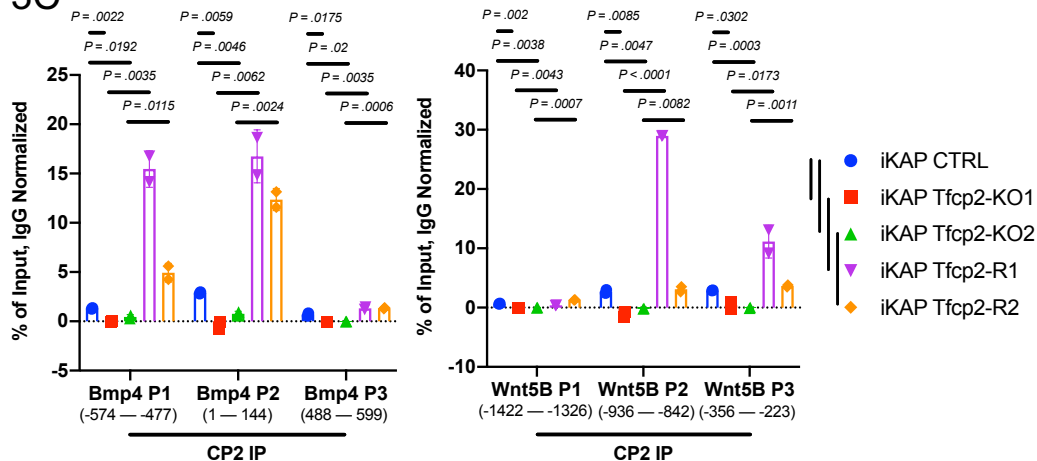
To validate the role of TFCP2 in mediating KRAS\*-driven expression of pro-adipogenic cytokine genes, we employed two approaches: Tfc2 depletion using short hairpin RNA (shRNA) and Tfc2 deletion through clustered regularly interspaced short palindromic repeats (CRISPR) technology in iKAP cell lines. As part of the experimental design, we also generated Tfc2-null clones that were subsequently rescued by the reintroduction of wild-type Tfc2. In cell lines where Tfc2 was depleted or deleted, the expression of Wnt5b and Bmp4 was reduced in Kras\*-expressing cells, while the Tfc2-rescued null controls exhibited restored

expression (Fig. 3B). Further validation was achieved through chromatin immunoprecipitation (ChIP) assays using anti-Tfcp2 antibodies, which confirmed the direct binding of Tfcp2 to its consensus binding motifs within the promoters of Wnt5b and Bmp4 (Fig. 3C). In addition, reporter gene expression assays for Wnt5b and Bmp4 showed reduced expression in *Kras*\*-expressing cells with Tfcp2 depletion, which was subsequently restored upon Tfcp2 re-expression, providing additional evidence of Tfcp2's direct binding to the promoters (Fig. 3D). TFCP2's role in regulating the biology of CAFs and other components of the tumor microenvironment was underscored by a robust positive correlation between TFCP2-high gene signature scores and various stromal lineages, including endothelial cells, fibroblasts, and adipocyte signatures (Franzen et al., 2019) (Fig. 3E).

### 3B



### 3C



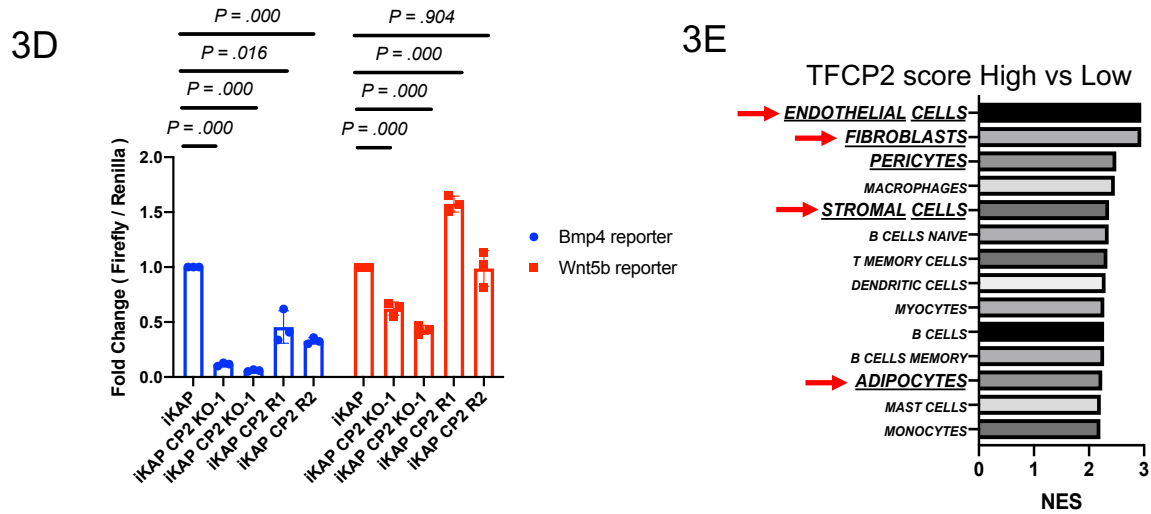


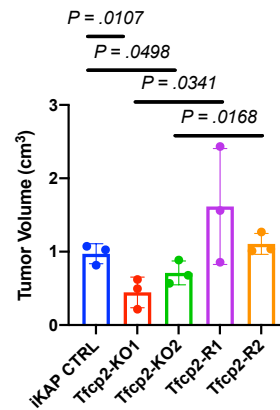
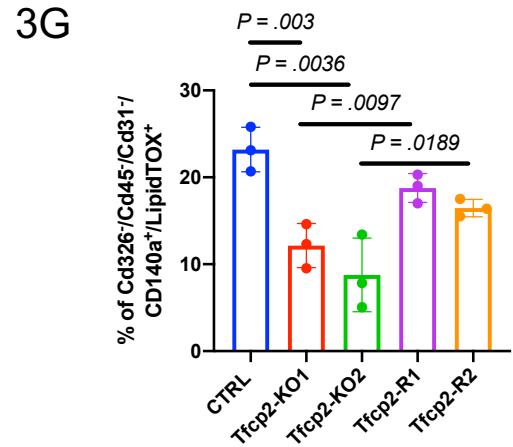
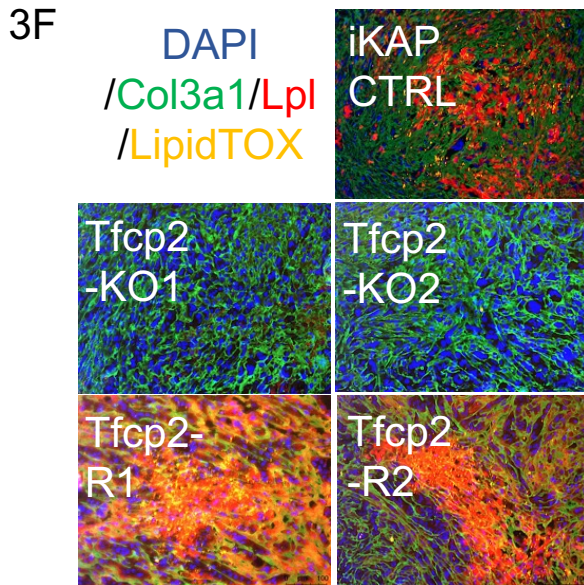
Figure 3B. Immunoblots of pro-adipogenic cytokines BMP4 and WNT5B, and TFCP2 in TFCP2-knockout and rescued iKAP cell lines (left panel). Immunoblots of WNT5B, BMP4 and TFCP2 in cell lysates of TFCP2-knockout and rescued iKAP cell lines. PLKO, vector control (right panel).

Figure 3C. Chromatin immunoprecipitation-quantitative polymerase chain reaction (ChIP-qPCR) analysis of WNT5B and BMP4 promoter sequences on the TFCP2 binding elements. N = 3 biological replicates. Data represent mean ± SD. Student's t test.

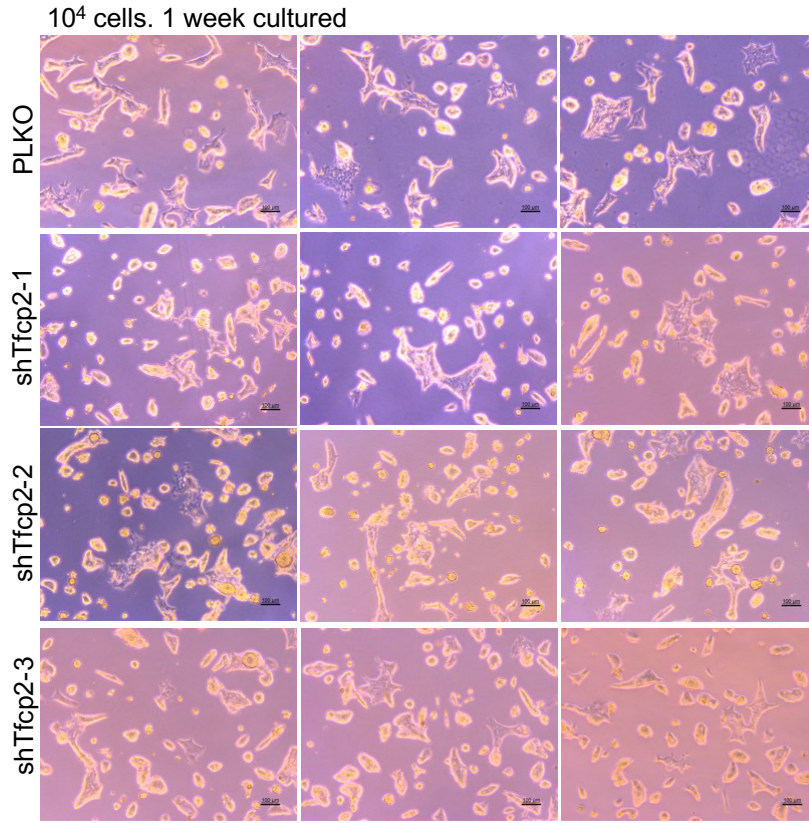
Figure 3D. Luciferase (Luc) reporter assays show that TFCP2 knockout reduces the transcriptional activity of BMP4 and WNT5B, which can be rescued by re-expression of TFCP2. N = 3 biological replicates. Data represent mean ± SD. Student's t test

Figure 3E. Cell type correlations in high TFCP2-regulated gene signature (GSEA, C3 TFT) gene set variation analysis (GSVA) scores of TCGA-COAD patient cohort. NES, normalized enrichment score.

Functionally, when iKAP cancer cells with Tfc2 depletion were syngeneically or xenograft-injected, they generated smaller tumors with fewer lipid-rich CAFs, in contrast to the Tfc2-rescued null controls where lipid-rich CAFs were abundant (Fig. 3F-H). Importantly, Tfc2 depletion did not significantly affect cancer cell proliferation in vitro (Fig. 3I-J), suggesting that its primary effects are exerted within the tumor microenvironment.



3I



3J

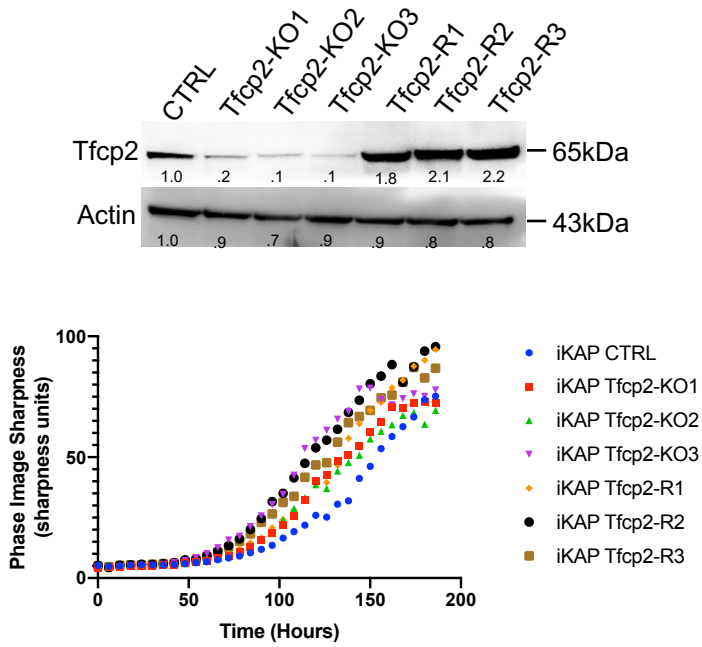


Figure 3F. Immunofluorescence staining of lipid droplets, LPL, and COL3a1 in TFCP2–knockout and rescued tumors. Scale bar, 100  $\mu$ m; n = 5 biological replicates.

Figure 3G. Percentages of CD326–/CD45–/CD31–/CD140a+/LipidTOX+ –sorted cells in TFCP2–knockout and rescued tumors from Fig. 4E. N = 3 biological replicates. Data represent mean  $\pm$  SD. Student's t test.

Figure 3H. Tumors generated by xenograft implantation of TFCP2–knockout and rescued iKAP cell lines into nude mice in 1 month (left panel). Quantification of tumor burdens (right panel). N = 3 biological replicates. Data represent mean  $\pm$  SD. Student's t test.

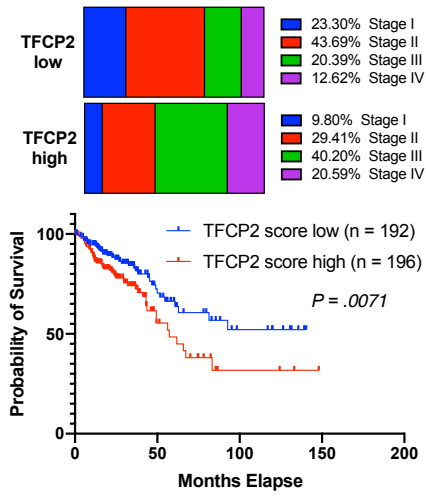
Figure 3I. Phase contrast images of TFCP2–knockdown iKAP cell lines in vitro after 1 week of culture. PLKO, vector control.

Figure 3J. Immunoblots of TFCP2 in the cell lysates of TFCP2–knockout and rescued iKAP cell lines (upper panel). The proliferation of TFCP2–knockout and rescued iKAP cell lines as determined using IncuCyte® Cell Count Proliferation Assay (lower panel).

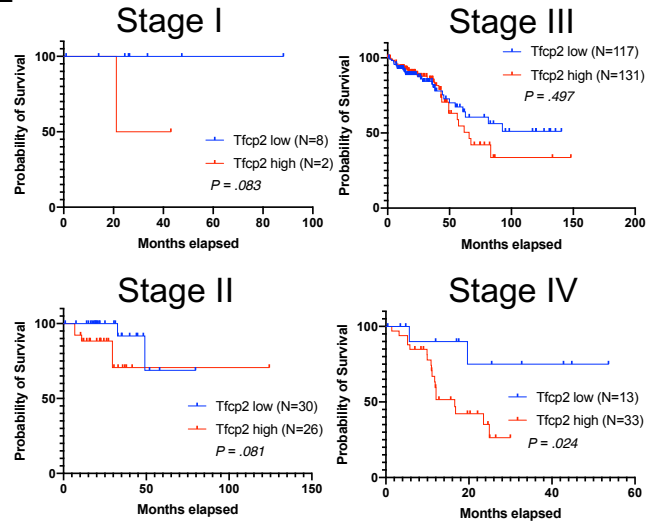
High TFCP2 gene signature scores correlated positively with advanced invasive and metastatic disease and poor survival in CRC patients (Fig. 3K-L). This discovery led us to investigate the therapeutic potential of the TFCP2-specific small molecule inhibitor FQI1, which targets the TFCP2 DNA binding domain and eliminates downstream transcriptional activity (Grant et al., 2012). Initially, we confirmed that FQI1 downregulated the canonical TFCP2-regulated genes *SPP1*, *MMP9*, and *CFH* (Santhekadur et al., 2012) in cultured iKAP cells treated with FQI1 (Fig. 3M). Subsequently, we demonstrated that FQI1 treatment of iKAP tumor cell lines reduced the expression of *Wnt5b* and *BMP4* (Fig. 3N). Furthermore, in tumor-bearing iKAP mice, FQI1 treatment reduced the accumulation of lipid-rich CAFs and extended survival (Fig. 3O-P). These findings provide compelling evidence that KRAS\*–dependent CRC progression is, in part, driven by the stimulation of lipo-fibrogenesis through TFCP2-mediated regulation of proadipogenic cytokines.



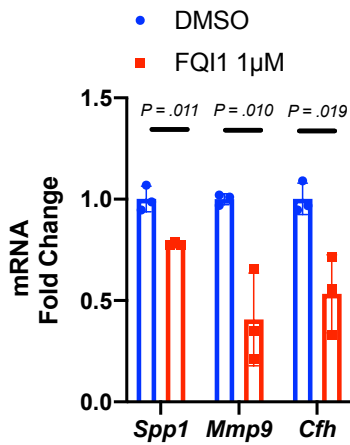
3K



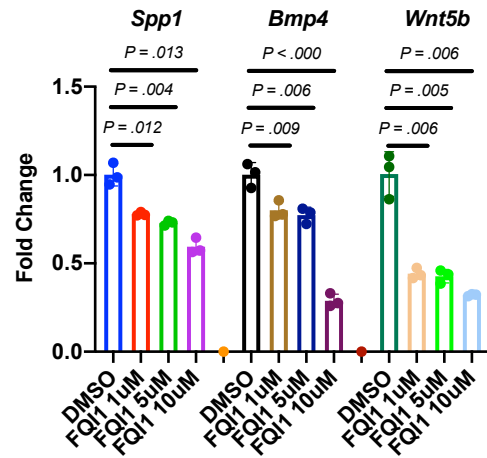
3L



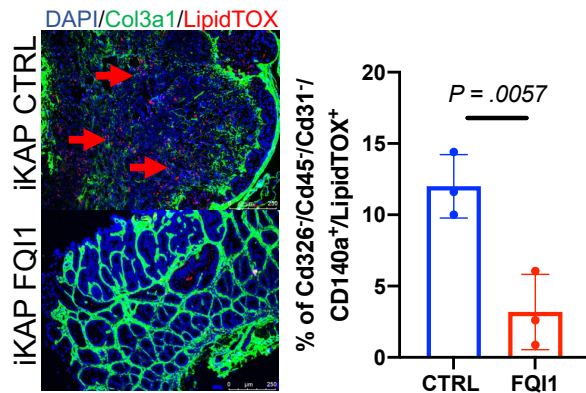
3M



3N



3O



3P

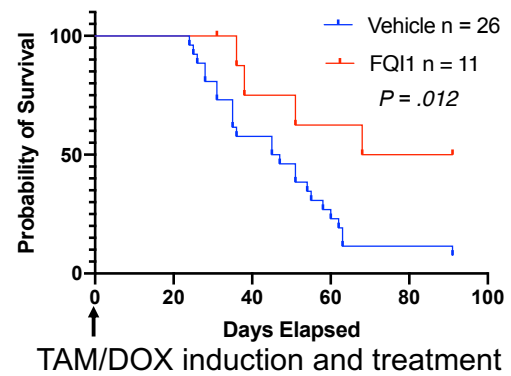


Figure 3K. TCGA–COAD tumor stages and survival in high vs. low GSVA scores of TFCP2–regulated gene signatures. The median TFCP2 GSVA score was used as cut-off to define high and low groups. Chi-square test for tumor stages and Log–rank (Mantel–Cox) test for survival analyses.

Figure 3L. Survival analyses comparing high vs. low GSVA scores of TFCP2–regulated gene signatures in different stage tumor in TCGA–COAD. The median TFCP2 GSVA score was used as cut-off to define high and low groups. Log–rank (Mantel–Cox) test.

Figure 3M. RT–qPCR validation of Tfc2 downstream genes following FQ11 treatment of iKAP cell lines. N = 3 biological replicates. Data represent mean  $\pm$  SD. Student's t test.

Figure 3N. RT–qPCR validation of pro–adipogenic cytokine genes in FQ11–treated iKAP cell lines in vitro. N = 3 biological replicates. Data represent mean  $\pm$  SD. Student's t test.

Figure 3O. Immunofluorescence staining of lipid droplets and Col3a1 (left panel) and percentages of Cd326–/Cd45–/Cd31–/Cd140a+/LipidTOX+ –sorted cells in FQ11–treated iKAP tumors (right panel). Scale bar, 250  $\mu$ m; N = 3 biological replicates. Data represent mean  $\pm$  SD. Student's t test.

Figure 3P. Kaplan–Meier survival curves of iKAP mice treated with FQ11 or vehicle. TAM, tamoxifen. Log–rank (Mantel–Cox) test.

**CHAPTER 6:**  
**LIPID-RICH CAFs SECRETE VEGFA**  
**TO PROMOTE TUMOR ANGIOGENESIS**

## **CHAPTER 6: LIPID-RICH CAFs SECRETE VEGFA TO PROMOTE TUMOR ANGIOGENESIS**

Content of this chapter is partly based on the following manuscript:

Hsu, W.H., LaBella, K. A., Lin, Y., Xu, P., Lee R., Hsieh, C.E., Yang, L., Zhou, A., Blecher, J. M., Wu, C. J., Lin, K., Shang, X., Jiang, S., Spring, D. J., Xia, Y., Chen, P., Shen, J. P., Kopetz, S., DePinho, R. A. (2023) "Oncogenic KRAS drives lipo-fibrogenesis to promote angiogenesis and colon cancer progression" *Cancer Discov*, 10.1158/2159-8290.CD-22-1467

### **6.1 Preliminary research and rationale**

Certain cells containing lipid droplets, whether they are cancer cells themselves or myeloid cells within the tumor microenvironment, have previously been demonstrated to enhance the invasiveness of colorectal cancer. However, the specific role of the subgroup of lipid-rich fibroblasts in this process remains unclear. Although single-cell sequencing analysis has identified the presence of lipofibroblasts in human colorectal cancer, no comprehensive study has investigated the development of stromal lipo-fibrogenesis driven by KRAS\* or the function of KRAS\*-driven cancer lipid-rich fibroblasts. In order to gain deeper insights into the biological functions of lipid-rich CAFs within KRAS\*-expressing CRC, we conducted an analysis of both murine and human CRC transcriptomic profiles to identify pathways and cell types that are enriched in tumors exhibiting high scores for the lipid-rich CAF gene signature. The top pathways identified included ANGIOGENESIS and KRAS\_SIGNALING\_UP. According to the cell type gene signature database Panglao DB, the cell types most associated with high lipid-rich CAF signature scores were fibroblasts, adipocytes, and endothelial cells (Fig. 4A-B). Notably, a heatmap analysis indicated an enrichment of the endothelial cell signature in both

lipid-rich CAFs and KRAS\*-driven invasive CRC tumors (Fig. 4C). Based on these computational findings, we formulated a hypothesis that a key function of lipid-rich CAFs may involve promoting angiogenesis within the tumor microenvironment.

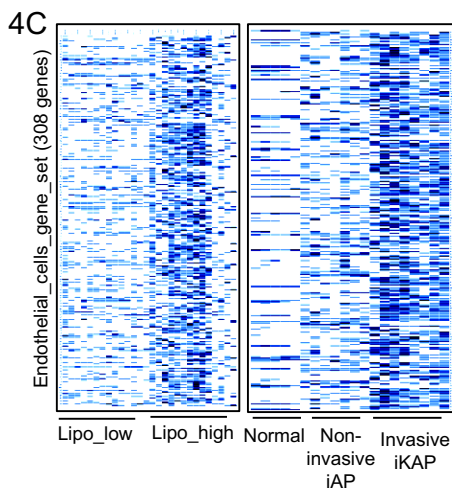
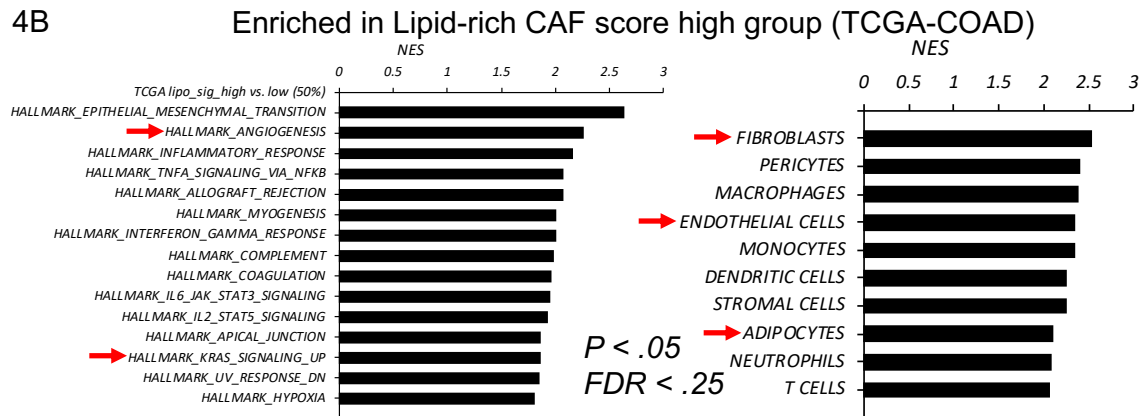
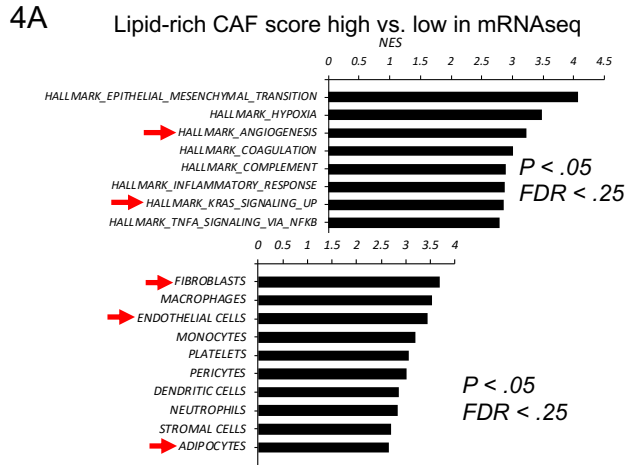


*Figure 4A. Transcriptomic profiling of high vs. low gene set variation analysis (GSVA) scores of lipid-rich CAF gene signatures in mouse bulk RNA sequencing dataset. Upper panel shows the enriched hallmark pathways and lower panel shows the correlated cell types in KRAS\* tumors as determined by GSEA. FDR, false discovery rate.*

*Figure 4B. GSEA (using the same cohort as in Fig. 3F) of high vs. low GSVA scores of lipid-rich CAF gene signatures in TCGA-COAD (left panel) and cell type correlations (lower panel). NES, normalized enrichment score. FDR, false discovery rate.*

*Figure 4C. Heatmap representation the expression of the endothelial cell gene set in high vs. low lipid-rich CAF GSVA scores in mouse bulk tumor RNA sequencing dataset (left panel). Expression of the endothelial cell gene set in non-invasive iAP vs invasive iKAP bulk tumor RNA sequencing dataset (right panel). Blue and white indicate high and low expression, respectively.*

## **6.2 Results**

To pinpoint the factors potentially driving tumor angiogenesis within lipid-rich CAFs, we conducted an analysis that integrated multiple datasets and carried out functional experiments using 3T3L1 cells educated with conditioned medium (CM) from iKAP cells and human mesenchymal stem cells (hMSCs) educated with CM from KRAS\*-expressing DLD1 cells. Firstly, employing adipokine array profiling, we identified several secreted factors known for their significant roles in tumor angiogenesis, including VegfA, macrophage colony-stimulating factor, hepatocyte growth factor, lipocalin 2, pentraxin 3 (Ptx3), and Dlk1 (a non-canonical Notch signaling ligand), to be upregulated in 3T3L1 cells educated with iKAP CM (Fig. 4D). Secondly, a scRNA-seq analysis of tumor tissues confirmed increased expression of Vegfa, pentraxin 3, and hepatocyte growth factor in the stroma of KRAS\*-expressing iKAP tumors

compared to iAP and KRAS<sup>\*</sup>-off (DOX-off) iKAP tumor controls (Fig. 4E-F). Correspondingly, reverse transcription polymerase chain reaction (RT-PCR) confirmed a significant and consistent increase in VEGFA expression in hMSCs educated with CM from DLD1 cells (Fig. 4G).

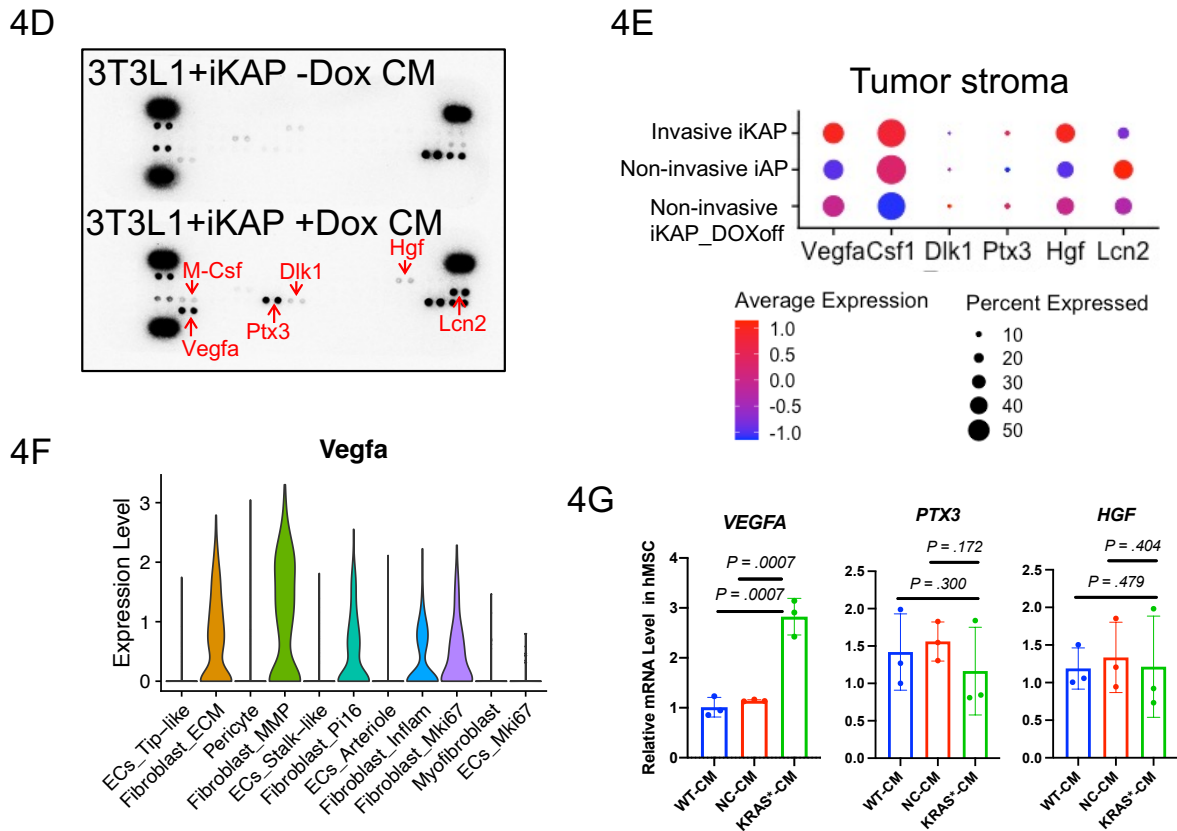


Figure 4D. Adipokine array of cell lysates from *Kras*<sup>\*</sup>(+DOX)- and *Kras*<sup>wt</sup>(-DOX)- conditioned medium (CM)-educated embryonic fibroblasts (3T3L1).

Figure 4E. Adipokine candidate gene expression in the stroma of iKAP, iAP, and iKAP\_DOX-off tumors using scRNA-seq. The average expression color scale was from 1 to -1. The dot size represents the proportion of expressing cells in each group. N = 3 biological replicates.

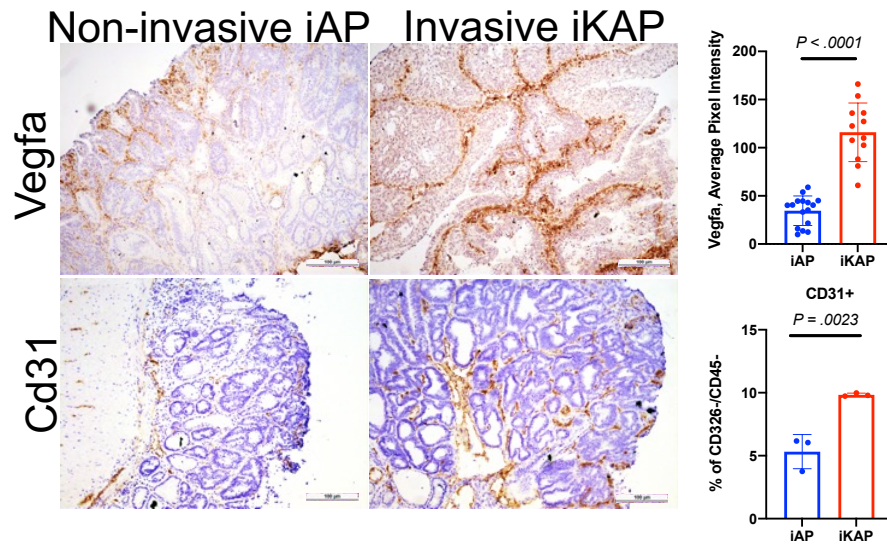
*Figure 4F. Vegfa expression levels in CAF subgroups in the combination of non-invasive iAP and invasive iKAP scRNA-seq data.*

*Figure 4G. RT-qPCR validation of targeted adipokines, VEGFA, PTX3 and HGF, in DLD1 KRAS<sup>G12D</sup> CM-educated hMSCs. N = 3 biological replicates. Data represent mean ± SD. Student's t test.*

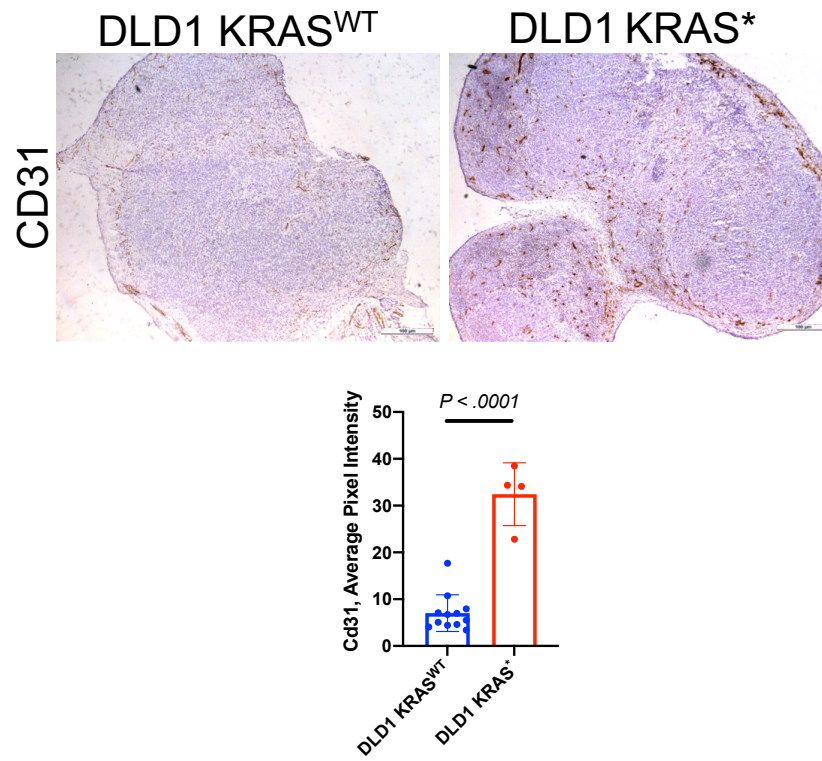
Thirdly, immunohistochemistry (IHC) and cytometry analysis confirmed the enrichment of Vegfa expression and the population of endothelial cells (CD326-/CD45-/CD31+) in both KRAS\*-expressing iKAP and KRAS\*-expressing DLD1 tumors (Fig. 4H-I). The positive correlation observed between lipid-rich CAFs and VEGFA expression, as well as endothelial cell counts in iKAP tumors, was in line with our immunofluorescence analysis, revealing an increase in Vegfa and the number of Cd31+ endothelial cells in iKAP tumors and tumors generated by co-injection of iKAP cancer cells and LipidTOX+ sorted cells (Fig. 4J). Finally, on a functional level, we evaluated the proangiogenic activity of lipid-rich CAFs using human umbilical vein endothelial cell (HUVEC) tube formation assays. The addition of CM from DLD1-KRAS<sup>G12D</sup> educated hMSCs resulted in a significant increase in various standard endothelial cell metrics, such as the covered area, total tube length, total number of branching points, and total number of loops within the endothelial structure (Fig. 4K). Hence, lipid-rich CAFs promote tumor angiogenesis through the secretion of VEGFA.



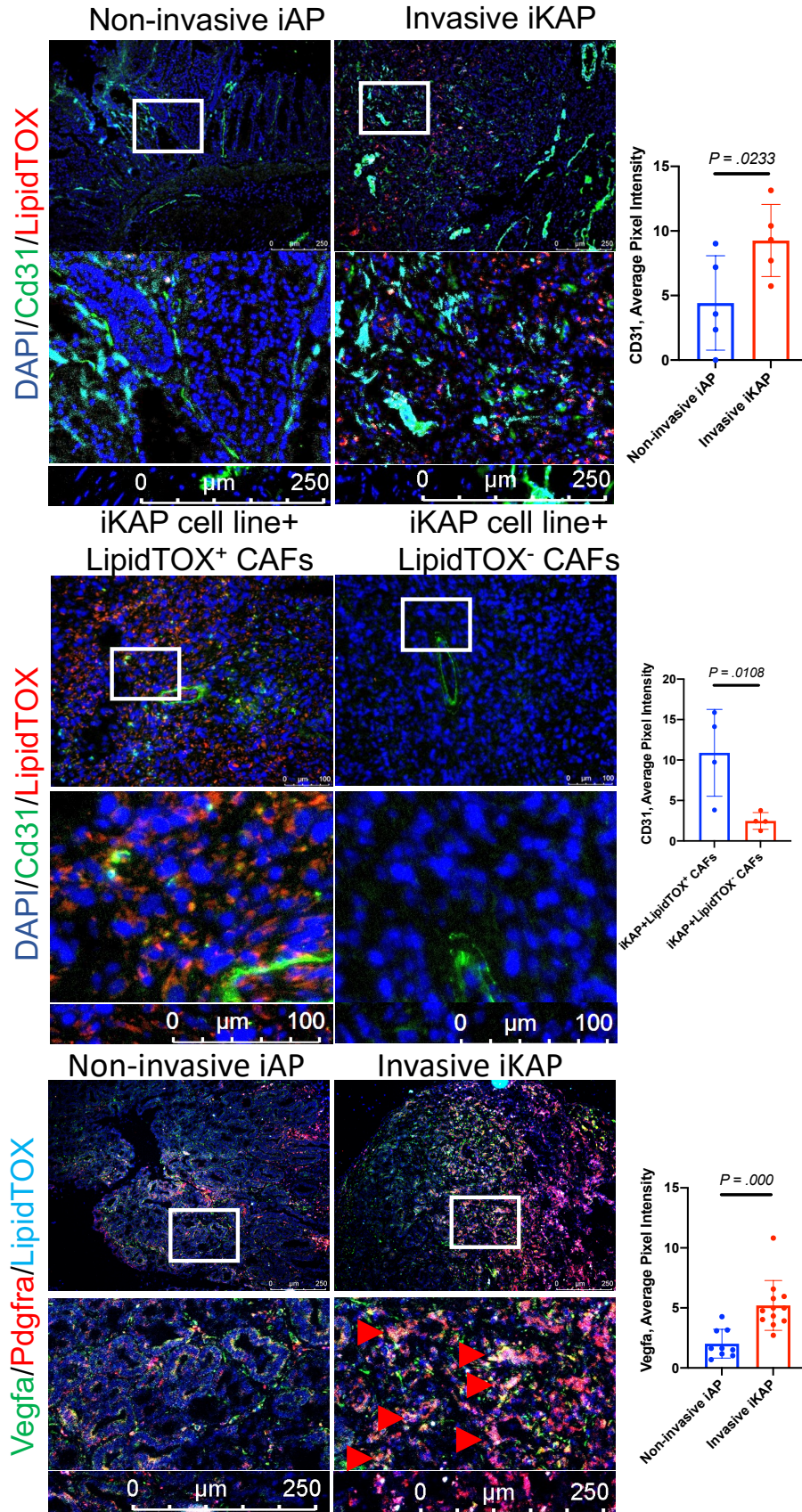
4H



4I



4J



4K

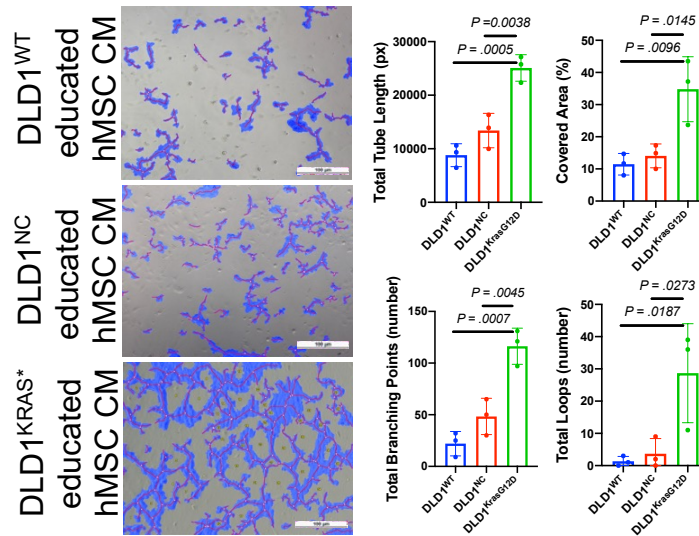


Figure 4H. Immunohistochemical staining of Vegfa and Cd31 in iAP and iKAP tumors. Representative images (left) and quantification (upper right). Scale bar, 100  $\mu$ m;  $N \geq 3$  biological replicates. Flow analysis of Cd326-/Cd45-/Cd31+ endothelial cells in iAP and iKAP tumors (lower right).  $N = 3$  biological replicates. Data represent mean  $\pm$  SD. Student's  $t$  test.

Figure 4I. Representative images (upper panel), and quantification (lower panel) of the CD31 IHC staining in DLD1  $KRAS^{WT}$  and  $KRAS^*$  tumors. Scale bar, 100  $\mu$ m;  $n \geq 4$  biological replicates. Data represent mean  $\pm$  SD. Student's  $t$  test.

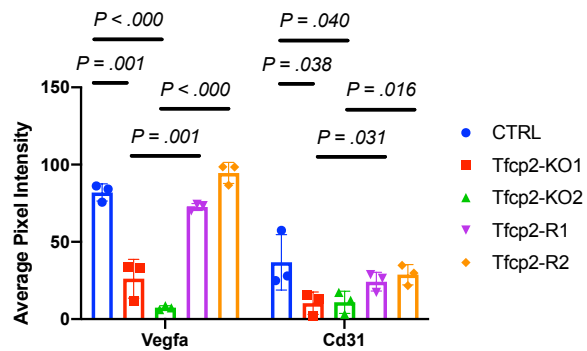
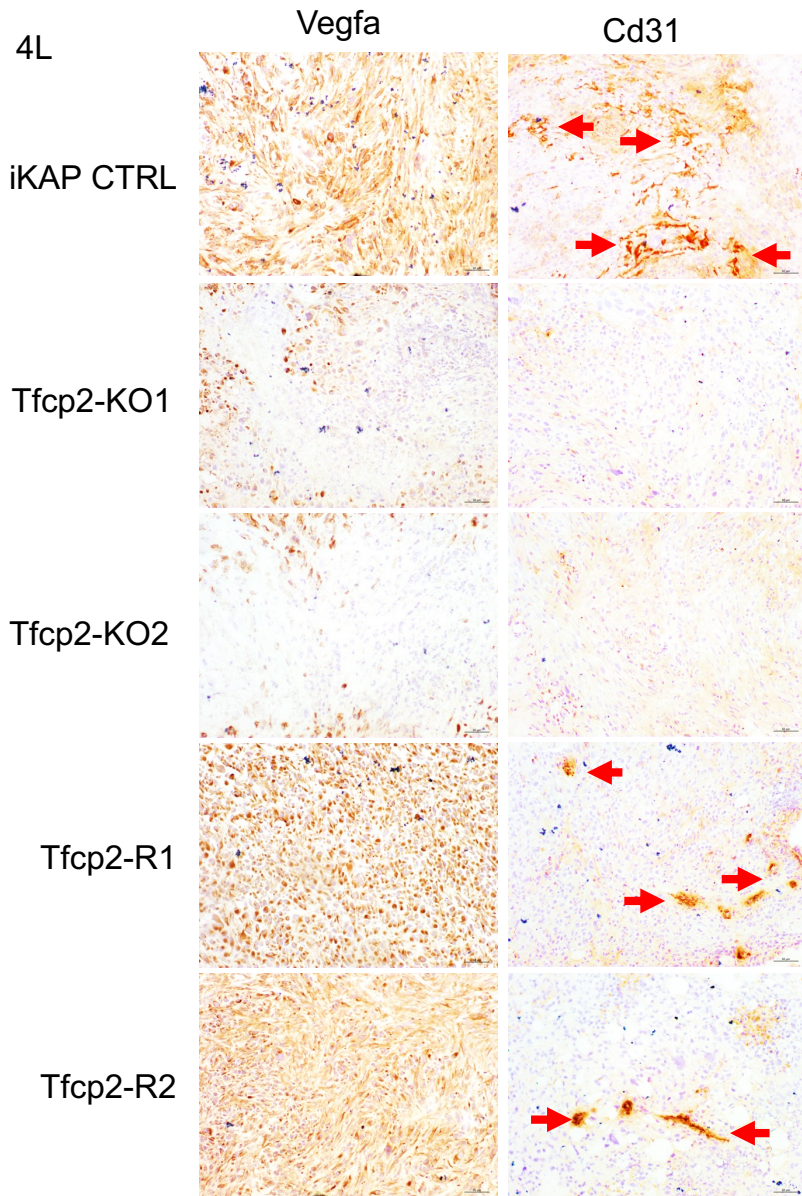
Figure 4J. Representative images (left panel) of immunofluorescence staining of lipid droplets, Vegfa, Pdgfra and Cd31 in orthotopic co-injection, non-invasive iAP and invasive iKAP tumors. White rectangles indicate the enlarged areas presented at the lower image. Red arrows indicate Cd31+ cells (upper and middle panels) and lipid droplets (lower panel). Quantification of Cd31 or Vegfa staining intensity (right panels).  $N \geq 4$  biological replicates Data represent mean  $\pm$  SD. Student's  $t$  test.

Figure 4K. The tube or capillary-like shapes of the HUVEC co-cultured with CM of DLD1  $KRAS^{G12D}$  CM-educated hMSCs. See Methods "Angiogenesis assay" for details.

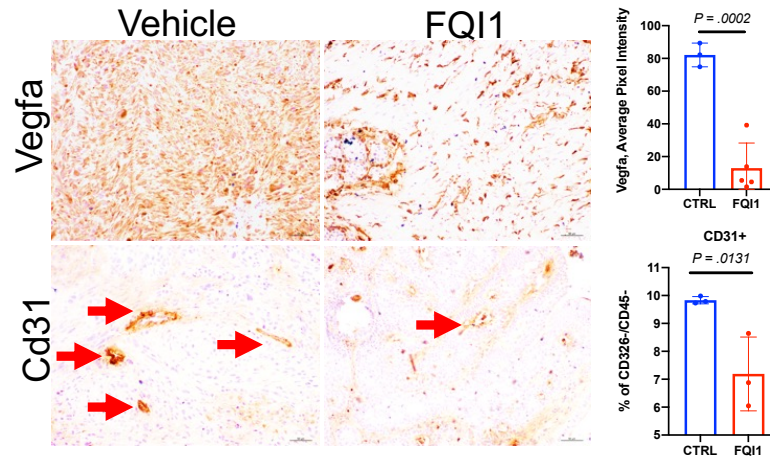
*Representative images (left) and quantification (right). Scale bar, 100  $\mu$ m; N = 3 biological replicates. Data represent mean  $\pm$  SD. Student's t test.*

Finally, the role of TFCP2 in mediating KRAS\*-induced lipofibrogenesis and angiogenesis has been confirmed through several key observations. Depletion of Tfc2 resulted in a decrease in Vegfa expression and a reduction in the density of endothelial cells in KRAS\*-expressing iKAP tumors compared to control tumors (Fig. 4L). Additionally, inhibiting Tfc2 with FQ11 led to reduced Vegfa expression and a decrease in the presence of Cd326-/Cd45-/Cd31+ endothelial cells in KRAS\*-expressing iKAP tumors (Fig. 4M). Analysis of the TCGA CRC dataset further supported the connection between *TFCP2* and *VEGFA*, as evidenced by the poor prognosis of CRC patients with high *VEGFA* expression, a *TFCP2*-high signature, or a combination of high *VEGFA* and *TFCP2* signatures (Fig. 3K and 4N). Correspondingly, treatment with FQ11 alone, the murine anti-VEGFA neutralizing antibody B20 alone, or a combination of both treatments all hindered CRC progression in iKAP GEM (Fig. 4O). These survival curves reveal two significant findings. First, treatment with FQ11 alone yielded results equivalent to combination treatment with FQ11 and B20, supporting VEGFA as a crucial downstream target of TFCP2. Second, FQ11 or FQ11+B20 treatments were more effective than B20 alone, suggesting that TFCP2 influences additional targets beyond VEGF, such as other angiogenesis-related factors mentioned earlier (Fig. 4D). In contrast, FQ11 treatment of the iAP CRC model had no impact on improving survival compared to vehicle-treated controls (Fig. 4P), thereby reinforcing the specificity of TFCP2 inhibition in angiogenesis, specifically in the context of KRAS\*. In summary, our findings indicate that KRAS\*-activated TFCP2 plays a pivotal role in the development of lipid-rich CAFs, primarily contributing to CRC progression through VEGFA-induced tumor angiogenesis. The preservation of the KRAS\*-TFCP2-VEGFA axis in human KRAS\*-driven CRC suggests its potential for translation into clinical research

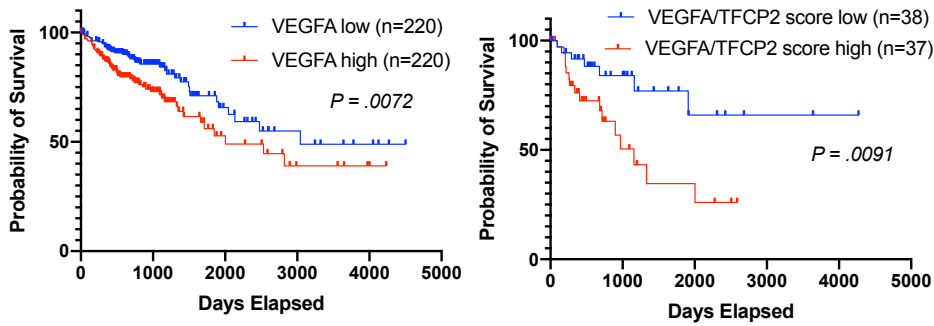
and raises the possibility that targeting TFCEP2 may be more effective than VEGFA neutralization in CRC.



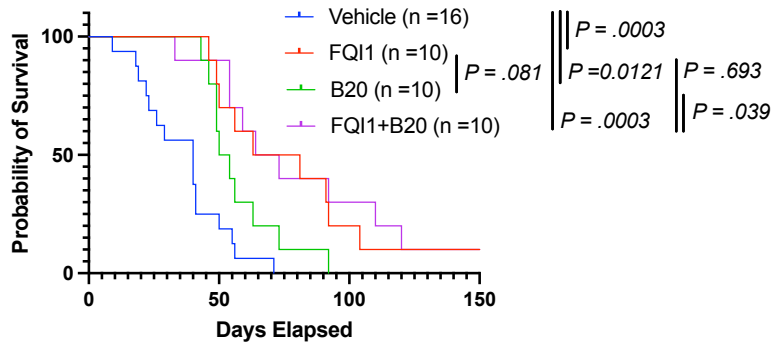
4M



4N



4O



4P

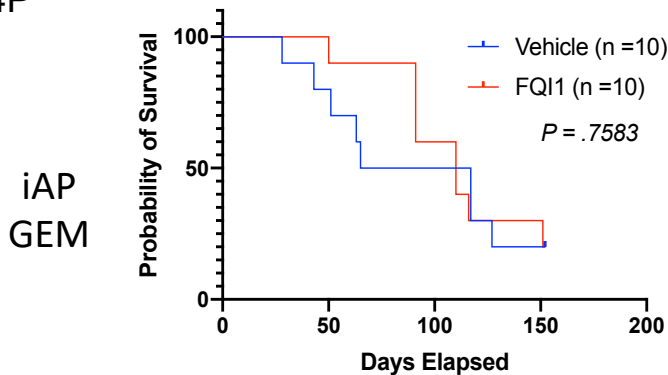


Figure 4L. IHC staining (upper panel) of Vegfa and Cd31 and quantification (lower panel) in *Tfcp2*-knockout and rescued *iKAP* tumors. Red arrows indicate positive staining of Cd31. Scale bar, 50  $\mu$ m; N = 3 biological replicates. Data represent mean  $\pm$  SD. Student's *t* test.

Figure 4M. Immunohistochemical staining of Vegfa and Cd31 in FQI1-treated *iKAP* tumors. Representative images (left) and quantification (upper right). Scale bar, 50  $\mu$ m; N = 3 biological replicates. Flow analysis of Cd326-/Cd45-/Cd31+ endothelial cells in FQI1-treated *iKAP* tumors (lower right). N = 3 biological replicates.

Figure 4N. Kaplan–Meier survival curves of high vs. low VEGFA expression (left) and high vs. low VEGFA expression plus TFCP2 GSVA score (right) in TCGA-COAD data from cBioPortal. VEGF high and low were defined using 50% cut-off of the RNA expression levels. VEGF/TFCP2 GSVA score  $\geq$  4th quantile was defined as high group and  $\leq$  1st quantile as low group. Log–rank (Mantel–Cox) test.

Figure 4O. Kaplan–Meier survival curves of *iKAP* mice treated with FQI1 and/or Vegfa monoclonal antibody treatment (single and combination). Log–rank (Mantel–Cox) test.

Figure 4P. Kaplan–Meier survival curves of *iAP* mice treated with FQI1 (single or combination treatment). GEM, genetically engineered mouse. Log–rank (Mantel–Cox) test.

**CHAPTER 7:**  
**THE IMPACT OF TELOMERE DYNAMICS**  
**BEYOND KRAS\* ON CRC**



## CHAPTER 7: THE IMPACT OF TELOMERE DYNAMICS BEYOND KRAS\* ON CRC

### 7.1 Preliminary research and rationale

Given that only a minority of cases, whether in humans or mouse models of KRAS\* CRC, progress to metastatic disease, it is evident that genetic events beyond KRAS activation are essential contributors to the metastatic process. The chromosomal instability pathway, known as CIN, has been identified in approximately 70% of progressive colorectal cancer (CRC) patients (Lengauer et al., 1998). This pathway, in conjunction with oncogenic activation pathways, plays a pivotal role in driving tumor progression (Pino et al., 2010). Our preliminary analysis of The Cancer Genome Atlas (TCGA) data also corroborated these findings, as we observed a positive correlation between the fraction of altered genomes and the incidence of cancer metastasis in CRC patients (Fig. 5A), underscoring the fundamental role of genomic instability in promoting metastasis. While our previous investigations have elucidated the impact of telomerase reactivation on bone metastases in a genetically engineered mouse (GEM) model of prostate cancer, the role of telomere dynamics in CRC progression remains inadequately understood. To address this knowledge gap, we developed a tamoxifen (TAM)-inducible telomerase reactivation model, denoted as iTAP, which integrates *LSL-TERT* within the iAP CRC GEM background. This approach capitalized on the non-metastatic phenotype characteristic of the iAP CRC GEM model, which exhibits a documented 0% metastasis rate and yields 57% adenoma formation. Prior studies by Karl Lenhard Rudolph et al. (1999) and Mariela Jaskelioff et al. (2011) highlighted that the fourth generation (G4) telomerase holoenzyme *Tert*<sup>-/-</sup> exhibited reduced survival compared to mice with intact telomeres (medium overall survival from 27 months decreased to 24 months) (Fig. 5B). Additionally, G4 inducible *Tert*<sup>-/-</sup> primary splenocytes displayed discernible features of short and dysfunctional

telomeres, as evidenced by telomere-specific fluorescence in situ hybridization (FISH) signals (Fig. 5C). Notably, the fourth generation exhibited these biological phenotypes of telomere shortening and decreased survival. Therefore, our establishment of the iTAP mouse model (Fig. 5D) involved a meticulous breeding strategy, extending through multiple generations until the fourth, to facilitate subsequent investigations in this context.

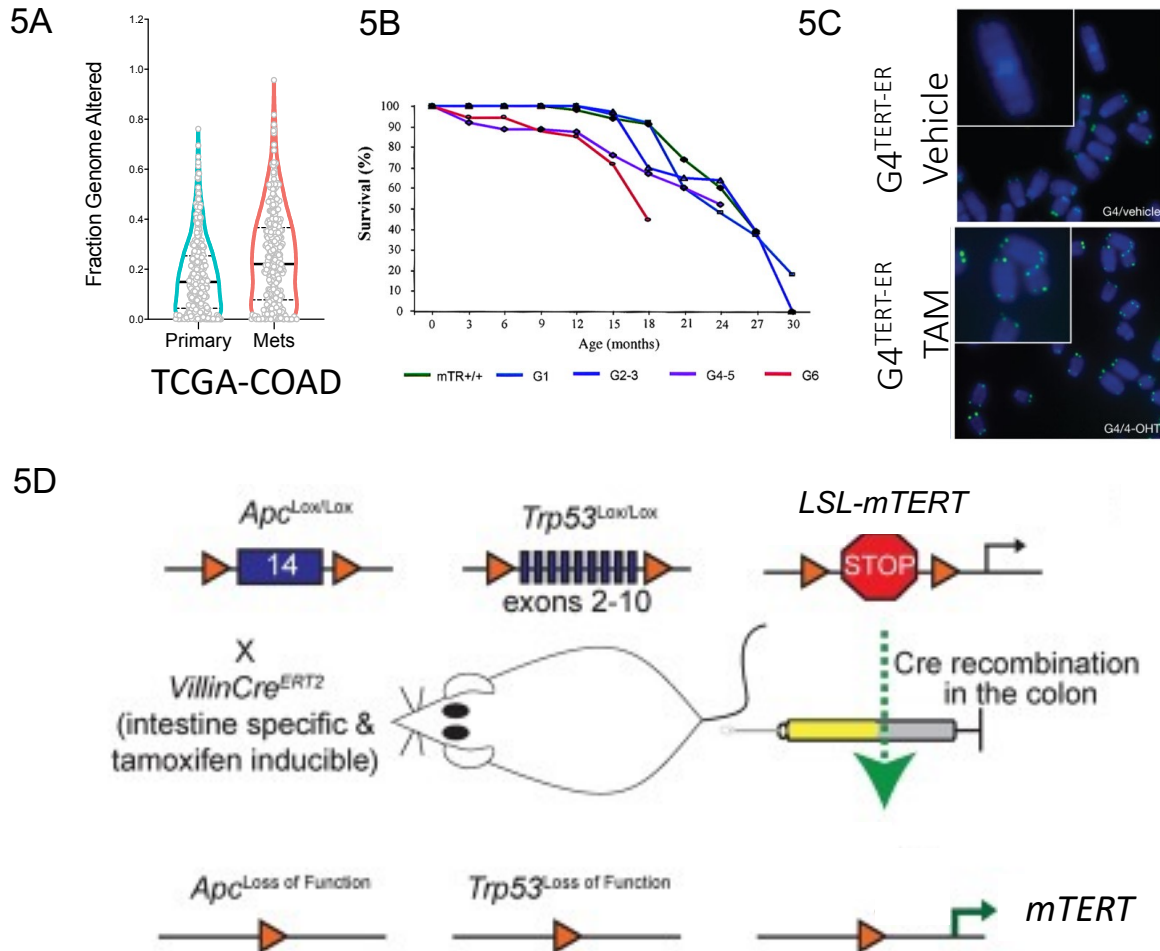


Figure 5A. Fraction genome altered score analysis in TCGA-COAD data from cBioPortal comparing primary and metastatic tumors.

Figure 5B. Survival analysis comparing *Tert*<sup>+/+</sup> (G0), and *Tert*<sup>-/-</sup> first to sixth generation (G1 to G6). Log-rank (Mantel-Cox) test.

Figure 5C. Telomere-specific fluorescence in situ hybridization signals in inducible G4 *Tert-ER* splenocyte metaphases

Figure 5D. Schematic diagram of genotyping in iTAP mouse.

## 7.2 Results

To explore the biological implications of telomere dynamics in CRC progression, I initiated tumor formation through tamoxifen (TAM) induction in both iTAP G0 and G4 cohorts. In iTAP G0 (*LSL-Tert*<sup>+/+</sup>;*Apc*<sup>-/-</sup>;*P53*<sup>-/-</sup>), telomeres remain intact, while iTAP G4 (*LSL-Tert*<sup>-/-</sup>;*Apc*<sup>-/-</sup>;*P53*<sup>-/-</sup>) represents the fourth generation with homozygous *LSL-Tert* and shortened telomeres. Both iTAP G0 and G4 models entail inducible *Apc* and *Tp53* deletions followed by telomerase reactivation upon TAM administration. The dynamics of telomeres and telomerase during CRC progression are depicted in Figure 5E. Assessing the impact of telomerase reactivation after telomere-based crisis on mouse survival, we observed a significant difference between iTAP G0 and G4. iTAP G0 displayed a median overall survival of 30 weeks, while iTAP G4 declined to 10 weeks (Figure 5F). This suggests that telomerase reactivation subsequent to telomere-based crisis supports tumor formation and compromises mouse survival. This biological effect aligns with our previous findings in prostate cancer, where telomerase reactivation increased the incidence of bone metastases and decreased survival in a *Tp53/Pten*<sup>-/-</sup> GEM model. Importantly, the reduced survival cannot be attributed to the physiological weakness of mice, as fourth generation (G4) *Tert*<sup>-/-</sup> mice exhibited a median overall survival of 24 months compared to telomere-intact (G0) mice with a median overall survival of 27 months.

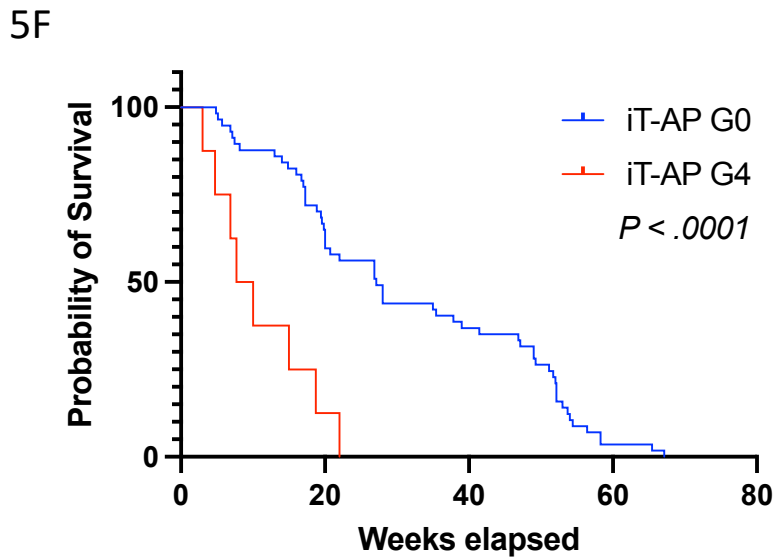
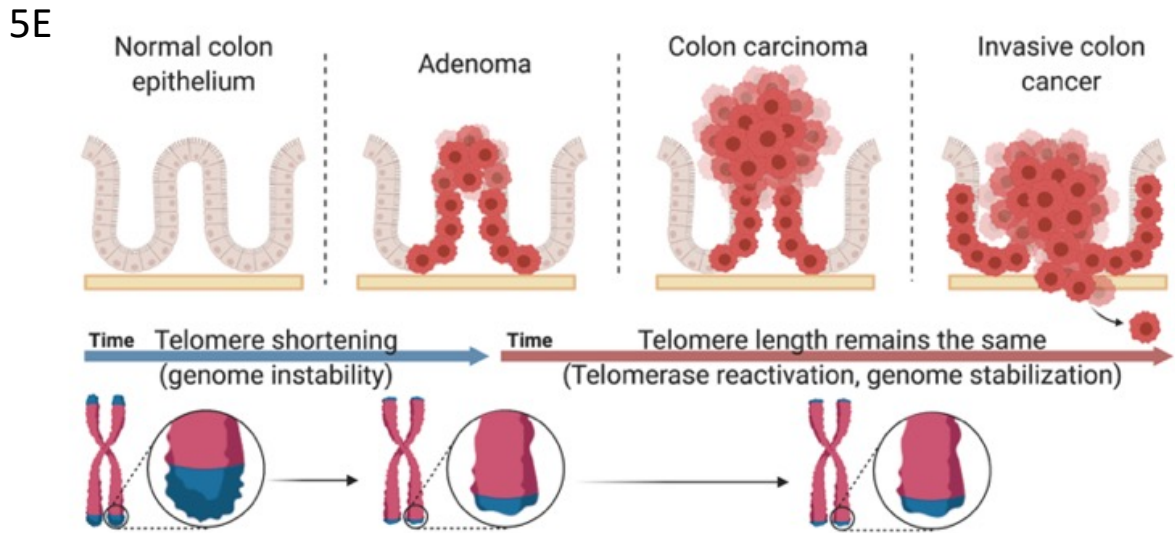
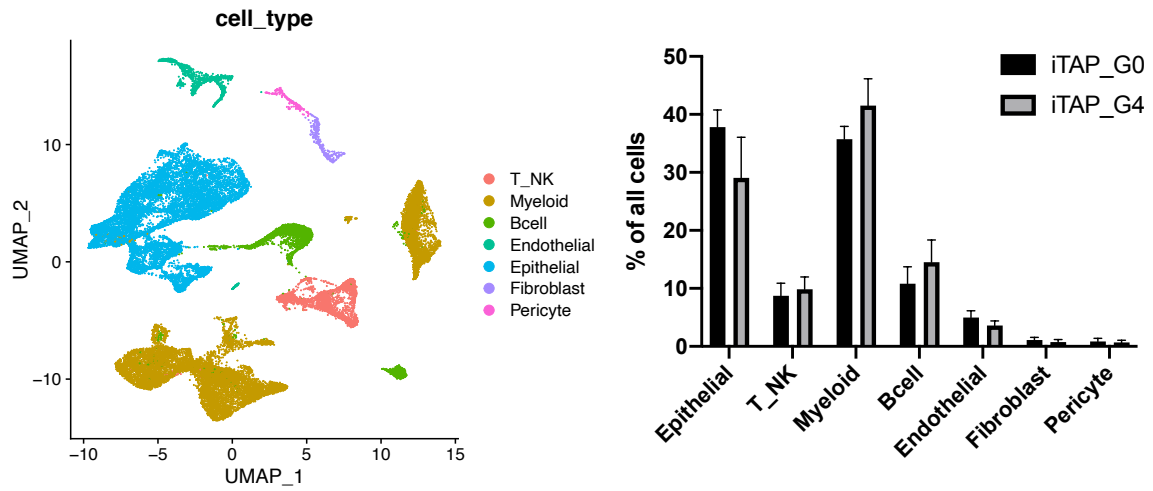


Figure 5E. Schematic diagram of the dynamics of telomeres and telomerase during CRC progression.

Figure 5F. Kaplan–Meier survival curves of iTAP mice comparing G0 to G4 (single or combination treatment). GEM, genetically engineered mouse. Log–rank (Mantel–Cox) test.

To elucidate the mechanistic underpinnings of telomere dynamics-driven CRC progression, we conducted scRNA-seq comparisons across three independent iTAP G0 and G4 CRC tumors. Among the 34,900 cells analyzed, we employed classical cell type markers to identify epithelial, myeloid, lymphoid, endothelial cells, pericytes, and fibroblasts (Figure 5G). No significant differences in cell proportions were observed when comparing G0 and G4 CRC tumors, confirming the methodological rigor of our analysis. Our attention subsequently turned to epithelial cells, given that both iTAP G0 and G4 GEM models feature the *Villin-Cre* gene, which expresses Cre recombinase in intestinal epithelial cells, leading to the deletion of *Apc* and *Tp53* and telomerase reactivation. Characterizing the impact of telomere dynamics in epithelial cells unveiled heterogeneity within CRC tumors, encompassing diverse consensus molecular subtypes (CMS) subtypes (Figure 5H). Importantly, we found no significant differences in the proportions of various tumor subtypes. This suggests that telomerase reactivation following telomere-based crisis does not regulate the shift in CMS in *Apc*<sup>-/-</sup> and *P53*<sup>-/-</sup> colorectal cancer.

5G



5H

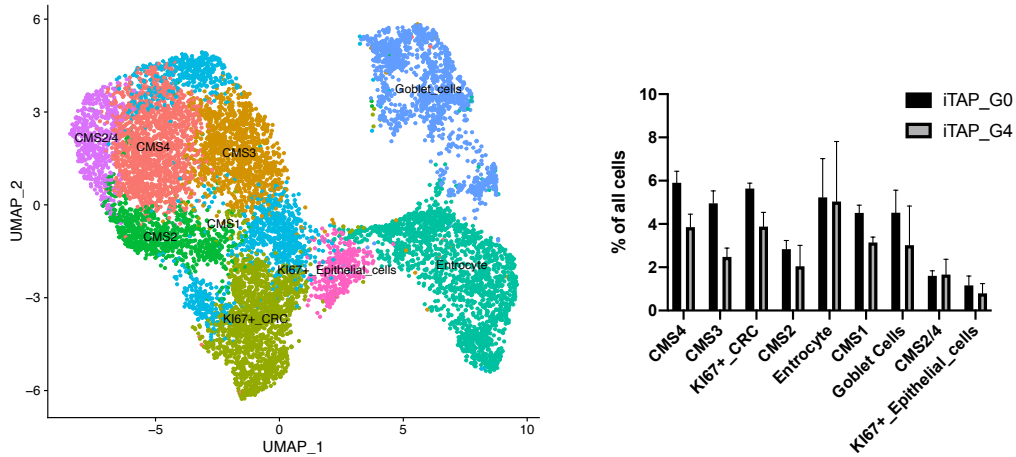


Figure 5G. Single-cell sequencing annotations for all cell types in iTAP G0 and G4 tumors (left panel).  $N = 3$  biological replicates. The proportion of each cell types in percentage of all cells (right panel).  $N = 3$  biological replicates.

Figure 5H. Single-cell sequencing annotations for all epithelial cell subtypes in iTAP G0 and G4 tumors (left panel).  $N = 3$  biological replicates. The proportion of each epithelial cell subtypes in percentage of all cells (right panel).  $N = 3$  biological replicates.

It is widely acknowledged that the initiation of telomere crisis leads to chromosomal instability (CIN), resulting in the emergence of chromothripsis and genomic aberrations, which instigate gene mutational processes (Maciejowski et al., 2015). To explore these phenomena, we conducted inferred copy number alteration (CNA) analyses using scRNA-seq data and the CopyKAT (Copynumber Karyotyping of Tumors) computational tool. While the distribution of tumor CMS exhibited no significant differences between G0 and G4 CRC tumors, our analysis revealed a predominant presence of epithelial cells with inferred CNAs in iTAP G4, when compared to iTAP G0 (Fig. 5I). To delve deeper into this observation, we performed unsupervised clustering of these aneuploid cells and mapped the major CNA clusters to epithelial UMAP clusters. Importantly, we observed that the primary CNAs predominantly occurred in tumor cells, hereafter referred to as CIN events, exhibiting the characteristic features of consensus molecular subtypes (Fig. 5J). Notably, these CIN events were notably more prevalent in iTAP G4 tumor cells compared to iTAP G0 (Fig. 5K). Remarkably, iTAP G0 exhibited minimal to no CIN events, underscoring that, although Apc and P53 deletions drive tumor initiation by regulating uncontrolled growth, they are insufficient to induce CIN—the principal catalyst of gene mutational processes responsible for elevating the mutational burden during tumor progression. This result corroborates our earlier findings in the iAP GEM model, where 66% of iAP tumors were classified as adenomas or in situ tumors, with only 6% classified as T2 tumors and no tumors characterized beyond T2 (Boutin et al., 2017).





*Figure 5I. Heatmap representation of inferred copy number karyotyping in iTAP G0 and G4 tumors. N = 3 biological replicates.*

*Figure 5J. Single-cell sequencing annotations for the major inferred CNAs in iTAP G0 and G4 epithelial cells. N = 3 biological replicates.*

*Figure 5K. The CIN events in iTAP G0 and G4 tumor cells. N = 3 biological replicates. Student's t test.*

Given the unexpected findings and the accuracy of inferred CNA analyses in GEM, we aim to extend our investigation to human studies, thereby enhancing the clinical relevance of exploring potential targets in telomere dynamics-driven CRC progression. In this regard, we conducted inferred CNA comparisons within a cohort of seven human microsatellite stable (MSS) CRC tumors characterized by APC and P53 mutations (Lee et al., 2019). It is noteworthy that MSS colorectal cancers exhibit normal levels of mismatch repair genes, which recognize a lower number of tumors neoantigens and are less responsive to immune therapy. In our analysis, spanning 11,558 epithelial cells, we classified patients into CIN high and low groups based on their percentage of diploid cells (Fig. 5L). This result will be integrated with our GEM analysis to further validate the mechanistic role of telomere dynamics in CRC progression in the subsequent chapter.

5L

MSS-AP (KRAS, BRAF, SMAD4 WT)

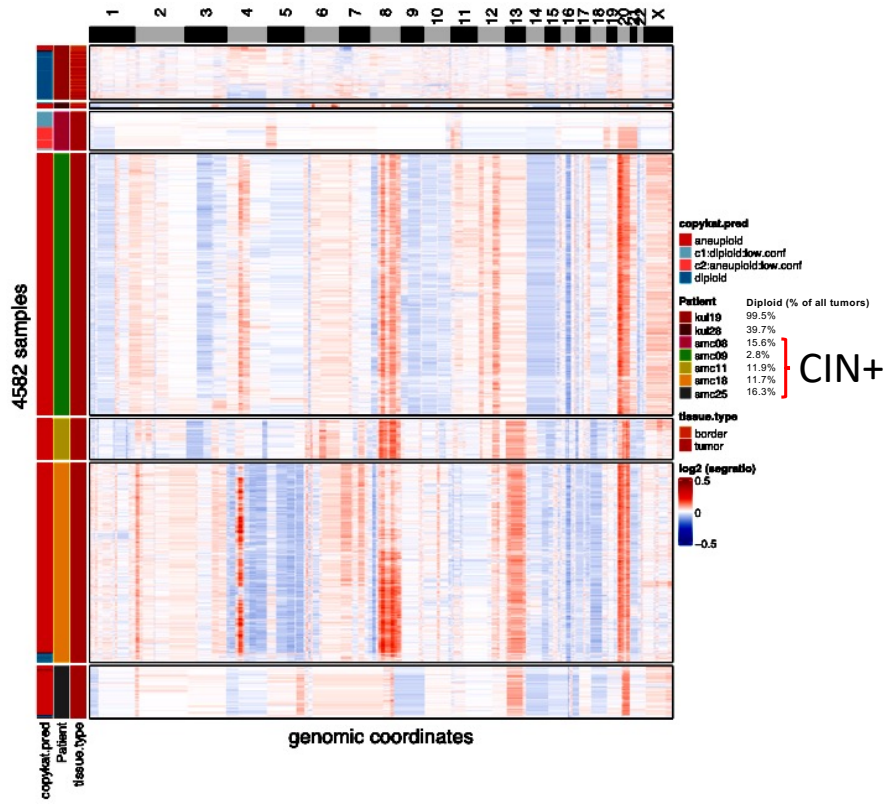


Figure 5L. Heatmap representation of inferred copy number karyotyping in human CRC scRNAseq.  $N = 7$ .

**CHAPTER 8:**  
**TELOMERE DYNAMICS-DRIVEN CHROMOSOMAL**  
**INSTABILITY MODULATES TUMOR IMMUNITY**

## **CHAPTER 8: TELOMERE DYNAMICS-DRIVEN CHROMOSOMAL INSTABILITY MODULATES TUMOR IMMUNITY**

### **8.1 Preliminary research and rationale**

Advanced colorectal cancers CRCs characterized by high CIN present an immunologically cold phenotype within their tumor microenvironments. This phenotype is characterized by a reduced presence of critical immune cell populations, including CD8+ T cells, NK cells, B cells, CD4+ T cells, dendritic cells (DCs), macrophages, and regulatory T cells (Tregs), leading to limited immune cell infiltration. Notably, high CIN CRCs are well-documented for their resistance to immune checkpoint inhibitors, prompting extensive research aimed at uncovering the underlying mechanisms responsible for suppressing the anti-tumor immune response. Our preliminary data have illustrated that the introduction of telomere dynamics into our iAP model can further enhance its suitability for investigating how CIN influences tumor immunity. In early-stage neoplasms, telomere dysfunction triggers the release of cytosolic dsDNA fragments, activating the cGAS/STING pathway. This activation, in turn, initiates a potent anti-tumor immune response primarily through the type I interferon-mediated pathway, involving the priming and infiltration of T-cells. However, as tumors progress, CIN itself exhibits a positive correlation with a low immune score, indicative of an immunologically cold state within the tumor microenvironment (TME). This correlation may arise from the acquisition of genetic events that actively suppress anti-tumor immunity. Consequently, a central focus of this chapter is to comprehensively explore how CIN contributes to the transition towards an immune-suppressive state during the progression of CRC tumors.

To investigate whether immune-suppressive mechanisms constitute the primary biological pathways affected by telomere dynamics-induced CIN in CRC, comprehensive GSEA pathway analyses were conducted in both GEM models and human CRC scRNA-seq datasets, comparing CIN-high and CIN-low conditions. In brief, the CIN-high GEM CRC dataset was derived from tumors displaying a predominant population of inferred CNAs, while the CIN-high human CRC dataset was based on tumors with a low predicted diploid cell count. By intersecting the enriched pathways in both datasets, a total of 26 common pathways emerged as significantly enriched in CIN-high CRC. These pathways encompassed categories such as defense response, development, cell motility, and survival. Remarkably, among the defense response pathways enriched in CIN-high CRC, the top five included cellular responses to stress, regulation of the immune system, leukocyte differentiation, and viral life cycle. Notably, telomere crisis following telomerase reactivation is well-established to induce cellular stress responses. Furthermore, the release of cytosolic dsDNA fragments during telomere crisis activates the cGAS/STING pathway, which exhibits similarities with the "viral life cycle" pathway within the GSEA database. Of particular interest, the activation of the pathways related to the regulation of the immune system and leukocyte differentiation underscores the previous hypothesis that CIN plays a role in modulating an immunologically cold state within the TME as tumors progress (Fig. 6A). These findings shed light on the intricate relationship between telomere dynamics-induced CIN and the immune-suppressive landscape of CRC.

6A

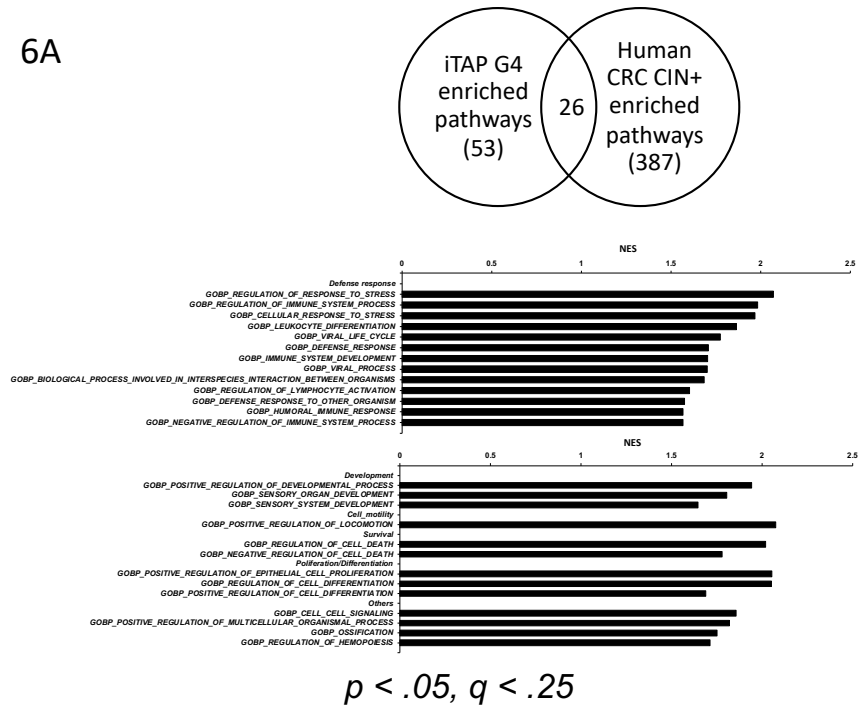


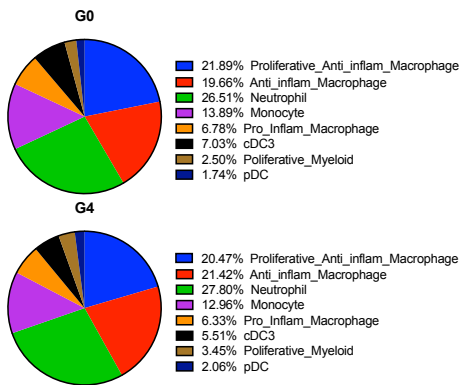
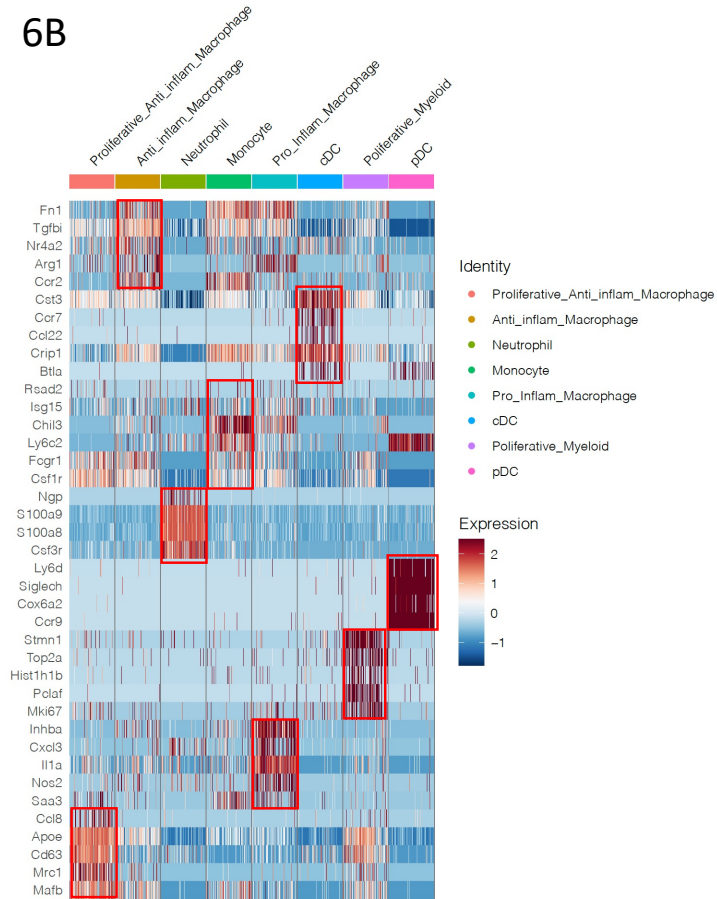
Figure 6A. Venn diagram of the GOBP pathways (upper panel) from GSEA database enriched in iTAP G4 tumor and CIN high human CRC (lower panel.  $N = 6$  in iTAP and  $N=7$  in human CRC).

## 8.2 Results

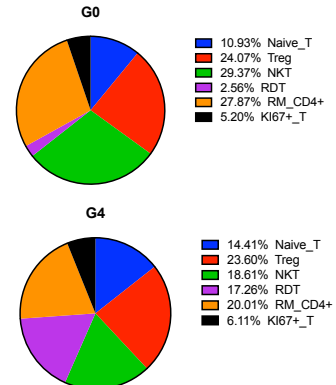
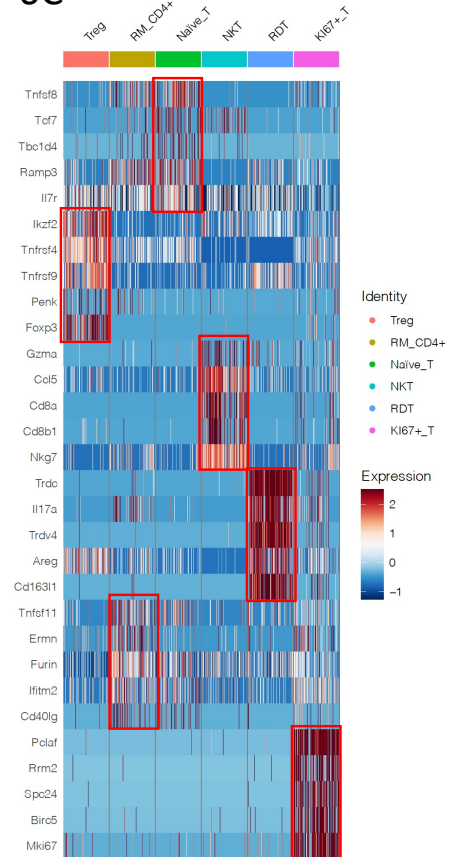
To delve deeper into the mechanistic insights regarding how telomere dynamics-induced CIN influences the immune-suppressive landscape of CRC, we employed classical cell type markers to discern the specific subtypes within the myeloid and lymphoid cell populations. When comparing G0 and G4 CRC tumors, we observed no significant differences in the subtype proportions of myeloid cells (Fig. 6B). However, a notable disparity was evident in the gamma-delta T cell (RDT) population between G0 and G4 CRC tumors (Fig. 6C). These gamma-delta T cells, identified by their expression of cell type marker genes *Trdc* and *Trdv4*, exhibited differential expression of genes such as *Il17a* and *Areg*, which have previously been

reported to exert protumor effects within the tumor microenvironment (Harmon et al., 2023). The unexpected finding of an increased population of protumor gamma-delta T cells in CIN-high GEM CRC prompted us to extend our investigation to human studies, thereby enhancing the clinical relevance of exploring potential targets associated with telomere dynamics-induced CIN and its influence on the immune-suppressive landscape of CRC. In this context, we conducted an analysis to quantify the number and percentage of lymphoid cell subtypes in microsatellite stable (MSS) CRC tumors harboring *APC* and *P53* mutations. Intriguingly, while an increase in gamma-delta T cells was observed in CIN-high human CRC, a significant expansion of T helper 17 cells (Th17) was noted instead of gamma-delta T cells (Fig 6D). Although this finding highlights differences in the immune compartment between mice and humans, it underscores the notion that telomere dynamics-induced CIN in CRC leads to the augmentation of IL17-expressing cells, be it gamma-delta T 17 in mice or Th17 in humans. Furthermore, the shared utilization of cytokines such as IL1b, IL12, and IL23 in the development of gamma-delta T 17 cells in mice and Th17 cells in humans (Mills et al., 2023) suggests that CIN-induced changes in these cytokines contribute to the maturation of IL17-expressing cells across both species.

6B



6C





6D

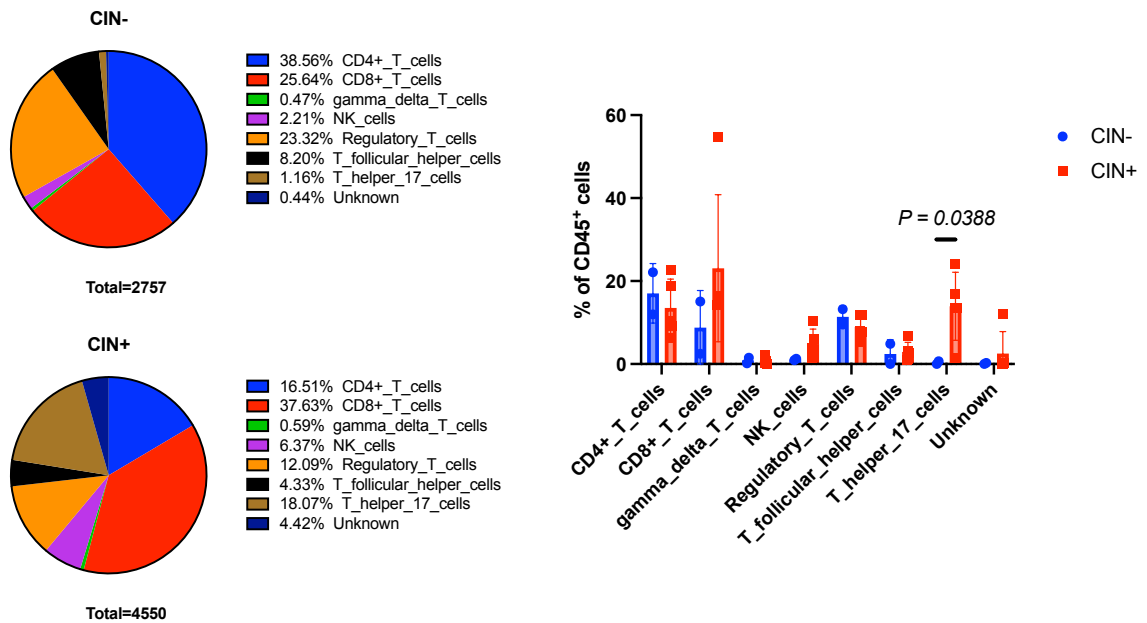


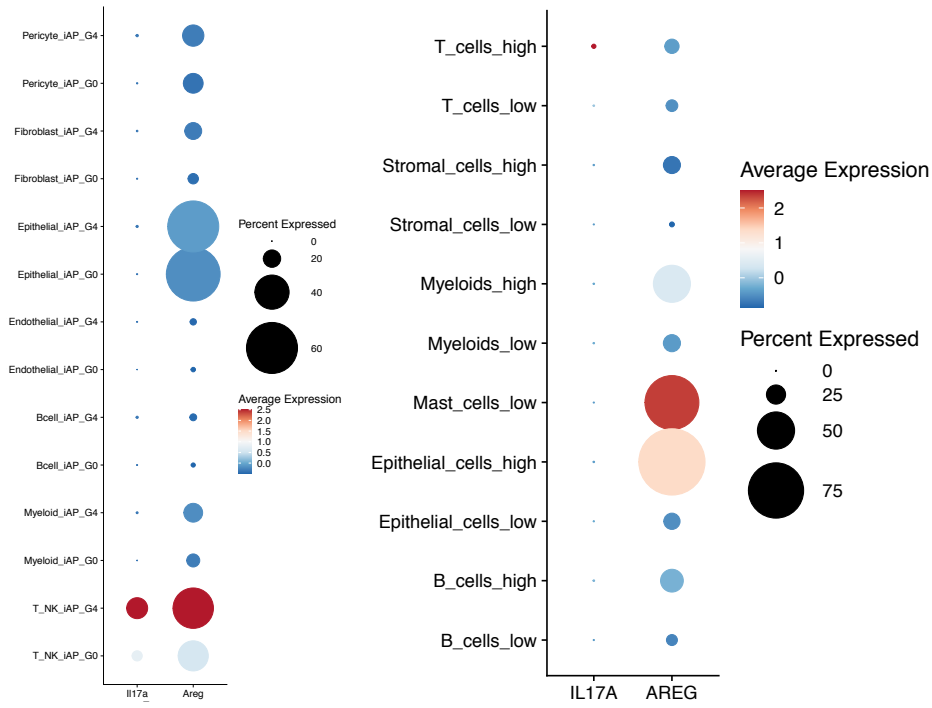
Figure 6B. Single-cell sequencing annotation of myeloid cells in iTAP G0 and G4 tumors. Heatmap of differential expression marker genes of myeloid cell subgroups (upper panel). The proportion of myeloid cell subgroups (lower panel).  $N = 6$  biological replicates.

Figure 6C. Single-cell sequencing annotation of lymphoid cells in iTAP G0 and G4 tumors. Heatmap of differential expression marker genes of lymphoid cell subgroups (upper panel). The proportion of lymphoid cell subgroups (lower panel).  $N = 6$  biological replicates.

Figure 6D. The proportion of myeloid cell subgroups in CIN high and low human CRC. (left panel). The proportion of myeloid cell subgroups to all CD45 positive cells in CIN high and low human CRC (right panel).  $N = 7$ .

The transcriptomic analysis in the dot plot also confirms our previous observations, showing elevated expression levels of *Il17a* and *Areg* in both iTAP G4 and CIN-high CRC, specifically within the T cell population (Figure 6E). It is noteworthy that while *Areg*-positive gamma T cells have been traditionally classified as immunosuppressive protumor cells within the tumor microenvironment, our analysis reveals that *Areg* is also expressed in mast cells and epithelial cells in human CRC. This suggests that AREG may have functions beyond immune suppression or may be contributed by different cells in TME in both mouse and human CRC settings. To further validate our computational findings regarding the increase in gamma-delta T 17 cells within the TME, we performed immunohistochemistry staining on iTAP G0 and G4 tumor tissue slides. We targeted TCR  $\gamma/\delta$  (a specific marker for gamma-delta T cells) and ROR $\gamma$  (the transcription factor responsible for regulating the differentiation of gamma-delta T 17 cells). The staining for TCR  $\gamma/\delta$  and ROR $\gamma$  exhibited significantly higher levels in iTAP G4 tumors compared to G0, providing robust experimental support for our earlier computational findings (Fig. 6F). These results underscore the impact of telomere dynamics-induced CIN in CRC, which leads to an increase in gamma-delta T 17 cells in murine models.

# 6E



CRC  
GEM

Human  
CRC

# 6F

iTAP G0

iTAP G4

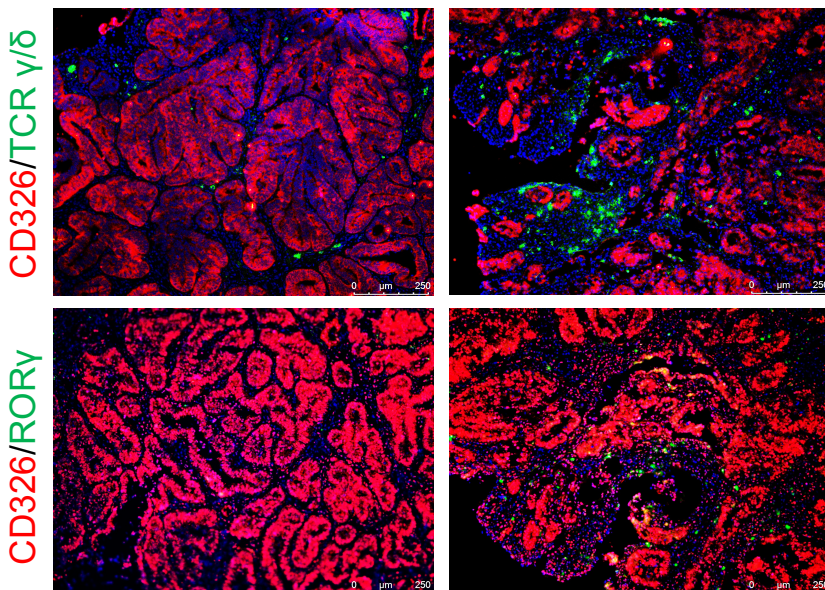
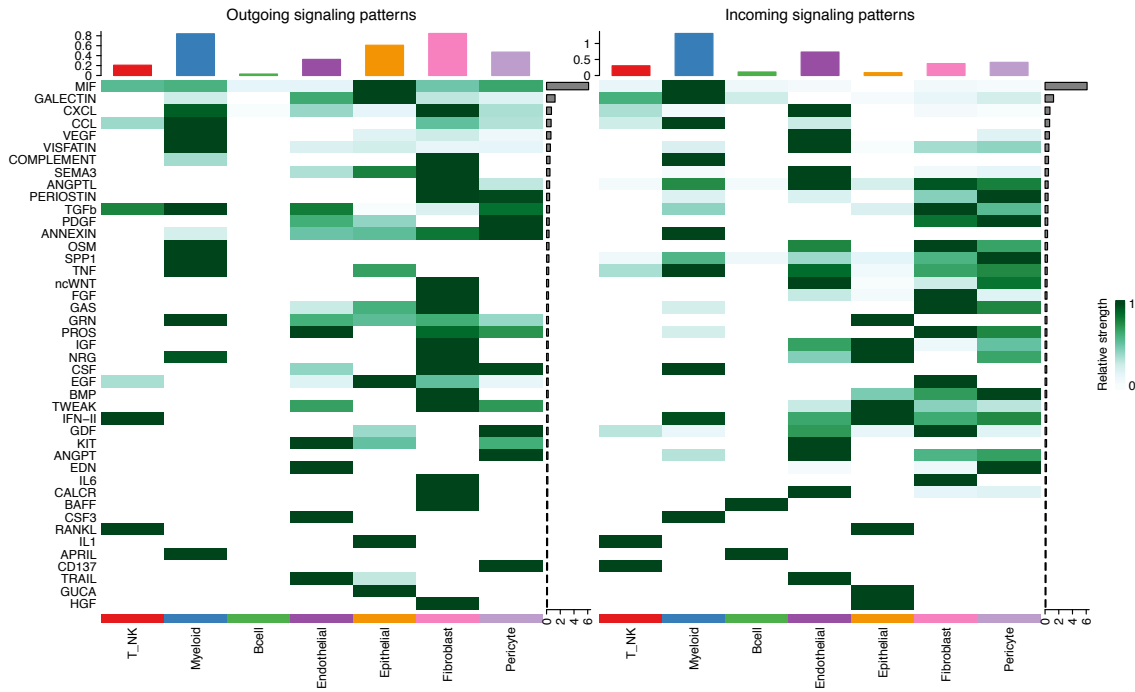


Figure 6E. IL17A and AREG mRNA expression level in all cell subtypes in iTAP G0 and G4 tumors; and human CIN high and low CRC using scRNA-seq. The average expression color scale was from 2.5 to -1. The dot size represents the proportion of expressing cells in each group. N = 6 biological replicates in iTAP and N = 7 biological replicates in human CRC.

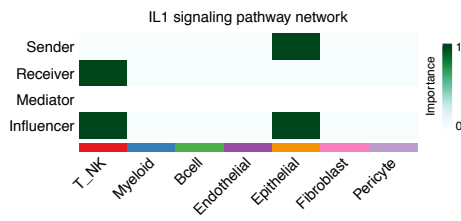
Figure 6F. Immunohistochemical staining of TCR  $\gamma/\delta$  and ROR $\gamma$  in iTAP G4 and G0 tumors. N = 6 biological replicates.

Given the shared utilization of IL1b, IL12, and IL23 in the development of gamma-delta T 17 cells in mice and Th17 cells in humans, as previously documented (Mills et al., 2023), we posited that CIN in epithelial cells may be responsible for the expression of IL1b, IL12, and IL23, thus driving the differentiation of T cells into gamma-delta T 17 cells in mice and Th17 cells in humans. To investigate this hypothesis, we conducted ligand-receptor interaction analyses using the computational tool CellChatDB. Our unbiased examination of epithelial cell-T cell interactions revealed a robust connection mediated by *Galectin*, *CXCL*, *TNF*, *GDF*, and *IL1* (Figure 6G). Notably, among these interactions, IL1 emerged as a prominent cytokine that likely regulates the differentiation of gamma-delta T 17 cells in mice and Th17 cells in humans (Figure 6H). This significant finding was further corroborated by transcriptomic dot plot analyses, which revealed specific *Il1b* expression in epithelial cells within both iTAP G4 and CIN-high human epithelial tumor cells. Together, these discoveries suggest a mechanistic pathway wherein CIN-high epithelial cells secrete IL1B to promote the differentiation of gamma-delta T or T helper cells into IL17-expressing cells, ultimately modulating the immunosuppressive TME and facilitating CRC progression. In summary, our study provides valuable insights into the intricate interplay between telomere dynamics-induced CIN and the immune landscape of CRC.

6G



6H



6I

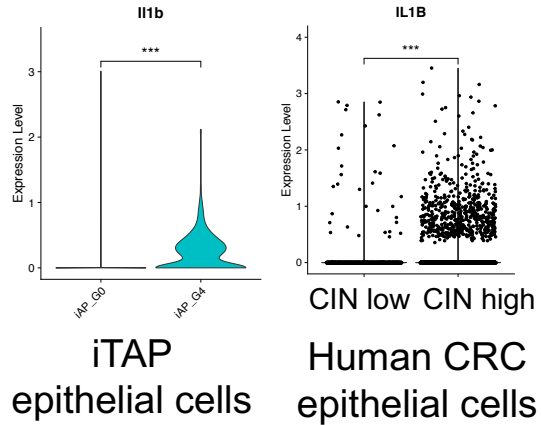


Figure 6G. Ligand-receptor interaction analyses using the CellChatDB in iTAP scRNAseq.

The importance color scale was from 1 to 0. N = 6 biological replicates.

Figure 6H. IL1 ligand-receptor interaction analyses using the CellChatDB in iTAP scRNAseq.

The importance color scale was from 1 to 0. N = 6 biological replicates.

Figure 6I. IL1B mRNA expression level in iTAP and human CRC scRNAseq. The importance

color scale was from 1 to 0. N = 6 biological replicates in iTAP and N = 7 biological replicates in human CRC.

**CHAPTER 9:**  
**CONCLUSIONS AND DISCUSSION**

## CHAPTER 9: CONCLUSIONS AND DISCUSSION

Content of this chapter is partly based on the following manuscript:

Hsu, W.H., LaBella, K. A., Lin, Y., Xu, P., Lee R., Hsieh, C.E., Yang, L., Zhou, A., Blecher, J. M., Wu, C. J., Lin, K., Shang, X., Jiang, S., Spring, D. J., Xia, Y., Chen, P., Shen, J. P., Kopetz, S., DePinho, R. A. (2023) "Oncogenic KRAS drives lipo-fibrogenesis to promote angiogenesis and colon cancer progression" *Cancer Discov*, 10.1158/2159-8290.CD-22-1467

In the initial phase of my research, I delved into the intricate mechanisms governing the progression of CRC induced by KRAS\*. Our investigation unveiled the pivotal role of KRAS\* in triggering TFCP2-mediated transcriptional upregulation of proadipogenic cytokines within cancer cells. Subsequently, this upregulation led to the transformation of CAFs into lipid-rich entities within the tumor microenvironment. These lipid-rich CAFs, in turn, generated a substantial amount of VEGFA, promoting angiogenesis and furthering the progression of the disease. Significantly, our study demonstrated that genetic or pharmacological interventions targeting TFCP2 effectively curtailed CAF adipogenesis, mitigated tumor angiogenesis, and impeded the growth of tumors in both mouse and human CRC models expressing the KRAS\* mutation. This research illuminates a novel facet of KRAS\* activity, expanding its known functions to encompass the phenotypic transformation of CAFs with heightened pro-tumorigenic characteristics. The proposed mechanism is shown in a schematic diagram for easy understanding (Figure 7A). Our findings also suggest that the KRAS\*-TFCP2-VEGFA axis presents a viable and testable therapeutic avenue for patients with KRAS\*-driven CRC.

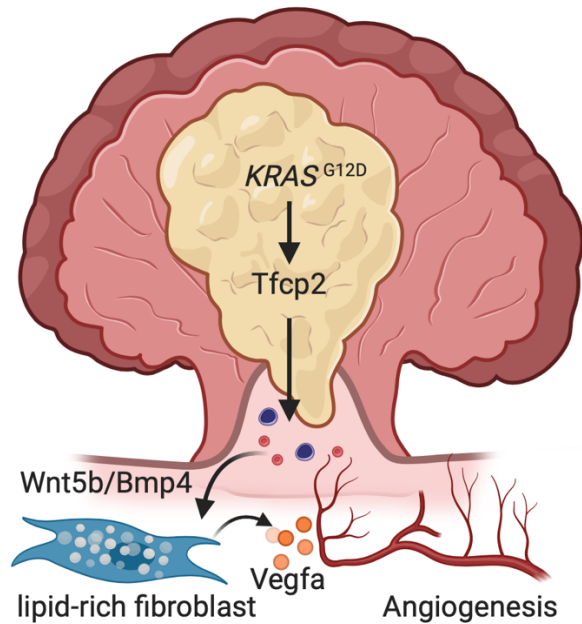


Figure 7A. Schematic diagram of the proposed mechanism that regulates the progression of CRC through the KRAS\*-TFCP2-VEGFA axis.

The CAF cells loaded with lipids, as identified in this study, share striking resemblances to lipid interstitial cells found in the developing murine lung (Kaplan et al., 1985, O'Hare et al., 1970) and cells engaged in adipogenesis (Cristancho et al., 2011). Firstly, mirroring the lipid-rich interactions between CAFs and endothelial cells, lung lipofibroblasts foster the growth of stem cells (Barkauskas et al., 2013, McQualter et al., 2013) by enhancing oxidative defenses, supplying leptin to stimulate surfactant production in type 2 alveolar epithelial cells, and encouraging the proliferation of type 2 cells (Rehan et al., 2014). Secondly, further parallels between lipid-rich CAFs and alveolar lipofibroblasts are evident in lineage-tracing analyses. These analyses reveal that PDGFR $\alpha$ + progenitor stromal cells differentiate into alveolar lipofibroblasts (Ntokou et al., 2015), characterized by an abundance of neutral lipids, lipid droplet-associated protein (perilipin), adipocyte markers such as TCF21, FABP4, LPL, and ZFP423, as well as membrane-tethered COL13A1 and FGF10 (McGowan et al., 2014; Park et al., 2019; Sanchez—Gurmaches et al., 2016). Similarly, lipid-rich CAFs and alveolar



lipofibroblasts share a comparable gene expression profile, including LPL, perilipin, TCF21, FGF10, PI16, CLO12A, and MMP13. Thirdly, both lipofibrogenesis and adipogenesis involve FGF10 in the conversion of PDGFR $\alpha$ + preadipocytes into beige adipocytes via a miRNA-327-FGF10-FGFR2 autocrine loop (Cristancho et al., 2011). Similarly, the expression of FGF10 induced by KRAS CM educated and transformed embryonic fibroblast and mesenchymal stem cells into lipid-rich fibroblasts in cell culture. KRAS exhibited similar functions in the iKAP tumor microenvironment. Among the commonalities between lipid-rich CAFs and adipocytes is their shared origin from a common progenitor cell, the PDGFR $\alpha$ + preadipocyte (Lv et al., 2021). In adipogenesis, the inhibition of canonical WNTs and the activation of BMP signaling facilitate the commitment of preadipocytes to an adipogenic fate, with insulin stimulating adipocyte maturation and lipid droplet accumulation. Correspondingly, iKAP cell lines demonstrate KRAS\*-dependent enrichment of the two main proadipogenic cytokines, BMP4 and WNT5B; iKAP bulk tumors and KRAS\*-driven tumor stroma exhibit insulin pathway signaling, consistent with an active adipogenesis process in KRAS\* stroma. These collective findings underscore that lipid-rich CAFs employ mechanisms akin to those governing normal lipofibrogenesis and adipogenesis programs.

Our focus on angiogenesis primarily stems from several key observations and analyses within our study. Firstly, an examination of tumor histopathology clearly demonstrates a robust association between KRAS\* and heightened tumor angiogenesis. Secondly, a comprehensive GSEA of KRAS\*-regulated pathways, shared and enriched in both mouse and human KRAS\*-associated CRC, revealed a compelling and substantial correlation between pathways involving epithelial-mesenchymal transition (EMT) and angiogenesis. This correlation was particularly pronounced in conjunction with the gene signature of lipid-rich CAFs. Thirdly, in-depth analyses of cytokine arrays focusing on the secreted factors from CAFs identified the presence of VEGFA, MCSF, DLK1, HGF, and LCN2 in the conditioned medium of embryonic

fibroblasts cultured with KRAS\* (resulting in the development of lipid-rich CAFs). These multiple lines of evidence provide strong support for our emphasis on angiogenesis as a fundamental hallmark under the regulation of lipid-rich CAFs in KRAS\*-associated CRC. Moreover, our prioritization of angiogenesis finds validation in wider literature, where angiogenesis is well-established as a driver of tumor progression. This is corroborated by (i) findings indicating an inverse correlation between increased VEGFA expression and overall survival in TCGA, (ii) elevated CD31 staining in invasive iKAP tumors compared to non-invasive iAP tumors, and (iii) the clinical efficacy of anti-VEGFA monoclonal antibodies in the iKAP model. Consequently, we hold confidence in regarding angiogenesis as a pivotal facet of the tumor's biological impact in KRAS\* CRC, while acknowledging that lipid-rich CAFs may potentially influence other cancer hallmarks, such as EMT, which contribute to tumor progression.

Regarding the mechanism responsible for the upregulation of VEGF in lipid-rich CAFs, we hypothesize that prostaglandin E2 (PGE2) serves as the upstream metabolite driving the specific expression of VEGFA in these cells. It's worth noting that lipid droplets are recognized as major reservoirs for various metabolites, including PGE2 (Accioly et al., 2008). Our gene expression data clearly indicate that the key enzymes involved in PGE2 synthesis and the PGE2 receptors are notably enriched in lipid-rich CAFs, whereas they are absent in myofibroblasts. Furthermore, our PGE2 ELISA analysis reveals an abundance of PGE2 in iKAP tumors compared to iAP tumors, as well as in the conditioned media from KRAS-activated iKAP fibroblasts (i.e., lipid-rich fibroblasts). It is established that PGE2 binds to its receptor PTGER, triggering downstream ERK/JNK signaling, which, in turn, leads to the upregulation of VEGFA expression (Pai et al., 2001). In line with this, our data shows the expression of PTGER1 and PTGER4 in lipid-rich CAFs. Additionally, when we depleted the crucial PGE2 synthesis enzyme, PTGS2, in the conditioned media of KRAS-activated 3T3L1

cells, we observed a reduction in VEGFA expression. Consequently, it can be inferred that PGE2 derived from lipid-rich CAFs is responsible for the upregulation of VEGF, and this process can occur through paracrine, autocrine, and/or intracrine mechanisms, as suggested by Prescott (2000). Importantly, this mechanism operates similarly in our model system.

Our research highlights TFCP2 as a pivotal downstream target of KRAS\* responsible for driving the proangiogenic and adipogenic program. In hepatocellular carcinoma (HCC), TFCP2 is known to regulate MMP9 expression, a factor that promotes angiogenesis (Santhekadur et al., 2012). TFCP2 also functions as a cofactor binding to YAP to regulate gene transcription, including MMP9, FN1, and TJP1, contributing to YAP-dependent liver malignancy (Zhang et al., 2017). However, in the context of CRC, the actions of TFCP2 have been less understood. Prior studies have revealed TFCP2's role in binding to the hypermethylated TF-binding region of CPEB1, thereby suppressing CPEB1 expression and promoting tumor metastasis (Shao et al., 2021). In our CRC investigations, we discovered that TFCP2 operates differently by directly upregulating WNT5B and BMP4 gene transcription, leading to the development of VEGFA-expressing, lipid-rich CAFs. Furthermore, while TFCP2 regulates MMP9 expression in HCC, this was not observed in the CRC model, likely because MMP9 is primarily expressed in myeloid cells and has low or no expression in cancer cells. In CRC, lipid-rich CAFs driven by TFCP2 emerge as the principal source of VEGFA, with myeloid cells as another source, underscoring the significant role of CAFs in tumor angiogenesis. Importantly, our findings link a high-TFCP2 signature to worse prognoses in CRC patients. Encouragingly, in our preclinical models, the inhibition of TFCP2 by FQI1 was well-tolerated and effectively hindered lipofibrogenesis, tumor angiogenesis, and tumor progression. Notably, FQI1 has previously demonstrated its ability to impede tumor growth in subcutaneous xenograft and spontaneous Alb-cMyc HCC models, suggesting the need for further investigations into the role of TFCP2 in various tumor types and genetic profiles (Grant et al.,

2012, Rajasekaran et al., 2015). In the context of CRC, our findings provide a rationale for testing adjuvant FQI1 treatment in early-stage KRAS\*-driven CRC patients who are at a high risk of metastases, such as Stage II patients with significant amounts of circulating tumor DNA after surgery. Additionally, the lipid-rich CAF/TFCP2-high signature could potentially serve as a valuable biomarker for patient selection in CRC trials targeting TFCP2, aimed at reducing disease recurrence. While current therapies targeting KRAS\* in cancers show promise, the emergence of resistance in human trials underscores the necessity to comprehensively define the spectrum of targetable biological actions of KRAS\* in CRC.

In the second part of my study, I delve into the role of genomic instability, specifically CIN, in CRC progression and its interaction with the TME. CRCs with high CIN are characterized by an immunologically "cold" TME, featuring a reduced presence of immune cell populations and resistance to immune checkpoint inhibitors. A tamoxifen (TAM)-inducible telomerase reactivation model (iTAP) was developed to investigate the impact of telomere dynamics on CRC progression, utilizing GEM models with Apc/P53 deletions. iTAP G4 mice, exhibiting homozygous *LSL*-mTERT and shortened telomeres, displayed decreased survival compared to iTAP G0 mice, reinforcing that telomerase reactivation following telomere crisis supports tumor formation but reduces survival. scRNA-seq analyses revealed no differences in cell proportions between G0 and G4 tumors. Further exploration focused on epithelial cells, which displayed heterogeneity in CMS but no significant subtype shift following telomerase reactivation. In-depth inferred CNA analyses indicated a higher prevalence of CIN events in iTAP G4 tumors compared to G0, highlighting the critical role of CIN in gene mutational processes during CRC progression.

This study also extended its investigation to human CRC, characterizing CIN-high and CIN-low patients based on diploid cell percentages. This analysis aimed to enhance the clinical

relevance of understanding telomere dynamics-induced CIN in CRC. Remarkably, both mouse and human studies revealed an increased population of IL17-expressing cells in CIN-high CRC. The shared utilization of cytokines such as IL1b, IL12, and IL23 in the development of these cells suggests that CIN in epithelial cells may promote their differentiation in both species. The ligand-receptor interaction analysis further supported this hypothesis, with IL1 emerging as a pivotal cytokine regulating the differentiation of these cells. Overall, this comprehensive study sheds light on the intricate interplay between telomere dynamics-induced CIN, immune responses, and CRC progression, providing valuable insights into potential therapeutic targets and enhancing our understanding of this complex disease.

## BIBLIOGRAPHY

1. Li, J., Ma, X., Chakravarti, D., Shalapour, S., and DePinho, R.A. (2021). Genetic And Biological Hallmarks Of Colorectal Cancer. *Genes Dev* 35, 787—820. 10.1101/gad.348226.120.
2. Siegel, R.L., Miller, K.D., Fuchs, H.E., and Jemal, A. (2022). Cancer Statistics, 2022. *CA Cancer J Clin* 72, 7—33. 10.3322/caac.21708.
3. Manfredi, S., Lepage, C., Hatem, C., Coatmeur, O., Faivre, J., and Bouvier, A.M. (2006). Epidemiology And Management Of Liver Metastases From Colorectal Cancer. *Ann Surg* 244, 254—259. 10.1097/01.sla.0000217629.94941.cf.
4. Wood LD, Parsons DW, Jones S, Lin J, Sjöblom T, Leary RJ, Shen D, Boca SM, Barber T, Ptak J, Silliman N, Szabo S, Dezso Z, Ustyanksky V, Nikolskaya T, Nikolsky Y, Karchin R, Wilson PA, Kaminker JS, Zhang Z, Croshaw R, Willis J, Dawson D, Shipitsin M, Willson JK, Sukumar S, Polyak K, Park BH, Pethiyagoda CL, Pant PV, Ballinger DG, Sparks AB, Hartigan J, Smith DR, Suh E, Papadopoulos N, Buckhaults P, Markowitz SD, Parmigiani G, Kinzler KW, Velculescu VE, Vogelstein B. The genomic landscapes of human breast and colorectal cancers. *Science*. 2007 Nov 16;318(5853):1108-13.
5. Li, H.T., Lu, Y.Y., An, Y.X., Wang, X., and Zhao, Q.C. (2011). Kras, Braf And Pik3ca Mutations In Human Colorectal Cancer: Relationship With Metastatic Colorectal Cancer. *Oncol Rep* 25, 1691—1697. 10.3892/or.2011.1217.
6. Knijn N, Mekenkamp LJ, Klomp M, Vink-Börger ME, Tol J, Teerenstra S, Meijer JW, Tebar M, Riemersma S, van Krieken JH, Punt CJ, Nagtegaal ID. KRAS mutation analysis: a comparison between primary tumours and matched liver metastases in 305 colorectal cancer patients. *Br J Cancer*. 2011 Mar 15;104(6):1020-6. doi: 10.1038/bjc.2011.26.
7. Boutin AT, Liao WT, Wang M, Hwang SS, Karpinets TV, Cheung H, Chu GC, Jiang S, Hu J, Chang K, Vilar E, Song X, Zhang J, Kopetz S, Futreal A, Wang YA, Kwong LN, DePinho

- RA. Oncogenic Kras drives invasion and maintains metastases in colorectal cancer. *Genes Dev.* 2017 Feb 15;31(4):370-382.
8. Liao W, Overman MJ, Boutin AT, Shang X, Zhao D, Dey P, Li J, Wang G, Lan Z, Li J, Tang M, Jiang S, Ma X, Chen P, Katkhuda R, Korphaisarn K, Chakravarti D, Chang A, Spring DJ, Chang Q, Zhang J, Maru DM, Maeda DY, Zebala JA, Kopetz S, Wang YA, DePinho RA. KRAS-IRF2 Axis Drives Immune Suppression and Immune Therapy Resistance in Colorectal Cancer. *Cancer Cell.* 2019 Apr 15;35(4):559-572.e7.
  9. Pylayeva-Gupta, Y., Grabocka, E. & Bar-Sagi, D. RAS oncogenes: weaving a tumorigenic web. *Nat Rev Cancer* 11, 761-774, doi:10.1038/nrc3106 (2011).
  10. Kapoor A, Yao W, Ying H, Hua S, Liewen A, Wang Q, Zhong Y, Wu CJ, Sadanandam A, Hu B, Chang Q, Chu GC, Al-Khalil R, Jiang S, Xia H, Fletcher-Sananikone E, Lim C, Horwitz GI, Viale A, Pettazzoni P, Sanchez N, Wang H, Protopopov A, Zhang J, Heffernan T, Johnson RL, Chin L, Wang YA, Draetta G, DePinho RA. Yap1 activation enables bypass of oncogenic Kras addiction in pancreatic cancer. *Cell.* 2014 Jul 3;158(1):185-197. doi: 10.1016/j.cell.2014.06.003.
  11. Chen, P., Hsu, W. H., Han, J., Xia, Y. & DePinho, R. A. Cancer Stemness Meets Immunity: From Mechanism to Therapy. *Cell Rep* 34, 108597, doi:10.1016/j.celrep.2020.108597 (2021).
  12. Fearon, E. R. & Carethers, J. M. Molecular subtyping of colorectal cancer: time to explore both intertumoral and intratumoral heterogeneity to evaluate patient outcome. *Gastroenterology* 148, 10-13, doi:10.1053/j.gastro.2014.11.024 (2015).
  13. Singh, A., Sweeney, M.F., Yu, M., Burger, A., Greninger, P., Benes, C., Haber, D.A., and Settleman, J. (2012). TAK1 inhibition promotes apoptosis in KRAS-dependent colon cancers. *Cell* 148, 639-650. 10.1016/j.cell.2011.12.033.
  14. Morris, J.C., Tan, A.R., Olencki, T.E., Shapiro, G.I., Dezube, B.J., Reiss, M., Hsu, F.J., Berzofsky, J.A., and Lawrence, D.P. (2014). Phase I study of GC1008 (fresolimumab): a

- human anti-transforming growth factor-beta (TGFbeta) monoclonal antibody in patients with advanced malignant melanoma or renal cell carcinoma. *PLoS One* 9, e90353. 10.1371/journal.pone.0090353.
15. Rodón J, Carducci M, Sepulveda-Sánchez JM, Azaro A, Calvo E, Seoane J, Braña I, Sicart E, Gueorguieva I, Cleverly A, Pillay NS, Desai D, Estrem ST, Paz-Ares L, Holdhoff M, Blakeley J, Lahn MM, Baselga J. Pharmacokinetic, pharmacodynamic and biomarker evaluation of transforming growth factor- $\beta$  receptor I kinase inhibitor, galunisertib, in phase 1 study in patients with advanced cancer. *Invest New Drugs*. 2015 Apr;33(2):357-70.
  16. Principe DR, DeCant B, Staudacher J, Vitello D, Mangan RJ, Wayne EA, Mascariñas E, Diaz AM, Bauer J, McKinney RD, Khazaie K, Pasche B, Dawson DW, Munshi HG, Grippo PJ, Jung B. Loss of TGF $\beta$  signaling promotes colon cancer progression and tumor-associated inflammation. *Oncotarget*. 2017 Jan 17;8(3):3826-3839.
  17. Spindler KL, Sorensen MM, Pallisgaard N, Andersen RF, Havelund BM, Ploen J, Lassen U, Jakobsen AK. Phase II trial of temsirolimus alone and in combination with irinotecan for KRAS mutant metastatic colorectal cancer: outcome and results of KRAS mutational analysis in plasma. *Acta Oncol*. 2013 Jun;52(5):963-70.
  18. Infante JR, Fecher LA, Falchook GS, Nallapareddy S, Gordon MS, Becerra C, DeMarini DJ, Cox DS, Xu Y, Morris SR, Peddareddigari VG, Le NT, Hart L, Bendell JC, Eckhardt G, Kurzrock R, Flaherty K, Burris HA 3rd, Messersmith WA. Safety, pharmacokinetic, pharmacodynamic, and efficacy data for the oral MEK inhibitor trametinib: a phase 1 dose-escalation trial. *Lancet Oncol*. 2012 Aug;13(8):773-81.
  19. Kopetz S, Grothey A, Yaeger R, Van Cutsem E, Desai J, Yoshino T, Wasan H, Ciardiello F, Loupakis F, Hong YS, Steeghs N, Guren TK, Arkenau HT, Garcia-Alfonso P, Pfeiffer P, Orlov S, Lonardi S, Elez E, Kim TW, Schellens JHM, Guo C, Krishnan A, Dekervel J, Morris V, Calvo Ferrandiz A, Tarpgaard LS, Braun M, Gollerkeri A, Keir C, Maharry K,



- Pickard M, Christy-Bittel J, Anderson L, Sandor V, Tabernero J. Encorafenib, Binimetinib, and Cetuximab in BRAF V600E-Mutated Colorectal Cancer. *N Engl J Med*. 2019 Oct 24;381(17):1632-1643. doi: 10.1056/NEJMoa1908075.
20. Awad MM, Liu S, Rybkin II, Arbour KC, Dilly J, Zhu VW, Johnson ML, Heist RS, Patil T, Riely GJ, Jacobson JO, Yang X, Persky NS, Root DE, Lowder KE, Feng H, Zhang SS, Haigis KM, Hung YP, Sholl LM, Wolpin BM, Wiese J, Christiansen J, Lee J, Schrock AB, Lim LP, Garg K, Li M, Engstrom LD, Waters L, Lawson JD, Olson P, Lito P, Ou SI, Christensen JG, Jänne PA, Aguirre AJ. Acquired Resistance to KRASG12C Inhibition in Cancer. *N Engl J Med*. 2021 Jun 24;384(25):2382-2393. doi: 10.1056/NEJMoa2105281.
21. Bartoschek M, Oskolkov N, Bocci M, Lötvrot J, Larsson C, Sommarin M, Madsen CD, Lindgren D, Pekar G, Karlsson G, Ringnér M, Bergh J, Björklund Å, Pietras K. Spatially and functionally distinct subclasses of breast cancer-associated fibroblasts revealed by single cell RNA sequencing. *Nat Commun*. 2018 Dec 4;9(1):5150.
22. Bernard V, Semaan A, Huang J, San Lucas FA, Mulu FC, Stephens BM, Guerrero PA, Huang Y, Zhao J, Kamyabi N, Sen S, Scheet PA, Taniguchi CM, Kim MP, Tzeng CW, Katz MH, Singhi AD, Maitra A, Alvarez HA. Single-Cell Transcriptomics of Pancreatic Cancer Precursors Demonstrates Epithelial and Microenvironmental Heterogeneity as an Early Event in Neoplastic Progression. *Clin Cancer Res*. 2019 Apr 1;25(7):2194-2205.
23. Costa A, Kieffer Y, Scholer-Dahirel A, Pelon F, Bourachot B, Cardon M, Sirven P, Magagna I, Fuhrmann L, Bernard C, Bonneau C, Kondratova M, Kuperstein I, Zinovyev A, Givel AM, Parrini MC, Soumelis V, Vincent-Salomon A, Mehta-Grigoriou F. Fibroblast Heterogeneity and Immunosuppressive Environment in Human Breast Cancer. *Cancer Cell*. 2018 Mar 12;33(3):463-479.e10.
24. Li H, Courtois ET, Sengupta D, Tan Y, Chen KH, Goh JLL, Kong SL, Chua C, Hon LK, Tan WS, Wong M, Choi PJ, Wee LJK, Hillmer AM, Tan IB, Robson P, Prabhakar S.

- Reference component analysis of single-cell transcriptomes elucidates cellular heterogeneity in human colorectal tumors. *Nat Genet.* 2017 May;49(5):708-718.
25. El Agha E, Moiseenko A, Kheirollahi V, De Langhe S, Crnkovic S, Kwapiszewska G, Szibor M, Kosanovic D, Schwind F, Schermuly RT, Henneke I, MacKenzie B, Quantius J, Herold S, Ntokou A, Ahlbrecht K, Braun T, Morty RE, Günther A, Seeger W, Bellusci S. Two-Way Conversion between Lipogenic and Myogenic Fibroblastic Phenotypes Marks the Progression and Resolution of Lung Fibrosis. *Cell Stem Cell.* 2017 Feb 2;20(2):261-273.e3. doi: 10.1016/j.stem.2016.10.004. Epub 2016 Nov 17. Erratum in: *Cell Stem Cell.* 2017 Apr 6;20(4):571.
  26. Shook BA, Wasko RR, Mano O, Rutenberg-Schoenberg M, Rudolph MC, Zirak B, Rivera-Gonzalez GC, López-Giráldez F, Zarini S, Rezza A, Clark DA, Rendl M, Rosenblum MD, Gerstein MB, Horsley V. Dermal Adipocyte Lipolysis and Myofibroblast Conversion Are Required for Efficient Skin Repair. *Cell Stem Cell.* 2020 Jun 4;26(6):880-895.e6.
  27. Biffi, G., and Tuveson, D.A. (2021). Diversity And Biology Of Cancer–Associated Fibroblasts. *Physiol Rev* 101, 147—176. 10.1152/physrev.00048.2019.
  28. Kalluri, R. (2016). The Biology And Function Of Fibroblasts In Cancer. *Nat Rev Cancer* 16, 582—598. 10.1038/nrc.2016.73.
  29. McAndrews KM, Vázquez-Arreguín K, Kwak C, Sugimoto H, Zheng X, Li B, Kirtley ML, LeBleu VS, Kalluri R.  $\alpha$ SMA+ fibroblasts suppress Lgr5+ cancer stem cells and restrain colorectal cancer progression. *Oncogene.* 2021 Jul;40(26):4440-4452.
  30. Gong J, Lin Y, Zhang H, Liu C, Cheng Z, Yang X, Zhang J, Xiao Y, Sang N, Qian X, Wang L, Cen X, Du X, Zhao Y. Reprogramming of lipid metabolism in cancer-associated fibroblasts potentiates migration of colorectal cancer cells. *Cell Death Dis.* 2020 Apr 23;11(4):267.
  31. Peng S, Li Y, Huang M, Tang G, Xie Y, Chen D, Hu Y, Yu T, Cai J, Yuan Z, Wang H, Wang H, Luo Y, Liu X. Metabolomics reveals that CAF-derived lipids promote colorectal

cancer peritoneal metastasis by enhancing membrane fluidity. *Int J Biol Sci.* 2022 Feb 21;18(5):1912-1932.

32. Pereira BA, Vennin C, Papanicolaou M, Chambers CR, Herrmann D, Morton JP, Cox TR, Timpson P. CAF Subpopulations: A New Reservoir of Stromal Targets in Pancreatic Cancer. *Trends Cancer.* 2019 Nov;5(11):724-741.
33. Wörmann SM, Song L, Ai J, Diakopoulos KN, Kurkowski MU, Görgülü K, Ruess D, Campbell A, Doglioni C, Jodrell D, Neesse A, Demir IE, Karpathaki AP, Barenboim M, Hagemann T, Rose-John S, Sansom O, Schmid RM, Protti MP, Lesina M, Algül H. Loss of P53 Function Activates JAK2-STAT3 Signaling to Promote Pancreatic Tumor Growth, Stroma Modification, and Gemcitabine Resistance in Mice and Is Associated With Patient Survival. *Gastroenterology.* 2016 Jul;151(1):180-193.e12.
34. Tape CJ, Ling S, Dimitriadi M, McMahon KM, Worboys JD, Leong HS, Norrie IC, Miller CJ, Poulogiannis G, Lauffenburger DA, Jørgensen C. Oncogenic KRAS Regulates Tumor Cell Signaling via Stromal Reciprocation. *Cell.* 2016 May 5;165(4):910-20.
35. Velez-Delgado A, Donahue KL, Brown KL, Du W, Irizarry-Negron V, Menjivar RE, Lasse Opsahl EL, Steele NG, The S, Lazarus J, Sirihorachai VR, Yan W, Kemp SB, Kerk SA, Bollampally M, Yang S, Scales MK, Avritt FR, Lima F, Lyssiotis CA, Rao A, Crawford HC, Bednar F, Frankel TL, Allen BL, Zhang Y, Pasca di Magliano M. Extrinsic KRAS Signaling Shapes the Pancreatic Microenvironment Through Fibroblast Reprogramming. *Cell Mol Gastroenterol Hepatol.* 2022;13(6):1673-1699.
36. Shaashua L, Ben-Shmuel A, Pevsner-Fischer M, Friedman G, Levi-Galibov O, Nandakumar S, Barki D, Nevo R, Brown LE, Zhang W, Stein Y, Lior C, Kim HS, Bojmar L, Jarnagin WR, Lecomte N, Mayer S, Stok R, Bishara H, Hamodi R, Levy-Lahad E, Golan T, Porco JA Jr, Iacobuzio-Donahue CA, Schultz N, Tuveson DA, Lyden D, Kelsen D, Scherz-Shouval R. BRCA mutational status shapes the stromal microenvironment of

- pancreatic cancer linking clusterin expression in cancer associated fibroblasts with HSF1 signaling. *Nat Commun.* 2022 Oct 31;13(1):6513.
37. Reya, T., Morrison, S. J., Clarke, M. F. & Weissman, I. L. Stem cells, cancer, and cancer stem cells. *Nature* 414, 105-111, doi:10.1038/35102167 (2001).
38. Artandi, S.E., Chang, S., Lee, S.L., Alson, S., Gottlieb, G.J., Chin, L., and DePinho, R.A. (2000). Telomere dysfunction promotes non-reciprocal translocations and epithelial cancers in mice. *Nature* 406, 641-645. 10.1038/35020592.
39. Harley, C.B. (2008). Telomerase and cancer therapeutics. *Nat Rev Cancer* 8, 167-179. 10.1038/nrc2275.
40. Ding Z, Wu CJ, Jaskelioff M, Ivanova E, Kost-Alimova M, Protopopov A, Chu GC, Wang G, Lu X, Labrot ES, Hu J, Wang W, Xiao Y, Zhang H, Zhang J, Zhang J, Gan B, Perry SR, Jiang S, Li L, Horner JW, Wang YA, Chin L, DePinho RA. Telomerase reactivation following telomere dysfunction yields murine prostate tumors with bone metastases. *Cell.* 2012 Mar 2;148(5):896-907.
41. Lengauer, C., Kinzler, K. W. & Vogelstein, B. Genetic instabilities in human cancers. *Nature* 396, 643-649, doi:10.1038/25292 (1998).
42. Pino, M. S. & Chung, D. C. The chromosomal instability pathway in colon cancer. *Gastroenterology* 138, 2059-2072, doi:10.1053/j.gastro.2009.12.065 (2010).
43. Scott, M.A., Nguyen, V.T., Levi, B., and James, A.W. (2011). Current Methods Of Adipogenic Differentiation Of Mesenchymal Stem Cells. *Stem Cells Dev* 20, 1793—1804. 10.1089/scd.2011.0040.
44. Labun, K., Montague, T.G., Krause, M., Torres Cleuren, Y.N., Tjeldnes, H., and Valen, E. (2019). Chopchop V3: Expanding The Crispr Web Toolbox Beyond Genome Editing. *Nucleic Acids Res* 47, W171—W174. 10.1093/nar/gkz365.
45. Sanjana, N.E., Shalem, O., and Zhang, F. (2014). Improved Vectors And Genome-Wide Libraries For CRISPR Screening. *Nat Methods* 11, 783—784. 10.1038/nmeth.3047.

46. Crowe, A.R., and Yue, W. (2019). Semi-quantitative Determination of Protein Expression using Immunohistochemistry Staining and Analysis: An Integrated Protocol. *Bio Protoc* 9,24: e3465. doi:10.21769/BioProtoc.3465
47. Schindelin J, Arganda-Carreras I, Frise E, Kaynig V, Longair M, Pietzsch T, Preibisch S, Rueden C, Saalfeld S, Schmid B, Tinevez JY, White DJ, Hartenstein V, Eliceiri K, Tomancak P, Cardona A. Fiji: an open-source platform for biological-image analysis. *Nat Methods*. 2012 Jun 28;9(7):676-82.
48. Schneider, C. A., Rasband, W. S., & Eliceiri, K. W. (2012). NIH Image to ImageJ: 25 years of image analysis. *Nature Methods*, 9(7), 671–675. doi:10.1038/nmeth.2089
49. Khan, M., and Gasser, S. (2016). Generating Primary Fibroblast Cultures from Mouse Ear and Tail Tissues. *J Vis Exp*. 10;(107):53565. doi: 10.3791/53565.
50. Boroujerdi, A., Tigges, U., Welser-Alves, J.V., and Milner, R. (2014). Isolation and culture of primary pericytes from mouse brain. *Methods Mol Biol* 1135, 383-392. 10.1007/978-1-4939-0320-7\_31.
51. Terranova, C., Tang, M., Orouji, E., Maitituoheti, M., Raman, A., Amin, S., Liu, Z., and Rai, K. (2018). An Integrated Platform for Genome-wide Mapping of Chromatin States Using High-throughput ChIP-sequencing in Tumor Tissues. *J Vis Exp*. 10.3791/56972.
52. Perez LJ, Rios L, Trivedi P, D'Souza K, Cowie A, Nzirorera C, Webster D, Brunt K, Legare JF, Hassan A, Kienesberger PC, Pulinilkunnil T. Validation of optimal reference genes for quantitative real time PCR in muscle and adipose tissue for obesity and diabetes research. *Sci Rep*. 2017 Jun 15;7(1):3612.
53. Lavie, D., Ben-Shmuel, A., Erez, N., and Scherz-Shouval, R. (2022). Cancer-Associated Fibroblasts In The Single-Cell Era. *Nat Cancer* 3, 793–807. 10.1038/s43018-022-00411-z.
54. Deng, C.C., Hu, Y.F., Zhu, D.H., Cheng, Q., Gu, J.J., Feng, Q.L., Zhang, L.X., Xu, Y.P., Wang, D., Rong, Z., and Yang, B. (2021). Single-cell RNA-seq reveals fibroblast

heterogeneity and increased mesenchymal fibroblasts in human fibrotic skin diseases. *Nat Commun* 12, 3709. 10.1038/s41467-021-24110-y.

55. Muhl L, Genové G, Leptidis S, Liu J, He L, Mocci G, Sun Y, Gustafsson S, Buyandelger B, Chivukula IV, Segerstolpe Å, Raschperger E, Hansson EM, Björkegren JLM, Peng XR, Vanlandewijck M, Lendahl U, Betsholtz C. Single-cell analysis uncovers fibroblast heterogeneity and criteria for fibroblast and mural cell identification and discrimination. *Nat Commun*. 2020 Aug 7;11(1):3953.
56. Habermann AC, Gutierrez AJ, Bui LT, Yahn SL, Winters NI, Calvi CL, Peter L, Chung MI, Taylor CJ, Jetter C, Raju L, Roberson J, Ding G, Wood L, Sucre JMS, Richmond BW, Serezani AP, McDonnell WJ, Mallal SB, Bacchetta MJ, Loyd JE, Shaver CM, Ware LB, Bremner R, Walia R, Blackwell TS, Banovich NE, Kropski JA. Single-cell RNA sequencing reveals profibrotic roles of distinct epithelial and mesenchymal lineages in pulmonary fibrosis. *Sci Adv*. 2020 Jul 8;6(28):eaba1972.
57. Xie T, Wang Y, Deng N, Huang G, Taghavifar F, Geng Y, Liu N, Kulur V, Yao C, Chen P, Liu Z, Stripp B, Tang J, Liang J, Noble PW, Jiang D. Single-Cell Deconvolution of Fibroblast Heterogeneity in Mouse Pulmonary Fibrosis. *Cell Rep*. 2018 Mar 27;22(13):3625-3640.
58. Smith, T.M., Cong, Z., Gilliland, K.L., Clawson, G.A., and Thiboutot, D.M. (2006). Insulin-Like Growth Factor-1 Induces Lipid Production In Human SEB-1 Sebocytes Via Sterol Response Element-Binding Protein-1. *J Invest Dermatol* 126, 1226—1232. 10.1038/sj.jid.5700278.
59. Cordero, A.D., Callihan, E.C., Said, R., Alowais, Y., Paffhausen, E.S., and Bracht, J.R. (2020). Epigenetic Regulation of Neuregulin-1 Tunes White Adipose Stem Cell Differentiation. *Cells* 9(5):1148. 10.3390/cells9051148.
60. Han X, Zhang Z, He L, Zhu H, Li Y, Pu W, Han M, Zhao H, Liu K, Li Y, Huang X, Zhang M, Jin H, Lv Z, Tang J, Wang J, Sun R, Fei J, Tian X, Duan S, Wang QD, Wang L, He B,

- Zhou B. A suite of new Dre recombinase drivers markedly expands the ability to perform intersectional genetic targeting. *Cell Stem Cell*. 2021 Jun 3;28(6):1160-1176.e7.
61. Lin X, Dong R, Diao S, Yu G, Wang L, Li J, Fan Z. SFRP2 enhanced the adipogenic and neuronal differentiation potentials of stem cells from apical papilla. *Cell Biol Int*. 2017 May;41(5):534-543.
62. Ullah, M., Stich, S., Haupl, T., Eucker, J., Sittinger, M., and Ringe, J. (2013). Reverse differentiation as a gene filtering tool in genome expression profiling of adipogenesis for fat marker gene selection and their analysis. *PLoS One* 8, e69754. 10.1371/journal.pone.0069754.
63. Guan, H., Zhang, Y., Gao, S., Bai, L., Zhao, S., Cheng, X.W., Fan, J., and Liu, E. (2018). Differential Patterns of Secreted Frizzled-Related Protein 4 (SFRP4) in Adipocyte Differentiation: Adipose Depot Specificity. *Cell Physiol Biochem* 46, 2149-2164. 10.1159/000489545.
64. Franzen, O., Gan, L.M., and Bjorkegren, J.L.M. (2019). Panglaodb: A Web Server For Exploration Of Mouse And Human Single–Cell Rna Sequencing Data. *Database (Oxford)* 2019;2019:baz046. 10.1093/database/baz046.
65. McGowan, S.E., and McCoy, D.M. (2014). Regulation Of Fibroblast Lipid Storage And Myofibroblast Phenotypes During Alveolar Septation In Mice. *Am J Physiol Lung Cell Mol Physiol* 307, L618—631. 10.1152/ajplung.00144.2014.
66. Park J, Ivey MJ, Deana Y, Riggsbee KL, Sørensen E, Schwabl V, Sjöberg C, Hjertberg T, Park GY, Swonger JM, Rosengreen T, Morty RE, Ahlbrecht K, Tallquist MD. The Tcf21 lineage constitutes the lung lipofibroblast population. *Am J Physiol Lung Cell Mol Physiol*. 2019 May 1;316(5):L872-L885.
67. Sanchez—Gurmaches, J., Hung, C.M., and Guertin, D.A. (2016). Emerging Complexities In Adipocyte Origins And Identity. *Trends Cell Biol* 26, 313—326. 10.1016/j.tcb.2016.01.004.

68. Goralski KB, McCarthy TC, Hanniman EA, Zabel BA, Butcher EC, Parlee SD, Muruganandan S, Sinal CJ. Chemerin, a novel adipokine that regulates adipogenesis and adipocyte metabolism. *J Biol Chem*. 2007 Sep 21;282(38):28175-88.
69. Unamuno X, Gómez-Ambrosi J, Ramírez B, Rodríguez A, Becerril S, Valentí V, Moncada R, Silva C, Salvador J, Frühbeck G, Catalán V. Dermatoportun, A Novel Adipokine Promoting Adipose Tissue Extracellular Matrix Remodelling and Inflammation in Obesity. *J Clin Med*. 2020 Apr 9;9(4):1069.
70. Christodoulides, C., Lagathu, C., Sethi, J.K., and Vidal-Puig, A. (2009). Adipogenesis And Wnt Signalling. *Trends Endocrinol Metab* 20, 16—24. 10.1016/j.tem.2008.09.002.
71. Huang H, Song TJ, Li X, Hu L, He Q, Liu M, Lane MD, Tang QQ. BMP signaling pathway is required for commitment of C3H10T1/2 pluripotent stem cells to the adipocyte lineage. *Proc Natl Acad Sci U S A*. 2009 Aug 4;106(31):12670-5.
72. Lv, Y.Q., Dhlamini, Q., Chen, C., Li, X., Bellusci, S., and Zhang, J.S. (2021). Fgf10 And Lipofibroblasts In Lung Homeostasis And Disease: Insights Gained From The Adipocytes. *Front Cell Dev Biol* 9, 645400. 10.3389/fcell.2021.645400.
73. Cristancho, A.G., and Lazar, M.A. (2011). Forming Functional Fat: A Growing Understanding Of Adipocyte Differentiation. *Nat Rev Mol Cell Biol* 12, 722—734. 10.1038/nrm3198.
74. Banerjee S, Zhang X, Kuang S, Wang J, Li L, Fan G, Luo Y, Sun S, Han P, Wu Q, Yang S, Ji X, Li Y, Deng L, Tian X, Wang Z, Zhang Y, Wu K, Zhu S, Bolund L, Yang H, Xu X, Liu J, Lu Y, Liu X. Comparative analysis of clonal evolution among patients with right- and left-sided colon and rectal cancer. *iScience*. 2021 Jun 11;24(7):102718.
75. Cellurale C, Sabio G, Kennedy NJ, Das M, Barlow M, Sandy P, Jacks T, Davis RJ. Requirement of c-Jun NH(2)-terminal kinase for Ras-initiated tumor formation. *Mol Cell Biol*. 2011 Apr;31(7):1565-76.



76. Reed, B.C., and Lane, M.D. (1980). Insulin Receptor Synthesis And Turnover In Differentiating 3T3–L1 Preadipocytes. *Proc Natl Acad Sci U S A* 77, 285–289. 10.1073/pnas.77.1.285.
77. Cancer Genome Atlas Network. Comprehensive molecular characterization of human colon and rectal cancer. *Nature*. 2012 Jul 18;487(7407):330-7.
78. Fechner, P.Y. (1996). The Role Of Sry In Mammalian Sex Determination. *Acta Paediatr Jpn* 38, 380–389. 10.1111/j.1442—200x.1996.tb03512.x.
79. Volker, J.L., Rameh, L.E., Zhu, Q., DeCaprio, J., and Hansen, U. (1997). Mitogenic Stimulation Of Resting T Cells Causes Rapid Phosphorylation Of The Transcription Factor LSF And Increased DNA–Binding Activity. *Genes Dev* 11, 1435–1446. 10.1101/gad.11.11.1435.
80. Grant TJ, Bishop JA, Christadore LM, Barot G, Chin HG, Woodson S, Kavouris J, Siddiq A, Gredler R, Shen XN, Sherman J, Meehan T, Fitzgerald K, Pradhan S, Briggs LA, Andrews WH, Sarkar D, Schaus SE, Hansen U. Antiproliferative small-molecule inhibitors of transcription factor LSF reveal oncogene addiction to LSF in hepatocellular carcinoma. *Proc Natl Acad Sci U S A*. 2012 Mar 20;109(12):4503-8.
81. Santhekadur PK, Rajasekaran D, Siddiq A, Gredler R, Chen D, Schaus SE, Hansen U, Fisher PB, Sarkar D. The transcription factor LSF: a novel oncogene for hepatocellular carcinoma. *Am J Cancer Res*. 2012;2(3):269-85.
82. Rudolph KL, Chang S, Lee HW, Blasco M, Gottlieb GJ, Greider C, DePinho RA. Longevity, stress response, and cancer in aging telomerase-deficient mice. *Cell*. 1999 Mar 5;96(5):701-12.
83. Jaskelioff M, Muller FL, Paik JH, Thomas E, Jiang S, Adams AC, Sahin E, Kost-Alimova M, Protopopov A, Cadiñanos J, Horner JW, Maratos-Flier E, Depinho RA. Telomerase reactivation reverses tissue degeneration in aged telomerase-deficient mice. *Nature*. 2011 Jan 6;469(7328):102-6.

84. Maciejowski J, Li Y, Bosco N, Campbell PJ, de Lange T. Chromothripsis and Kataegis Induced by Telomere Crisis. *Cell*. 2015 Dec 17;163(7):1641-54. doi: 10.1016/j.cell.2015.11.054. PMID: 26687355; PMCID: PMC4687025
85. Lee HO, Hong Y, Etliloglu HE, Cho YB, Pomella V, Van den Bosch B, Vanhecke J, Verbandt S, Hong H, Min JW, Kim N, Eum HH, Qian J, Boeckx B, Lambrechts D, Tsantoulis P, De Hertogh G, Chung W, Lee T, An M, Shin HT, Joung JG, Jung MH, Ko G, Wirapati P, Kim SH, Kim HC, Yun SH, Tan IBH, Ranjan B, Lee WY, Kim TY, Choi JK, Kim YJ, Prabhakar S, Tejpar S, Park WY. Lineage-dependent gene expression programs influence the immune landscape of colorectal cancer. *Nat Genet*. 2020 Jun;52(6):594-603.
86. Harmon C, Zaborowski A, Moore H, St Louis P, Slattery K, Duquette D, Scanlan J, Kane H, Kunkemoeller B, McIntyre CL, Scannail AN, Moran B, Anderson AC, Winter D, Brennan D, Brehm MA, Lynch L.  $\gamma\delta$  T cell dichotomy with opposing cytotoxic and wound healing functions in human solid tumors. *Nat Cancer*. 2023 Aug;4(8):1122-1137.
87. Mills, K.H.G. IL-17 and IL-17-producing cells in protection versus pathology. *Nat Rev Immunol* 23, 38–54 (2023).
88. Kaplan, N.B., Grant, M.M., and Brody, J.S. (1985). The Lipid Interstitial Cell Of The Pulmonary Alveolus. Age And Species Differences. *Am Rev Respir Dis* 132, 1307—1312. 10.1164/arrd.1985.132.6.1307.
89. O'Hare, K.H., and Sheridan, M.N. (1970). Electron Microscopic Observations On The Morphogenesis Of The Albino Rat Lung, With Special Reference To Pulmonary Epithelial Cells. *Am J Anat* 127, 181—205. 10.1002/aja.1001270205.
90. Barkauskas, C.E., Crouce, M.J., Rackley, C.R., Bowie, E.J., Keene, D.R., Stripp, B.R., Randell, S.H., Noble, P.W., and Hogan, B.L. (2013). Type 2 alveolar cells are stem cells in adult lung. *J Clin Invest* 123, 3025-3036. 10.1172/JCI68782.
91. McQualter, J.L., McCarty, R.C., Van der Velden, J., O'Donoghue, R.J., Asselin-Labat, M.L., Bozinovski, S., and Bertoncello, I. (2013). TGF-beta signaling in stromal cells acts

- upstream of FGF-10 to regulate epithelial stem cell growth in the adult lung. *Stem Cell Res* 11, 1222-1233. 10.1016/j.scr.2013.08.007.
92. Rehan, V.K., and Torday, J.S. (2014). The Lung Alveolar Lipofibroblast: An Evolutionary Strategy Against Neonatal Hyperoxic Lung Injury. *Antioxid Redox Signal* 21, 1893—1904. 10.1089/ars.2013.5793.
93. Ntokou A, Klein F, Dontireddy D, Becker S, Bellusci S, Richardson WD, Szibor M, Braun T, Morty RE, Seeger W, Voswinckel R, Ahlbrecht K. Characterization of the platelet-derived growth factor receptor- $\alpha$ -positive cell lineage during murine late lung development. *Am J Physiol Lung Cell Mol Physiol*. 2015 Nov 1;309(9):L942-58.
94. Accioly, M.T., Pacheco, P., Maya-Monteiro, C.M., Carrossini, N., Robbs, B.K., Oliveira, S.S., Kaufmann, C., Morgado-Diaz, J.A., Bozza, P.T., and Viola, J.P. (2008). Lipid bodies are reservoirs of cyclooxygenase-2 and sites of prostaglandin-E2 synthesis in colon cancer cells. *Cancer Res* 68, 1732-1740. 10.1158/0008-5472.CAN-07-1999.
95. Pai, R., Szabo, I.L., Soreghan, B.A., Atay, S., Kawanaka, H., and Tarnawski, A.S. (2001). PGE(2) stimulates VEGF expression in endothelial cells via ERK2/JNK1 signaling pathways. *Biochem Biophys Res Commun* 286, 923-928. 10.1006/bbrc.2001.5494.
96. Prescott, S.M. (2000). Is cyclooxygenase-2 the alpha and the omega in cancer? *J Clin Invest* 105, 1511-1513. 10.1172/JCI10241.
97. Zhang X, Sun F, Qiao Y, Zheng W, Liu Y, Chen Y, Wu Q, Liu X, Zhu G, Chen Y, Yu Y, Pan Q, Wang J. TFCP2 Is Required for YAP-Dependent Transcription to Stimulate Liver Malignancy. *Cell Rep*. 2017 Oct 31;21(5):1227-1239.
98. Shao, K., Pu, W., Zhang, J., Guo, S., Qian, F., Glurich, I., Jin, Q., Ma, Y., Ju, S., Zhang, Z., and Ding, W. (2021). DNA hypermethylation contributes to colorectal cancer metastasis by regulating the binding of CEBPB and TFCP2 to the CPEB1 promoter. *Clin Epigenetics* 13, 89. 10.1186/s13148-021-01071-z.

Rajasekaran D, Siddiq A, Willoughby JL, Biagi JM, Christadore LM, Yunes SA, Gredler R, Jariwala N, Robertson CL, Akiel MA, Shen XN, Subler MA, Windle JJ, Schaus SE, Fisher PB, Hansen U, Sarkar D. Small molecule inhibitors of Late SV40 Factor (LSF) abrogate hepatocellular carcinoma (HCC): Evaluation using an endogenous HCC model. *Oncotarget*. 2015 Sep 22;6(28):26266-77.

## TABLES

### TABLE1

#Supplementary Table 1 includes DEGs from 4 fibroblast subtypes						
MMP13	CD55	ELN	IGFBP5	RBP12	MMP22	PTX3
CXCL131	C4B2	CXCL14	HAS1	GPX3	SERPINE21	APOD
IL1RL1	PTGS21	SMOC1	VCAN2	PDPN3	COL1A12	APOE
LUM	CCL71	MFAP41	MMP9	ASP1	LOXL11	ELN1
SFRP1	DCN2	COL3A12	HSD11B12	IFI205	FN1	CLEC3B
CEMIP	SAA31	GAS6	PDGFRA1	RNASE41	PLOD22	THBS2
PI16	FBLN11	TNXB	TMEM119	UGDH	TMEM176B	AEBP12
MMP101	IFI27L2A1	MGP1	CCDC801	FBN12	NBL1	GREM12
ADAMDEC1	IGFBP6	PTN	CP1	PTGES1	HGF1	SDC23
C3	SLIT3	CCN5	MFAP42	NPPC	C1QTNF3	GAS1
COL14A1	SFRP11	FBLN21	HTRA11	NCAM12	IGFBP53	
NRG11	SERPINA3N1	COL1A21	SVEP11	PRELP1	TMEM176A	
CILP	CCDC802	TNC1	SPON21	RARRES2	RBP4	
INHBA1	CCL21	DIO2	CHL11	IGFBP43	SPON22	
SFRP2	FBLN1	LCN21	ADAM231	LRP12	SCARA5	
GSN1	BMP21	DPT2	BGN1	C4B1	LAMA51	
SERPINA3N2	IFI27L2A	WNT5A1	MEG31	PMEPA1	FHL12	
COL8A1	SLPI	TNFAIP6	PAPPA	CHL1	TGFB11	
DPT1	PLAU	GFPT2	EFEMP11	BMP5	CRYAB1	
GSN	IL33	ABI3BP2	TNFSF13B2	VCAN1	TGFBR31	
IL11	EREG1	FGF71	SERPINF1	CD551	LGI21	
MFAP5	C31	TIMP11	RARRES21	SVEP12	BGN2	
CLEC3B1	MGP2	OGN	TNFAIP61	LBP1	PTCH1	
GREM11	LPL1	IGF1	PDGFRA	ECM12	CCL112	

**TABLE2**

#Supplementary Table 2 includes Lipid-rich CAFs gene signature							
PPARG	FGR	COL6A2	WIF1	CYP1B1	CCL19	NOX4	STAT3
FABP4	HCK	FABP4	SNHG18	COL13A1	NNMT	THY1	TCF4
DLK1	TNFRSF1B	ASPN	CDH11	ADAMTS10	FOXF1	CD40	ZEB2
DLK2	PRKCD	ANGPTL2	PTCH1	CCL11	HAS1	SERPINH1	LAMC1
ZFP423	ENO3	EFEMP1	ARAP1	ADAM33	CTGF	CD44	MEDAG
TCF21	ABI3	SCARA5	FBLN2	COL4A3	ERCC1	PDGFRA	LAMB1
LPL	TREML4	IGFBP3	IGF1	COL4A4	WISP1	EN1	DKK3
PLIN4	PIP4K2A	COPZ2	PRRX1	LAMA2	TWIST2	DCN	TBX20
CEBPA	CD300E	DPEP1	FKBP7	ACKR3	RIPK3	CEBPB	MDK
CEBPB	SERPINB10	ADAMTS5	OAF	CD55	DDR2	EGR1	GSTM5
DCN	CTHRC1	COL5A1	COL6A3	FBLN7	ELN	FOSB	NGF
DPT	TBX18	CD248	CTSK	FIBIN	FN1	FOSL2	VEGFA
CFD	COL15A1	PI16	DKK1	THBS2	HHIP	HIF1A	FGF2
CCL2	GJB2	PAMR1	C1S	NOV	FMO2	KLF2	P4HTM
IL1R1	IL34	TNXB	RARRES2	PTX3	COL1A2	KLF4	CKAP4
FAP	EDN3	MMP2	GREM1	MMP3	COL3A1	KLF6	INMT
FLI1	SLC6A13	COL14A1	SPON2	LRRK1	VIM	KLF9	CXCL14
CELA1	VTN	CLEC3B	TCF21	HGF	FSTL1	NFAT5	
LOX	ITIH5	IGFBP6	PCSK6	FRZB	GSN	NFATC1	
PDGFRB	LUM	COL5A2	COL8A1	COL12A1	SPARC	NFKB1	
P4HA1	DPT	FBN1	ENTPD2	COL7A1	S100A4	NR4A1	
UCP2	POSTN	MFAP5	CXCL8	MEOX1	NT5E	NR4A2	
CCR2	PENK	FKBP10	CXCL3	PRG4	COL1A1	PBX1	
ITGAL	MMP14	PALLD	IL6	PKD2	MGP	RUNX1	

**TABLE3**

#Supplementary Table 3 contains the predicted TFs on pro-adipogenic cytokines' promoter								
Pax-6	c-Ets-2	ABI4	ABF1	SRY	T3R-beta1	R	DSXM	NF-kappaB1
RC2	c-Ets-1	MYBAS1	POU2F2	CREMtau	SF-1	LVb-binding	E2F-1	BTEB4
Elk-1	TGGCA-binding	AP-2alpha	LCR-F1	CREMtau1	USF2	HELIOS	CDX2	ANT
MF3	LIM1	Pax-9a	POU3F1	CREMtau2	Pax-2	NF-E4	HOXD8	EBF
Zic3	C/EBPalpha	Pax-9b	AGL3	MEF1	SPF1	Sp3	POU1F1b	INSAF
NF-1	R2	NF-Y	Nkx6-2	myogenin	POU4F1(I)	AP-4	POU1F1c	c-Myc
NF-X3	Nkx2-1	CUTL1	POU2F1	MyoD	HNF-1C	E12	NF-AT4	NF-InsE2
En-1	Nkx2-5	POU1F1a	HNF-3alpha	FOXP2	AP-2	Myf-3	ENKTF-1	NF-InsE3
Sox2	NFI/CTF	C/EBPdelta	Pax-4a	TFIIB	RAR-gamma	AP-2alphaA	C/EBPbeta	Zta
Ncx	WT1	GBF	POU3F2	FOXD3	Pax-2a	SXR:RXR-alp	TBP	RF2a
Cdx-1	DEF:GLO	unc-86	FOXP3	YY1	c-Myb	PUR	AP-1	TSAP
HNF-3	MNB1a	BR-C	EllaE-A	SBF-1	MED8	BTEB3	GATA-2	MCB1
HNF-3beta	DEF:GLO:SQ	C/EBPbeta(p	FOXO3a	TII	STAT5A	TCF-1A	ALF1B	MCB2
MYB2	COE2	HSF1	Pax-8	Antp	XPF-1	LEF-1	E2F-5	MAZ
IPF1	f(alpha)-f(ep	Pu	USF2b	Prd	DBP	TCF-4E	PPAR-alpha:	Xvent-1
Alfin1	GAL4	NF-AT2	c-Jun	p53	Spz1	MIG1	ADR1	LyF-1
Msx-1	Tal-1	NF-AT1	JunB	AT-BP1	VDR	T-Ag	CCBF	C/EBPgamma
Pax-5	AREB6	TRM1	c-Fos	AT-BP2	LVc	PR	SWI4	GATA-1
ZF5	E47	AP-3	JunD	Nrf2:MafK	44167	GR-alpha	SWI6	TCF-1(P)
Vpr	CP2	STAT1beta	NHP-1	PBF	T3R-alpha1	GR-beta	USF	RP58
HMG	Adf-1	HNF-1B	ATF3	MZF-1	MATalpha2	IRF-1	RAR-beta:RXR-alpha	
STAT4	C/EBP	Ubx	GR	Zic1	MAC1	PEA3	Yi	
p300	CAC-binding	Crx	GA-BF	Zic2	USF-1	IRF-3	Pbx1b	
FACB	LF-A1	COE1	HOXA3	AIRE	TAF	DSXF	ETF	

#TF signature upregulated in iKAP Inv	#TF signature upregulated in KRAS* TCGA
FREAC2	MYAATNNNNNNNGGC
LBP1	FREAC4
AREB6	AP1
YWATTWNN	PR
FOXO4	ZID
PAX4	GGCNRNWCTTYS
AP4	FOXO1
CP2	TEF
TEF1	ZIC3
SRY	TAL1ALPHAE47
AR	GATA6
MYOD	CDC5
AP4	YTAATTAA
AP4	P53
MAZ	TGIF
CRGAARNN	HEB
FOXO1	FREAC7
YGTCCTTGR	OSF2
SRF	SRF
AP1	FOXO3
E2A	TAL1BETAITF2
HNF3ALPHA	RFX1
ETS1	MEF2
CP2	PAX
AP1FJ	OCT1
CTGRYYYNA	CGGAARNGGCNG
OCT1	OCT1
GGATTA	EVI1
BACH2	MYB
STAT3	TGTTTGY
HMEF2	PSMB5
SMAD	TFIIA
SPZ1	HEN1
KMT2D	TTF1
EGR1	PRMT5
OCT	NKX3A
CP2	AP1
AR	SRY
GREB1	
ATF6	
HNF3ALPHA	
OCT1	
SRF	
AP1	
GATAAGR	
ZNF746	
HNF3	
YNTTTNNNANGCARM	

**TABLE4**

#Supplementary Table 4 shows Primers that used for RT-qPCR and ChIP-qPCR				
Exprimment	Gene/primer name	Forward	Reverse	
RT-qPCR	mActa2	TGCTGACAGAGGCACCACTGAA	CAGTTGTACGTCCAGAGGCATAG	
	mPi16	AACTGGCACGAGGAGCATGAGT	GCCAATTCCTCAGTCTTGCTCC	
	mCxcl13	CATAGATCGGATTCAAGTTACGCC	GTAACCAATTTGGCAGGAGGATTC	
	mCol12a1	CAGCACCATGAATGTCGTCTGG	GGTCTTTGAGGATAGTGTCTGGC	
	mMMP13	GATGACCTGTCTGAGGAAGACC	GCATTTCTCGGAGCCTGTCAAC	
	mSpp1	GCTTGGCTTATGGACTGAGGTC	CCTTAGACTCACCGCTCTTCATG	
	mMmp9	GCTGACTACGATAAGGACGGCA	TAGTGGTGCAGGCAGAGTAGGA	
	mCfh	GAGACAAGCAGGAGTACGAACG	CCATCCAAGTATTTACGGTGGT	
	mLpl	CGGTAGCAGGAAGTCTGACCAA	AGCGTCATCAGGAGAAGGCGCA	
	mPlin4	GTGTCCACCAACTCACAGATG	GGACCATTCTTTTGACGAT	
	mPparg	GTAAGTGTGGTTTTCAGAAAGTCC	ATCTCCGCCAACAGCTTCTCT	
	mTcf21	CGTCCAGCTACATCGCTCACTT	CAGGTCATTCTCTGGTTTGGCCG	
	mFgf10	ATCACCTCCAAGGAGATGTCCG	CGGCAACAACCTCCGATTCCAC	
	mTgfb1	CCACTGCAAGACCATCGAC	CTGGCGAGCCTTAGTTGGAC	
	mBmp4	ATTCTGTGTAACCGAATGCTG	CCGGTCTCAGGTATCAAACTAGC	
	mBmp2	GGGACCCGCTGTCTTCTAGT	TCAAACAAATTCGCTGAGGAC	
	mEcm1	TTCAGACCAGCGAGAGATGAC	GGAGTCTCCGGTTTGTGG	
	mWnt5b	GCTACCGCTTTGCCAAGGAGTT	CATTTGCAGGCAGCATCAGCCA	
	mWnt5a	CAACTGGCAGGACTTTCTCAA	CCTTCTCCAATGTACTGCATGTG	
	mWnt10b	GCGGGTCTCTGTTCTTGG	CCGGGAAGTTTAAAGCCGAG	
	mFabp4	TGAAATCACCCGACGACACAGG	GCTTGTCAACATCTCGTTTCTC	
	mCebpa	GCAAAGCCAAGAAGTCGGTGGA	CCTTCTGTTGCGTCTCCACGTT	
	mYwhaz	CAGAAGACGGAAAGGTGCTGAGA	CTTTCTGGTTGCGAAGCATTGGG	
	mActb	CATTGCTGACAGGATGCAGAAGG	TGCTGGAAGGTGGACAGTGAGG	
	hZFP423	CAAGTGCAGATGACCTTCGAG	GGAGTCGAACATCTGTTGCAC	
	hFGF10	TGAGAAGAACGGGAAGGTCAGC	TGGCTTTGACGGCAACAACCTCC	
	hPPARG	AGCCTGCGAAAGCCTTTTGGTG	GGCTTACATTCAGCAAACCTGG	
	hPlin1	GCGGAATTTGCTGCCAACCTC	AGACTTCTGGGCTTGTGGTGT	
	hPLIN2	GATGGCAGAGAACGGTGTGAAG	CAGGCATAGGTATTGGCAACTGC	
	hPLIN4	CCCACGCTTGGCAATGCTGCA	TGTTCCGCCGACAGCACCTTTG	
	hAPOE	GGGTCGCTTTTGGGATTACCTG	CAACTCCTTCATGGTCTCGTCC	
	hVEGFA	TTGCCTTGCTGCTCTACCTCCA	GATGGCAGTAGCTGCGCTGATA	
	hCSF1	TGAGACACCTCTCCAGTTGCTG	GCAATCAGGCTTGGTCACCACA	
	hDLK1	CCCCAAAATGGATTCTGCGAGG	GGTTCTCCACAGAGTCCGTGAA	
	hPTX3	CGAAATAGACAATGGACTCCATCC	CTCATCTGCGAGTCTCCAGCA	
	hHGF	GAGAGTTGGGTTCTTACTGCACG	CTCATCTCTCTCCGTGGACA	
	hLCN2	GTGAGCACCAACTACAACCAGC	GTTCCGAAGTCAGCTCCTTGGT	
	hACTB	CACCATTGGCAATGAGCGGTTTC	AGGTCTTTGCGGATGTCCACGT	
	ChIP-qPCR	Bmp4 ChIP P1	CCCAGAAACCAAGAACCAGG	GCGCTGAAGGAAATCACAGC
		Bmp4 ChIP P2	TAGACCTGGGGATCGATGG	GTGTGCCCCAAGGAGATACC
Bmp4 ChIP P3		CTGGGGAGCTGTGCAATCTT	TTAATCGCTCCCTCTCTGG	
Wnt5b ChIP P1		AGTTGCTTCTCTCACGCTGT	GGTGGACCCCTAGAATGCTC	
Wnt5b ChIP P2		TGCCACCCCAATCCAAGAG	GGAGCTGTTGTTCTCAGGGG	
Wnt5b ChIP P3		AACTGGGCCCTAAGTCTCTGA	ACCCGGGAGCTATTTCCACT	



**TABLE5**

#Supplementary Table 5 shows the human CRC clinical information

Patient	Sample_type	Location	Gender	Current_age_at_collec	MS_status
C1	Colorectal cancer	Colon	M	47	IV MSS
C2	Colorectal cancer	Colon	M	39	IV MSS
C3	Colorectal cancer	Colon	F	65	IV MSS
C4	Colorectal cancer	Colon	M	85	II MSI
C5	Colorectal cancer	Colon	M	72	IV MSS
C6	Colorectal cancer	Colon	F	62	IV MSS
L1	Colorectal cancer	Liver	F	64	IV MSS
L4	Colorectal cancer	Liver	M	70	IV MSS
L6	Colorectal cancer	Liver	F	68	IV MSS
L8	Colorectal cancer	Liver	M	54	IV MSS
L9	Colorectal cancer	Liver	M	56	IV MSS
L11	Colorectal cancer	Liver	M	60	IV MSS

APC	ARID1A	ATR	AXL	BRAF	FBXW7	KDR	KRAS	NOTCH2	PIK3CA	PPP2R1A	PTEN	RNF43	SETD2	TERT	TP53
Wildtype	Wildtype	Wildtype	Wildtype	Wildtype	Wildtype	Wildtype	Wildtype	Mutant	Wildtype	Wildtype	Wildtype	Wildtype	Wildtype	Wildtype	Mutant
Wildtype	Wildtype	Mutant	Wildtype	Wildtype	Wildtype	Wildtype	Wildtype	Wildtype	Wildtype	Wildtype	Wildtype	Wildtype	Wildtype	Wildtype	Mutant
Wildtype	Mutant	Wildtype	Wildtype	Wildtype	Wildtype	Wildtype	Mutant	Wildtype	Wildtype	Mutant	Wildtype	Wildtype	Wildtype	Wildtype	Mutant
NA	NA	NA	NA	NA	NA	NA	NA	NA	NA	NA	NA	NA	NA	NA	NA
Wildtype	Wildtype	Wildtype	Wildtype	Wildtype	Wildtype	Wildtype	Mutant	Wildtype	Wildtype	Wildtype	Wildtype	Wildtype	Wildtype	Wildtype	Wildtype
Wildtype	Wildtype	Wildtype	Wildtype	Wildtype	Wildtype	Wildtype	Mutant	Wildtype	Wildtype	Wildtype	Wildtype	Wildtype	Wildtype	Wildtype	Mutant
Wildtype	Wildtype	Wildtype	Wildtype	Mutant	Wildtype	Wildtype	Wildtype	Wildtype	Wildtype	Wildtype	Wildtype	Mutant	Wildtype	Wildtype	Mutant
Mutant	Wildtype	Wildtype	Wildtype	Wildtype	Wildtype	Mutant	Mutant	Wildtype	Mutant	Wildtype	Wildtype	Wildtype	Wildtype	Wildtype	Mutant
Wildtype	Wildtype	Wildtype	Wildtype	Wildtype	Wildtype	Wildtype	Mutant	Wildtype	Wildtype	Wildtype	Mutant	Wildtype	Wildtype	Wildtype	Mutant
Wildtype	Wildtype	Wildtype	Wildtype	Mutant	Mutant	Wildtype	Mutant	Wildtype	Wildtype	Wildtype	Wildtype	Wildtype	Mutant	Wildtype	Wildtype
Wildtype	Wildtype	Wildtype	Wildtype	Mutant	Wildtype	Wildtype	Wildtype	Wildtype	Wildtype	Wildtype	Wildtype	Wildtype	Wildtype	Wildtype	Wildtype
Wildtype	Wildtype	Wildtype	Wildtype	Wildtype	Wildtype	Wildtype	Wildtype	Wildtype	Wildtype	Wildtype	Wildtype	Wildtype	Wildtype	Wildtype	Wildtype

## VITA

Wen-Hao (Howard) Hsu was born in Taiwan. He earned his Bachelor of Science degree with a major in Life Sciences from Fu Jen Catholic University in 2010. Subsequently, he pursued a Master of Science degree with a major in Head and Neck Cancer Biology at Taiwan University and worked as a graduate researcher for five years at Yang-Ming University. In August of 2018, he enrolled in The University of Texas MD Anderson Cancer Center UTHealth Graduate School of Biomedical Sciences.

Permanent address: 190 Fable Ct, Mountain View, CA, 94043